

LIGHT PIPE OPTICAL CHARACTERIZATION

A Dissertation

by

MATTHEW TIMOTHY MORRISON

Submitted to the Office of Graduate and Professional Studies of
Texas A&M University
in partial fulfillment of the requirements for the degree of

DOCTOR OF PHILOSOPHY

Chair of Committee,	George R. Welch
Co-Chair of Committee,	Christi K. Madsen
Committee Members,	Alexey Belyanin Philip Hemmer
Head of Department,	Grigory Rogachev

May 2018

Major Subject: Applied Physics

Copyright May 2018 Matthew Timothy Morrison

ABSTRACT

With glass processing methodologies improving, namely femtosecond laser irradiated assisted chemical etching (FLICE), freeform fused silica structures having micron level features are becoming increasingly more feasible to physically realize. One application of this technology is the creation of light pipes for solar concentrators, as fused silica offers significantly higher transmission and damage threshold properties over that of comparable polymer-based structures for the same purpose without suffering from related photodegradation pathways. As such fused silica structures having millimeter scale dimensions have not been widely used for such purposes due to their previous scarcity, the community is, in some ways, in its infancy in terms of adopting standardized light pipe characterization practices. The aim of this work is to identify major loss mechanisms of fused silica light pipes pertinent to their application as a solar concentrator, establish transmission testing practices while identifying critical measurement and assembly considerations, and to demonstrate the possibility of high throughput light pipe structures made out of fused silica. To achieve this, a custom test bench has been developed that includes the ability to launch light rays of a given source at an arbitrary angle and location on a given light pipe structure.

A fused silica rectangular prism light pipe 50 mm x 1 mm x 1 mm was shown to transmit, on average, > 90% (Fresnel reflection losses are not subtracted) of 514 nm center wavelength light launched at incidence angles from 0 to 25°.

DEDICATION

To my family, to Narda, my friends, to good graduate students everywhere riding the roller coaster of graduate school, to long hours spent on behalf of students and science, to the stolen moments, to the missed moments, to the path behind us, and to the journey ahead.

ACKNOWLEDGMENTS

Were it not for the chance my advisor, Professor Christi K. Madsen, took by bringing me on board her team, I would have never had the deeply educational experiences I did while performing this work. I am truly grateful for all of her support and instruction during my time as part of her group, and I hope the best to her and her family after my departure from College Station.

Neither the right words nor enough time exists to fully convey my sincerest gratitude and feelings for the support, understanding, and love of my parents, James and Helen, my brother, Christopher, my sister, Rebecca, my precious Narda, Molly, and Bernoulli. Their various sacrifices on my behalf represent time that can never be returned, but will forever be remembered. Growing up with an astrophysicist Dad and a nurse anesthetist Mom, gave me, among other things, a unique and rare glimpse and immersion into science, mechanical systems, hard work, a constant strive for greater understanding, passion, and patience. I thank my Dad for the countless hours shared building a > 30ft free-standing playset (for starters), and for the oscilloscopes and assortment of equipment with buttons to play with before I could read or tie my shoes. I thank my Mom for passing along her work ethics, her conviction in fighting for what one believes in, and her Woodstock-sense of adventure. The love and acceptance from my parents are unparalleled sources of strength that I am honored and privileged to know. The support from, and bond with, my brother and sister throughout our lives together

continue to encourage my further growth as a scientist. I will forever be inspired by my dearest Narda, from her unparalleled rate of success and proficiency, her spirit, her love, and her companionship on our journey together. To that end, I must also thank The Twilight Zone, the Physics and Astronomy Department of Texas A&M University, and Mazda.

I acknowledge and am grateful for the support and friendship of Professor Michael Mason Kash, of Lake Forest College. It was during my time as his student that I was exposed to simply unrivaled laboratory practices and techniques. He is truly a Jedi master of physics and displays a love and care for students' understanding of material that all should strive to emulate. His support and time on my behalf made possible the success that I have experienced.

I thank Professor George R. Welch for his help and support during my time at Texas A&M. His fruitful and delightful conversations were among the best I experienced during my time here. It was comforting to know there was another experimentalist to talk to that understands the desire to work with something to the point of complete understanding at the risk of personal injury.

I must thank Robert Atkins, Dennie Spears, and Jim Gardner for their help with equipment support and encouraging conversations. I hope the best to all of them and their families.

I thank Sherree Kessler for her support during my time as a graduate student at Texas A&M University. Her encouragement and assistance with matters pertaining to the Physics and Astronomy department allowed me to continue to prosper within the department. She, as well as Michelle Sylvester, Heather Walker, Brendan Martin, Veronica Rodriguez, and Cheryl Picone, are wonderful members of the department that provided resources necessary for my success during my time in the department.

Lastly, I thank David Curie, Michaelangelo “Monty” Monterroso, and Anthony Valsamis, for their friendship and support. Our time at Lake Forest College instilled a greater understanding and appreciation of physics and Silo pizza.

CONTRIBUTORS AND FUNDING SOURCES

Contributors

This work was supported by a dissertation committee consisting of Professor Christi K. Madsen [advisor and co-chair] and Professor Philip Hemmer of the Department of Electrical and Computer Engineering, as well as Professor George R. Welch [chair] and Professor Alexey Belyanin of the Department of Physics and Astronomy.

Funding Sources

This work was made possible, in large part, through the generous support of Professor Christi K. Madsen, and a research assistantship through the Department of Electrical and Computer Engineering at Texas A&M University. This work was supported, in part, through funds made available by the Advanced Research Projects Agency - Energy (ARPA-E).

NOMENCLATURE

EIT – Electromagnetically-Induced Transparency

FLICE - Femtosecond Laser Irradiated Assisted Chemical Etching

FTIR – Frustrated Total Internal Reflection

FWHM – Full Width at Half Maximum

HRC – High Reflection Coating

IS – Integrating Sphere

LED – Light Emitting Diode

LP – Light Pipe

NPCBS – Non-Polarizing Cube Beam Splitter

PMMA – Poly(methyl methacrylate)

PTFE – Polytetrafluoroethylene, e.g. Teflon[®]

RMS – Root Mean Square

TE – Transverse Electric

TIR – Total Internal Reflection

TIS – Total Integrated Scattering, Total Integrated Scatter

TM – Transverse Magnetic

UV – Ultraviolet

TABLE OF CONTENTS

	Page
ABSTRACT	ii
DEDICATION	iii
ACKNOWLEDGMENTS.....	iv
CONTRIBUTORS AND FUNDING SOURCES.....	vii
NOMENCLATURE.....	viii
TABLE OF CONTENTS	ix
LIST OF FIGURES.....	xii
LIST OF TABLES	xviii
CHAPTER I INTRODUCTION TO LIGHT PIPES (LPS).....	1
1.1 Characteristics	4
1.2 Loss Mechanisms	7
Fresnel Reflection.....	10
Absorption.....	12
Total Integrated Scattering	15
Total Internal Reflection Violation	19
Evanescent Field.....	19
Frustrated Total Internal Reflection	22
Goos-Hänchen Shift	27
CHAPTER II OPTICAL PATH ELEMENTS	29
2.1 Sources	29
Spectral Irradiance.....	29
Étendue.....	31
Spatial Coherence.....	32
Numerical Aperture.....	32
2.2 Input Coupling.....	33
Lens Array Element.....	35
Ray Fan Producing Optics.....	37
Cylindrical Lens	37
Powell Lens	37

2.3 Detector	38
Acceptance Angle.....	38
Wavelength Dependence	38
Detection Area Homogeneity and Relationship to Illumination Area	38
Power Meter and Data Collection	39
2.4 Reference Path.....	41
2.5 Spectral Filtering.....	43
Monochromator	43
Ocean Optics Spectrometer	43
Optical Spectrum Analyzer	44
2.6 Calculating the Estimated Transmission	44
 CHAPTER III GLASS LPS FOR OPTICAL TESTING	 46
3.1 Light Pipe Assembly	47
Mounting Schemes	48
Optical Adhesives.....	54
End Facet Preparation	55
Cover Slips	55
Adhesive Endcaps	57
High Reflectance Coated Cover Slips and Crossbars	60
3.2 Module Assembly	60
Baseplate Preparation and Subsequent Light Pipe Alignment and Mounting	60
Total Module Alignment	62
 CHAPTER IV COLLIMATED BEAM - ANGULAR SWEEP CHARACTERIZATION	 64
4.1 Measurement Setup.....	64
Beam Divergence Characterization.....	66
θ Rotation Ability	67
ϕ Rotation Ability.....	68
Integrating Sphere (IS) Characterization and Performance Comparison With Photodiode Detector	69
4.2 Single Channel Light Pipe Measurement Results.....	73
Rectangular Prism Light Pipes	74
Light Pipes with 45 Degree Turning Surface	85
 CHAPTER V SPECTRAL CHARACTERIZATION	 90
5.1 Broadband Source Measurement Apparatus	90
5.2 Results	91
 CHAPTER VI PREPARATIONS TOWARD MULTI-LENS ELEMENT COUPLED TO MULTI-LUT - DETECTOR CHARACTERIZATION	 93

6.1 Experimental Arrangement	93
6.2 Silicon Photodiode	94
6.3 Results	98
CHAPTER VII SUMMARY, CONCLUSIONS, AND FUTURE WORK	100
REFERENCES	103
APPENDIX I 2D GEOMETRICAL AND MATHEMATICAL DESCRIPTIONS OF SINGULAR RAY TRAJECTORIES IN BASIC LIGHT PIPE STRUCTURES	107
A1.1 2D Rectangular Prism LP	107
A1.2 Rectangular LP with 45° Input Face	111
APPENDIX II LIBERATION PROCEDURE	121
APPENDIX III MICROSOFT EXCEL FORMULA FOR USE WITH THE ⊕ STAGE	124
APPENDIX IV NOTES REGARDING WORKING WITH NORLAND OPTICAL ADHESIVES	128

LIST OF FIGURES

	Page
Figure 1 Traditional LP / fiber optic anatomy.....	4
Figure 2 Refracted angle in fused silica when input medium is air ($n = 1$).	6
Figure 3 Internal propagation angle within LP for $\lambda = 514$ nm.....	7
Figure 4 Number of internal reflections in a rectangular prism LP when rays are launched at the center of the input face for an LP refractive index of 1.4616 surrounded by $n = 1$ (air).	9
Figure 5 Idealized Fresnel transmission through a window having $n_{window} = 1.4616$ surrounded by $n_{air} = 1$	11
Figure 6 Calculated transmission of light energy through a 20 mm x 1 mm x 1 mm sample of refractive index $n_{core} = 1.4616$ mounted on $n_{lower\ cladding} = 1.328 + ik$. Calculations include idealized Fresnel reflection losses at two interfaces. Light having a wavelength of 514 nm is considered. A smooth interface is assumed.	15
Figure 7 Contour plots of TIS for various rms surface roughness values showing the predicted power remaining in a specular beam after reflection.	17
Figure 8 TIS for light incident on a 50 mm x 1 mm x 1 mm LP having an RMS surface roughness of $\sigma = 10$ nm (top) and $\sigma = 100$ nm (bottom), accounting for the number of internal reflections and refraction upon entering.	18
Figure 9 Evanescent field penetration depth for $\lambda = 500$ nm incident from fused silica on a $n = 1.3685$ interface near the critical angle.	21
Figure 10 Wavelength dependence of evanescent field penetrating a fused silica / $n = 1.328$ boundary.	22
Figure 11 Frustrated total internal reflection. Light that is incident upon the n_1/n_2 interface satisfying TIR conditions tunnels across the n_2 barrier and into the n_3 region. Relating this to an LP in this work, the n_1 , n_2 , and n_3 regions would correspond to the core material, the mounting adhesive, and the mounting substrate, respectively.	23
Figure 12 FTIR into a mounting substrate when $n_2 = 1.327$. The calculated lines end at approximately the corresponding critical angle between n_1/n_2	25

Figure 13 FTIR into a mounting substrate when $n_2 = 1$. The calculated lines end at approximately the corresponding critical angle between n_1/n_2	26
Figure 14 Illustration of the Goos-Hänchen shift. Rather than reflect from the point of reflection, the ray reflects from a location shifted by a distance s corresponding to the apparent emergence point from reflection within the second medium.	28
Figure 15 Sample spectral profile of the CPS520 source as measured with a Thorlabs OSA 201 optical spectrum analyzer.	30
Figure 16 Example spectral output of monochromator delivery system used for testing. It should be noted that the profile depended on the coupling and alignment with the sampling spectrometer's input fiber.	30
Figure 17 Mechanical misalignment situations between two optical fibers that show (a) longitudinal misalignment, (b) lateral misalignment, and (c) angular misalignment.....	33
Figure 18 Polymer aspheric lens array made by Syntec Optics. One side of a hexagon is 6.2 mm in length, and the focal length of an individual lens element is 20.3 mm.....	36
Figure 19 Reference path of measurement apparatus.	42
Figure 20 LP endface quality before polishing processes. The top and bottom rows show samples created using different fabrication parameters and display a 1 mm^2 endface. The right column shows a zoomed in view of a selected region of a respective sample.	47
Figure 21 LP assembly stage shown with a vacuum pickup tool in place (left) and with a diamond scribe pen and translation stage-mounted vacuum chuck (right).	48
Figure 22 End-on view of a rectangular prism LP mounted in majority contact with a substrate. It should be noted that, for a given LP, one set of parallel sidewalls as well as both endfaces, will be polished post FLICE process and the remaining parallel sidewalls will possess very nearly the original substrate surface properties.....	51
Figure 23 Side view of a rectangular prism LP mounted in majority contact with a substrate.	51

Figure 24 Rectangular prism LP mounted on two crossbars. The cross bars are mounted on a borosilicate base, which is subsequently mounted, via double sided tape, to a bottom microscope slide for holding purposes.	52
Figure 25 LP with 45° face mounted on high reflection coated crossbar and utilizing a microscope slide cover slip at its output.	52
Figure 26 Two different methodologies to adhere a sample directly to a mounting substrate.	53
Figure 27 End-on depiction of adhesive displacement and migration along the vertical sidewalls of the LP.	53
Figure 28 Pedestal mounting structure to mitigate adhesive sidewall creep.	54
Figure 29 Microscope slide cover slip surface roughness enhancement concept.	55
Figure 30 Microscope slide cover slips as an LP endface enhancement – end view.	56
Figure 31 Microscope slide cover slips as an LP endface enhancement - side view.	56
Figure 32 Fresnel reflection loss comparison between microscope cover slips use on LP endfaces. The negligible change in angle due to refraction from the cover slips is considered. Calculations performed for 514 nm light and associated refractive indices. Perfect index matching at interfaces is assumed.	57
Figure 33 Adhesive-made endface caps production methodology.	58
Figure 34 White light interferometer created surface profile of adhesive endcap created with a non-ideal release agent.	59
Figure 35 White light interferometry created surface profile of adhesive endcap created using a silicone-based release agent.	59
Figure 36 Polymer sheet of $n = 1.327$	60
Figure 37 Baseplate alignment grid.	61
Figure 38 Total module testing apparatus.	63
Figure 39 Light pipe optical throughput measurement apparatus.	65
Figure 40 Divergence measurement apparatus.	66
Figure 41 Beam full angle divergence determination.	67

Figure 42 Rotation mount insert (top left) providing ϕ adjustment ability. Sample LP on mount in place within rotation stage (top right). 50 mm x 1 mm x 1 mm LP testing in situ (though translated out of the detector for the image) using insert and stage (bottom).....	68
Figure 43 Line-of-sight concern with integrating spheres that do not possess an internal baffle.....	70
Figure 44 Measured angular response of detectors.....	71
Figure 45 Detector performance comparison when a sample is in place. Note the dip at -50° when an integrating sphere is used.	72
Figure 46 LP Output clipping as a result of poor sample placement.	72
Figure 47 Axis and angular definitions for rectangular prism LPs.	73
Figure 48 Sign convention for 45° sample input angles.	73
Figure 49 Source comparison between a ~ 1 nm linewidth source (laser) and a ~ 30 nm linewidth source (monochromator output). The LP was mounted on top of a $200 \mu\text{m}$ deep notch cut in the mounting substrate.	75
Figure 50 Investigation of polarization dependence on LP transmission properties. The LP used was a 20 mm long sample where the original (i.e. non laser irradiated) sides were interrogated.....	76
Figure 51 70 mm LP mounted on non-coated crossbars (top) and during testing at $\theta = 45^\circ$ (bottom).	77
Figure 52 Scan interrogating original sides where one is mounted at two locations to non-coated crossbar supports through the use of a $n = 1.328$ adhesive.....	78
Figure 53 50 mm LP transmission results when the θ scanning plane is orthogonal to the polished sides (of which were facing air) of the LP. The errors bars in the golden plot indicate the latest data collection methodology was used in the measurement process.	79
Figure 54 50 mm LP transmission results when the θ scanning plane is orthogonal to the original sides of the LP (one, of which, being in contact with the crossbar supports). The errors bars in the golden plot indicate the latest data collection methodology was used in the measurement process.	80
Figure 55 Bond quality between the 50 mm sample and the two crossbar supports. The column on the left features images created using dark field	

microscopy, while the column on the right features images created using bright field microscopy.....	80
Figure 56 Loss model comparison with data for 50 mm LP. Measured and calculated curves correspond to $\lambda = 514$ nm. The critical angle indicated shows the required incident angle on the LP surface that corresponds to an internal propagation angle equal to the critical angle of the fused silica / adhesive interface. Note that the critical angle for a fused silica / air interface is not achievable even for extreme angles of incidence at the LP input. An RMS surface roughness of 6.36 nm is assumed in all cases.....	82
Figure 57 50 mm LP results utilizing the full angular (φ in addition to θ) ability of the testing apparatus.	85
Figure 58 Transmission results of LPs containing a 45° turning surface under various preparation configurations.	86
Figure 59 Relationship between the angle incident on the input surface of a 45° sample and the angle incident on the turning surface.....	88
Figure 60 Top view depiction of mounting block used to hold 45° containing LPs via vacuum.....	89
Figure 61 Broadband transmission measurement apparatus.	90
Figure 62 Broadband testing result as a function of incidence angle using a 50 mm x 1 mm x 1 mm sample.....	92
Figure 63 Block diagram of single channel LP photodiode testing apparatus.....	94
Figure 64 Amplifier circuit used with photodiodes for testing solar module performance.	96
Figure 65 Arduino/protoboard layout of amplifier circuits used with the silicon photodiodes.....	96
Figure 66 Total module testing apparatus with silicon photodiodes attached to provide at-lens and after-lens reference values.	97
Figure 67 Lens element characterization.....	99
Figure 68 Angular definitions in rectangular prism LP.	107
Figure 69 Angular definitions in rectangular LP with an angled face (45°) for light incident on the central location.....	111

Figure 70 Quantities used to determine the number of internal reflections in a 45° LP.....	113
Figure 71 2D Tapered LP	115
Figure 72 Propagation cases in 2D tapered LP.	116
Figure 73 Case 1.....	117
Figure 74 Internal reflections in 2D taper. The illustrated propagation is non-physical in the sense that the reflection angles have been drawn to allow for room for labels.	118
Figure 75 Example θ stage angle calculation spreadsheet.	124
Figure 76 Counting dial/knob used with the theta rotation stage.....	125

LIST OF TABLES

	Page
Table 1 Selected mounting arrangements for LP testing.	50
Table 2 Various Norland Products Inc. optical adhesives and associated properties.	54
Table 3 Properties pertaining to tested, non-identical, LPs containing a 45° turning surface tested with 514 nm center wavelength light.....	87
Table 4 Results of silicon photodiode testing of 45° containing LP.	98

CHAPTER I

INTRODUCTION TO LIGHT PIPES (LPS)

At their most basic level, light pipes serve the very important purpose of guiding light from one place to another. The details of such a function vary depending on application. Two popular modern day uses of LPs are beam homogenizers [1] and, as is the context of this work, as solar concentrators [3]-[5]. Examples of LPs can be found in vehicle cabin illumination systems (dashboard and button illumination), illuminated buttons on electronic devices, pool and spa lighting, liquid crystal backlights, projection systems, and in luminaries, to name a few [2]. Often, this is accomplished through reflection means, where light enters and propagates through a LP via a series of internal reflections. A common example is that of a fiber optic cable, where light is confined in a core region surrounded by a material of lower refractive index. LPs utilize the same scheme, but a notable difference is that their cladding is often air, which allows for much smaller critical angles between the core/cladding interface thereby allowing light to propagate at steeper incidence angles. Additionally, the higher refractive index ratio between the core and cladding allows for greater numerical apertures to be achieved when compared with standard fiber optics. This is of paramount importance and utility when it comes to light guiding applications for solar concentrators whose concentration factors necessitate greater acceptance angles of the receiving/guiding LPs. While fiber optics are examples of LPs, the term “light pipe” usually refers to structures with cross-sections an order of magnitude or greater than those belonging to standard optical fibers.

As such, LPs are highly multi-moded, inherently unlike single mode fibers, and support orders of magnitudes of modes above that of a standard multimode fiber. This makes transmission/performance predictions based on modal analysis a daunting and highly complex feat that has not been accomplished in a rapidly applicable way, especially for complex geometries. Because of this, characterization of LP performance and transmission estimation is often carried out using ray optics based software analysis packages. Many LPs today are made from Poly(methyl methacrylate) (PMMA) or other polymer [2] which have the attractive feature of being less expensive than their fused silica counterparts in terms of raw material costs, but their absorption properties in the ultraviolet (UV) lead to decreased transmission performance and change of refractive index [12], as well as their susceptibility to thermal degradation at comparably low temperatures [13] being far greater, make polymer-based LPs less practical for solar light guiding applications than fused silica based LPs. With advancements in glass processing, such as the FLICE method [14], fused silica LPs of longer lengths and more complex geometries can now be realized. This furthers the need for optical characterization and transmission estimation in order to aid in LP design and testing. Clear loss dependencies on input/output facet and sidewall surface roughness (through scattering and ray deflection) have been shown for optical LPs [6]-[11]. In order to develop a loss model that accurately predicts and accounts for the performance of a given LP, careful transmission measurements must be made. It is the aim of this work to provide a basis for such measurements. As LPs differ from standard fiber optics in design and implementation, they also differ in conventional transmission testing. Fiber

optics are generally designed to transport light over great distances via a structure whose core/cladding cross section is constant and symmetrical, lending itself to standard testing methods such as the cut-back method wherein a length of fiber is subsequently cut back to provide transmission information as a function of length. Since most LPs are intended to operate under specific dimensional constraints, and sometimes do not have a constant cross section (as in the case of solar concentrator or homogenizer designs), standard optical fiber testing methods cannot be easily extended to LPs. A previous group has worked on characterizing loss within a LP with attention paid to bending geometry [6], but the work does not relate overall end to end performance to a physical sample using measured data. Similar statements can be made regarding [9]. Another group has made measurements pertaining to coupling/insertion losses of a light guiding device [9], but the treatment does not consider free-space coupling of input light over multiple incidence angles. Such a treatment is found in [10], but does not have the multi-wavelength testing ability presented in this work and also lacks a second rotation axis to provide incidence angles in any plane of choice. [25]-[28] utilize a system to launch rays at a desired angle into single mode fibers (i.e. symmetric cladding conditions) but their system comprises only one rotation axis.

This work is aimed at providing a common-ground basis for the transmission/loss characterization of optical LPs. While the work is generally applicable to a wide variety of LPs, some emphasis is placed on the particular application of a high concentration factor solar concentrating design [4]-[5].

1.1 Characteristics

As mentioned in the introduction to this chapter, LPs have multiple commonalities with fiber optic transmission lines, and utilize standard geometrical optics definitions to facilitate general analysis. **Figure 1** shows a cutaway side view of a common optical fiber having a constant cross section.

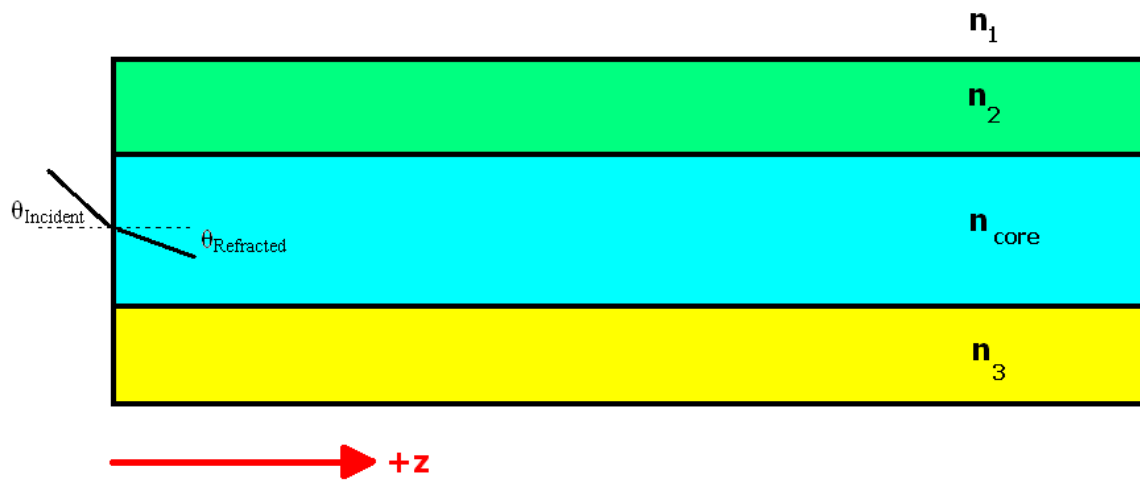


Figure 1 Traditional LP / fiber optic anatomy.

For a standard fiber optic cable providing light propagation ability through total internal reflection (TIR) means, the refractive indices are such that $n_2 = n_3 < n_{\text{core}}$, where n_2 and n_3 constitute the coaxial cladding of the cable. The refracted angle of the light upon entry into the core region is found through Snell's Law and is

$$\theta_{\text{Refracted}} = \sin^{-1}\left(\frac{n_1 \sin(\theta_1)}{n_{\text{core}}}\right). \quad (1.1)$$

The image space numerical aperture is geometrically defined as

$$NA = n_1 \sin(\alpha), \quad (1.2)$$

where α is the half angle of the fan of light that can enter the core region. For standard optical fibers whose core diameter is large compared to the wavelength of light being launched into the fiber, this is commonly expressed as

$$NA = \frac{1}{n_1} \sqrt{n_{core}^2 - n_{cladding}^2}. \quad (1.3)$$

For a given interface, the condition for TIR to take place is that the angle of the light incident upon the interface be greater than the critical angle, defined as

$$\theta_{critical} = \sin^{-1}\left(\frac{n_2}{n_1}\right), \quad (1.4)$$

where n_1 is the index of refraction of the medium the light was traveling in prior to the interface, and n_2 is the index of refraction of the medium after the interface. Note that TIR only takes place when $n_2 < n_1$. Light, upon entering another medium, will undergo refraction and will leave the interface at a new angle related by Snell's Law as

$$\theta_{refracted} = \sin^{-1}\left(\frac{n_1 \sin(\theta_{incident})}{n_2}\right) \quad (1.5)$$

An example of this relationship for fused silica is shown in **Figure 2**, where the wavelength-dependent refractive index of fused silica from the database at [17] was used.

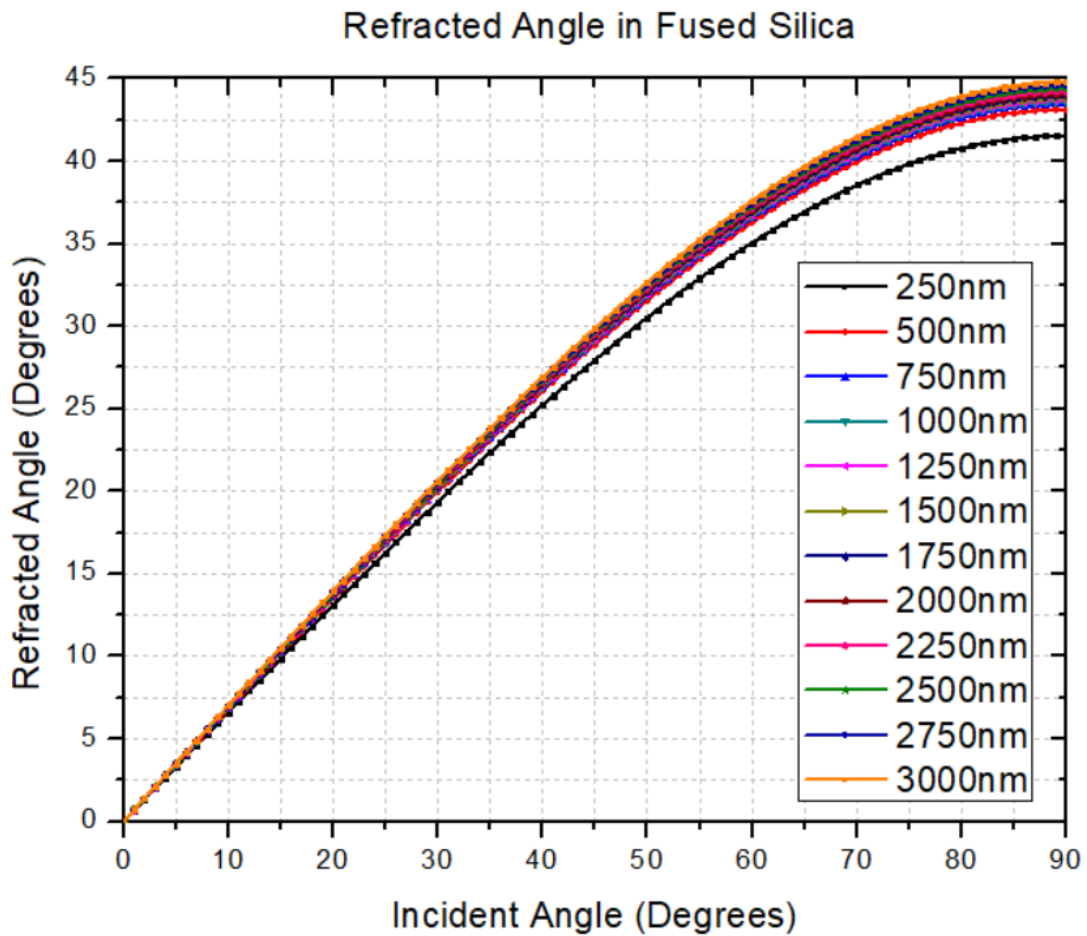


Figure 2 Refracted angle in fused silica when input medium is air ($n = 1$).

After entering the LP, the light will propagate along the length of the LP by way of TIR at an internal propagation angle equal to the complement of the refracted angle. This relationship is shown in **Figure 3**.

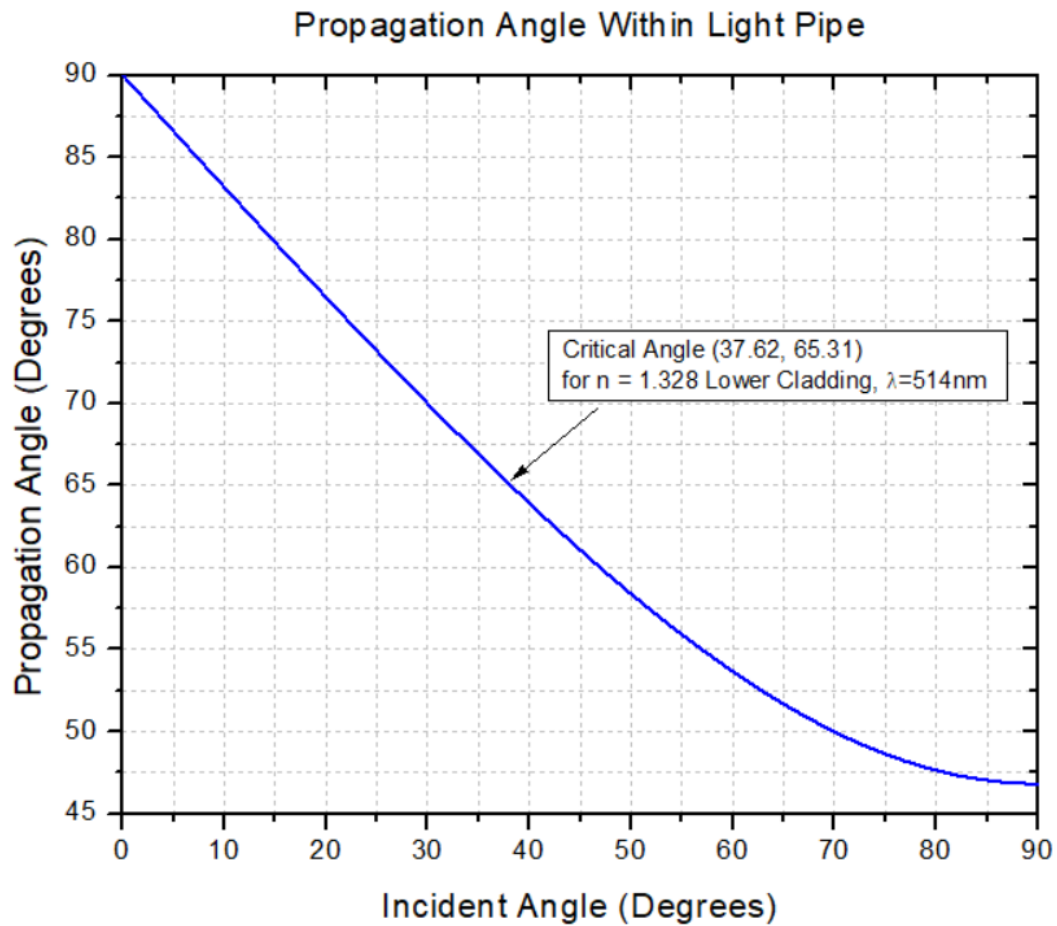


Figure 3 Internal propagation angle within LP for $\lambda = 514$ nm.

1.2 Loss Mechanisms

Light is lost from entrance to exit of a LP through various means. Understanding these loss mechanisms is critical to efficient light pipe design and provides a basis for comparison between estimated design performance and measured performance data. The main loss mechanisms considered here are Fresnel reflection, material absorption, scattering represented by Total Integrated Scattering (TIS), violation of TIR conditions,

and Frustrated Total Internal Reflection (FTIR). The overall transmission of a light pipe will be determined in terms of these loss mechanisms as

$$P_{transmitted} = (P_{incident}) \prod_i^n (1 - i), \quad (1.6)$$

Where each element of the product is the loss (from zero to one) imparted for the respective loss mechanism. In actuality, each mechanism is dependent on wavelength, location, and angular distribution, all of which are not necessarily constant during propagation. Some of these loss mechanisms are dependent on the number of internal reflections within a given LP. For a LP with a constant square cross section, the number of non-endface internal reflections when light is launched at the center is shown through geometry and Snell's law to be (see Appendix I for further details),

$$N = 1 + \left\lfloor \frac{1}{2} \left(\left(\frac{h}{2} \right)^{-1} L \tan \left(\sin^{-1} \left[\frac{\sin(\theta_1) n_1}{n_2} \right] \right) - 1 \right) \right\rfloor, \quad (1.7)$$

where h is the height of the input face (1 mm in the case of the LPs presented in this work), L is the length of the LP, θ_1 is the incident angle on the input surface of the light pipe, n_1 is the index of refraction of air (or surrounding atmosphere), and n_2 is the index of refraction of the LP material (fused silica in the context of this work). The sum includes the use of a floor function due to the integer nature of reflections. A plot of this equation utilizing various parameters is found in **Figure 4**. The step-like nature of the plots is due to the fact that the number of internal reflections does not change over small incidence angle ranges. Furthermore, horizontal asymptotes exist due to the finite length of the examples shown, as well as the limit to the propagation angle imposed by the

refracted angle in the medium (see **Figure 2**). The following condition is required in order for an internal reflection to take place,

$$L > \frac{3h}{2 \tan \left(\sin^{-1} \left[\frac{\sin(\theta_1) n_1}{n_2} \right] \right)} \quad (1.8)$$

One can more easily connect with equation (1.8) if they consider the fact that light at direct incidence will propagate through a LP without reflecting from its sidewalls.

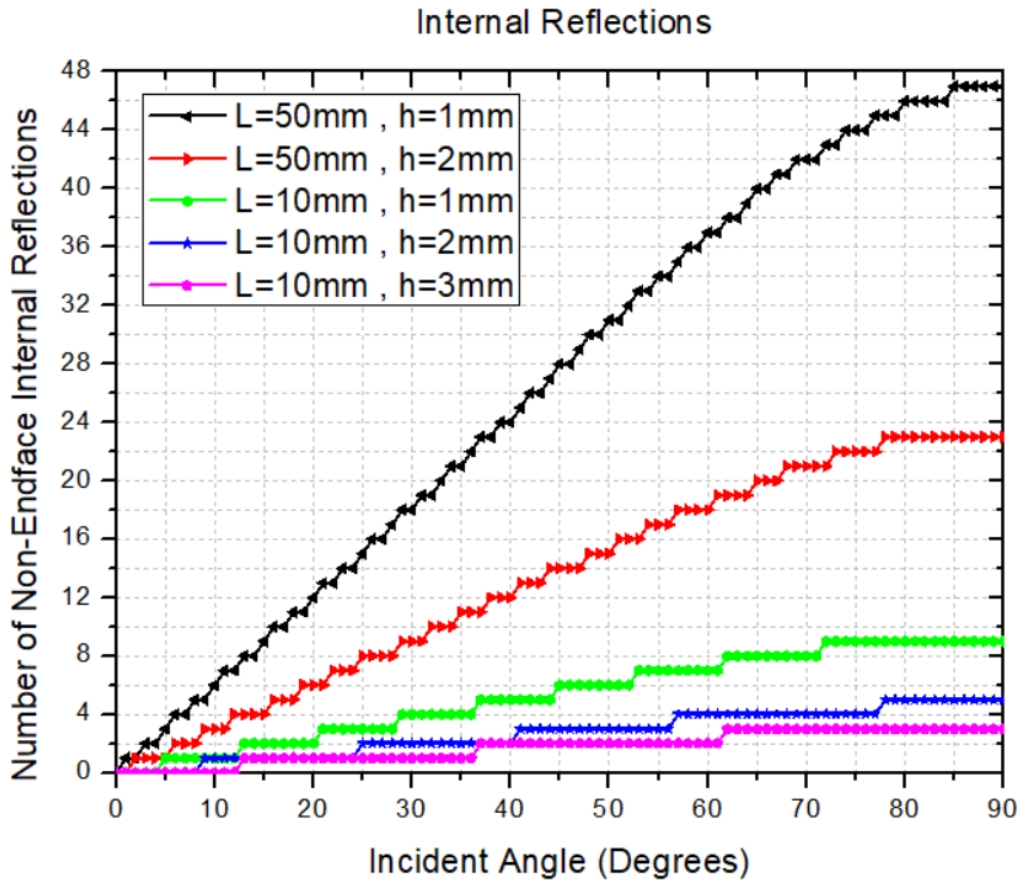


Figure 4 Number of internal reflections in a rectangular prism LP when rays are launched at the center of the input face for an LP refractive index of 1.4616 surrounded by $n = 1$ (air).

Fresnel Reflection

When light propagates from one medium to another, a percentage of light is reflected, rather than transmitted, and is dependent upon the angle of incidence on the interface. This is commonly referred to as Fresnel reflection. In the context of LPs, this plays a significant role in loss at the LP's input and output faces. For light of a transverse magnetic (TM) polarization, the Fresnel reflection is given as

$$R_p = \left| \frac{n_1 \sqrt{1 - \left(\frac{n_1}{n_2} \sin(\theta_i)\right)^2} - n_2 \cos(\theta_i)}{n_1 \sqrt{1 - \left(\frac{n_1}{n_2} \sin(\theta_i)\right)^2} + n_2 \cos(\theta_i)} \right|^2 \quad (1.9)$$

For light of a transverse electric (TE) polarization, the Fresnel reflection is given as

$$R_s = \left| \frac{n_1 \cos(\theta_i) - n_2 \sqrt{1 - \left(\frac{n_1}{n_2} \sin(\theta_i)\right)^2}}{n_1 \cos(\theta_i) + n_2 \sqrt{1 - \left(\frac{n_1}{n_2} \sin(\theta_i)\right)^2}} \right|^2 \quad (1.10)$$

With the average Fresnel reflection being

$$R_{average} = \frac{R_s + R_p}{2} \quad (1.11)$$

Therefore, when considering the light transmitted through an interface, one uses the quantity

$$T = 1 - R_{average} \quad (1.12)$$

It is important to remind the reader that only in the case of power can one make the statement that $1-R=T$. For complex field amplitudes, there is a refractive index and

angle dependent correction coefficient for T, due to the fact that light will propagate with different speed and direction in the second medium. An example of the idealized Fresnel transmission for light incident on a window of finite width that has an index of refraction of $n = 1.4616$ (the index of refraction of fused silica at 514 nm according to [17]) is shown in **Figure 5**.

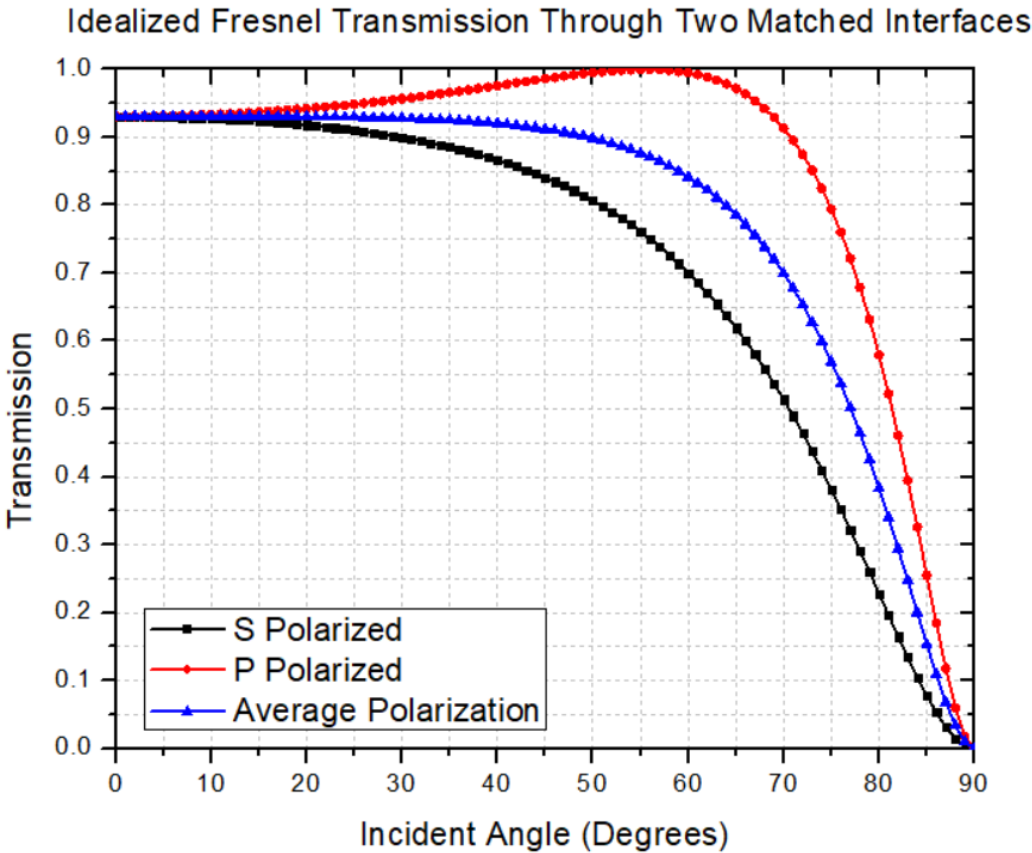


Figure 5 Idealized Fresnel transmission through a window having $n_{window} = 1.4616$ surrounded by $n_{air} = 1$.

For a collection of rays, a distribution of ray angles, as well as the associated power distribution, needs to be considered in order to more accurately predict the loss from the reflection from an LP input. In this case, the transmission through an interface will be

$$T = 1 - \sum R(\theta_n)P(\theta_n) \quad (1.13)$$

where $R(\theta)$ is the angle-dependent Fresnel reflection, and $P(\theta)$ is the angle-dependent power distribution of the beam and is largely a function of the beam divergence and optics used to deliver the beam. The unity term on the right hand side refers to the total optical power incident on the interface and will become a variable itself, in practice, as a reference measurement of the total power which it represents will be dependent on detector properties.

Absorption

In general, absorption is considered to be the effect by which light interacting with a given medium is attenuated through various mechanisms. This effect manifests itself in two ways in this work. The first of which, is the attenuation of the light energy traveling in the core material itself. The other way this effect comes into play, is in the reflection from an absorbing medium, such as an absorbing cladding layer, during an internal reflection of the light within a LP. In the former case, the bulk material's wavelength-dependent attenuation coefficient is used to describe this behavior. The loss model, for which, takes on an exponential form, as is common. In the latter case, the loss dependence can be treated using Fresnel reflection equations that take the complex (i.e. Real and Imaginary components) nature of the wavelength-dependent refractive indices

into account and, in doing so, describe the reflection loss for metals and other absorbing media. For TM-polarized light incident from a lossless medium having a refractive index of n_1 upon a metallic or otherwise absorbing interface having a refractive index of n_2 , the reflection coefficient is given as (adapted from [16])

$$r_{TM} = \frac{-(n_2^2 + 2n_2k_2i - k_2^2)\cos(\theta) + n_1\sqrt{n_2^2 - k_2^2 - n_1^2\sin^2(\theta) + i2n_2k_2}}{(n_2^2 + 2n_2k_2i - k_2^2)\cos(\theta) + n_1\sqrt{n_2^2 - k_2^2 - n_1^2\sin^2(\theta) + i2n_2k_2}}, \quad (1.14)$$

where θ is the angle of incidence on the interface measured with respect to surface normal and k_2 is the Imaginary component of the complex refractive index of the second medium. For TE-polarized light in this situation, the reflection coefficient is given as

$$r_{TE} = \frac{n_1\cos(\theta) - \sqrt{n_2^2 - k_2^2 - n_1^2\sin^2(\theta) + i2n_2k_2}}{n_1\cos(\theta) + \sqrt{n_2^2 - k_2^2 - n_1^2\sin^2(\theta) + i2n_2k_2}}. \quad (1.15)$$

The reflection as a value from zero to one is given by

$$R = |r|^2. \quad (1.16)$$

For the sake of completeness, the reflection for these two polarization states are given thusly as

$$R_{TM} = \frac{\left[(-n_2^2 + k_2^2)\cos(\theta) + n_1(A^2 + B^2)^{1/4}\cos\left(\frac{1}{2}\tan^{-1}\left(\frac{B}{A}\right)\right)\right]^2 + \left[\sin\left(\frac{1}{2}\tan^{-1}\left(\frac{B}{A}\right)\right)n_1(A^2 + B^2)^{1/4} - 2n_2k_2\cos(\theta)\right]^2}{\left[(n_2^2 - k_2^2)\cos(\theta) + n_1(A^2 + B^2)^{1/4}\cos\left(\frac{1}{2}\tan^{-1}\left(\frac{B}{A}\right)\right)\right]^2 + \left[\sin\left(\frac{1}{2}\tan^{-1}\left(\frac{B}{A}\right)\right)n_1(A^2 + B^2)^{1/4} + 2n_2k_2\cos(\theta)\right]^2} \quad (1.17)$$

and

$$R_{TE} = \frac{\left[n_1\cos(\theta) - (A^2 + B^2)^{1/4}\cos\left(\frac{1}{2}\tan^{-1}\left(\frac{B}{A}\right)\right)\right]^2 + \left[-\sin\left(\frac{1}{2}\tan^{-1}\left(\frac{B}{A}\right)\right)(A^2 + B^2)^{1/4}\right]^2}{\left[n_1\cos(\theta) + (A^2 + B^2)^{1/4}\cos\left(\frac{1}{2}\tan^{-1}\left(\frac{B}{A}\right)\right)\right]^2 + \left[\sin\left(\frac{1}{2}\tan^{-1}\left(\frac{B}{A}\right)\right)(A^2 + B^2)^{1/4}\right]^2}, \quad (1.18)$$

where

$$A = n_2^2 - k_2^2 - n_1^2 \sin^2(\theta), \quad (1.19)$$

and

$$B = 2n_2k_2. \quad (1.20)$$

If evaluating this function with a computer, make sure to take note of the appropriate quadrant associated with the arctan function in this case (i.e. it is more appropriate to use “ATAN2” versus “ATAN” in some software environments). An example of the above treatment is applied to a 20 mm x 1 mm x 1 mm LP mounted on an absorbing medium in **Figure 6**. Here, if we reference the depiction in **Figure 1**, $n_2 = 1$ (air), $n_{core} = 1.4616$, and $n_3 = 1.328 + ik$. Note that, in the case of $k = 0$ which corresponds to a non-absorbing medium, the transmission behavior reduces to that of basic Fresnel reflection as the Fresnel reflection from the LPs two endfaces are included in the calculation. A vertical asymptote exists at the angle corresponding to the internal propagation angle that matches the critical angle of the interface.

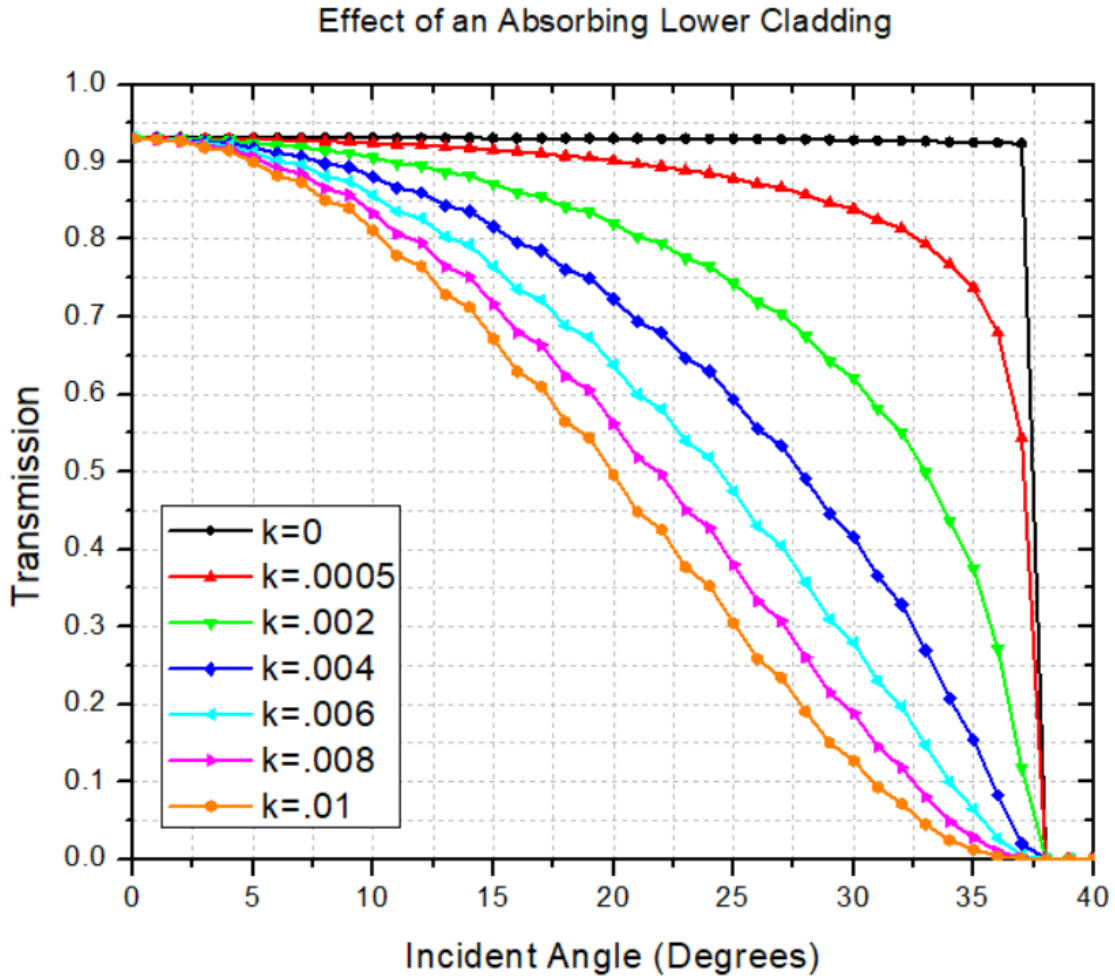


Figure 6 Calculated transmission of light energy through a 20 mm x 1 mm x 1 mm sample of refractive index $n_{core} = 1.4616$ mounted on $n_{lower\ cladding} = 1.328 + ik$. Calculations include idealized Fresnel reflection losses at two interfaces. Light having a wavelength of 514 nm is considered. A smooth interface is assumed.

Total Integrated Scattering

While finite surface roughness contributes to LP loss, it is a complex and rich topic in its own right, and one that spans many volumes of textbooks, dissertations, journal articles, etc. and will only be touched on briefly here in the context of total integrated scattering,

which is also referred to sometimes as total integrated scatter (both abbreviated by TIS). From [18], “the fraction of the total reflected radiant power remaining in the specular beam after reflection from a single moderately rough surface is given by”

$$\frac{R_s}{R_t} = e^{-\left(\frac{4\pi\sigma \cos(\theta_{incident})}{\lambda}\right)^2}, \quad (1.21)$$

where R_s is the specular reflectance, R_t is the total reflectance, $\theta_{incident}$ is the angle incident on the interface, σ is the root-mean-square surface roughness (RMS) surface roughness of the interface, and λ is the wavelength of the light incident on the interface. The referenced literature describes the validity and conditions of this widely used relationship. Examples of this relationship follow in **Figure 7**.

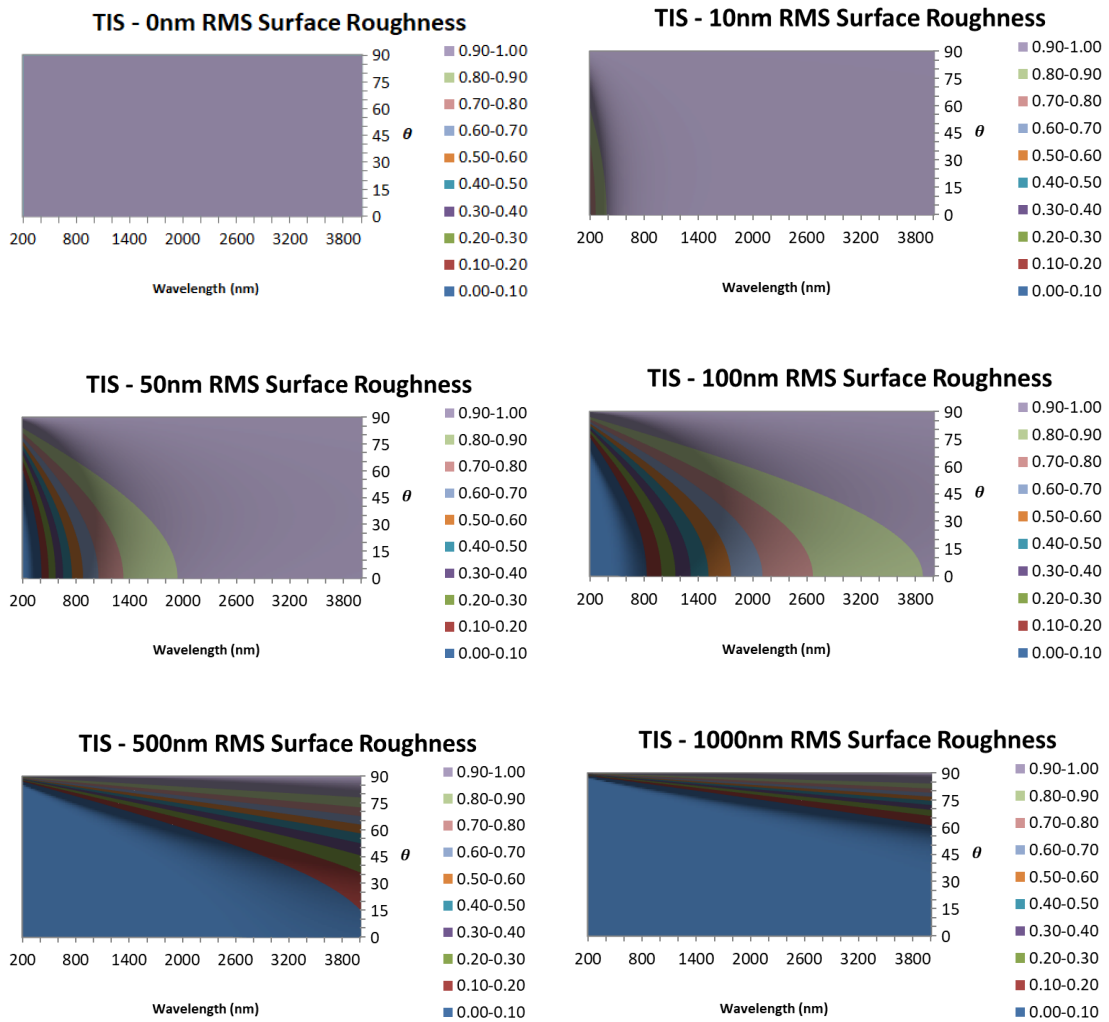


Figure 7 Contour plots of TIS for various rms surface roughness values showing the predicted power remaining in a specular beam after reflection.

Figure 8 shows the effect of TIS on light propagating through a LP of dimensions 50 mm x 1 mm x 1 mm, where the number of internal reflections and the refracted angle upon entering are taken into account.

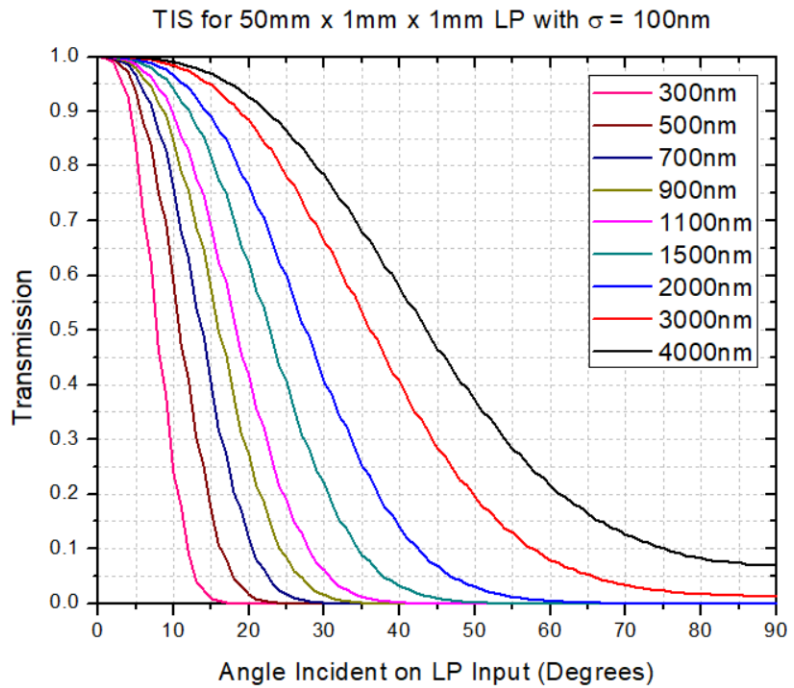
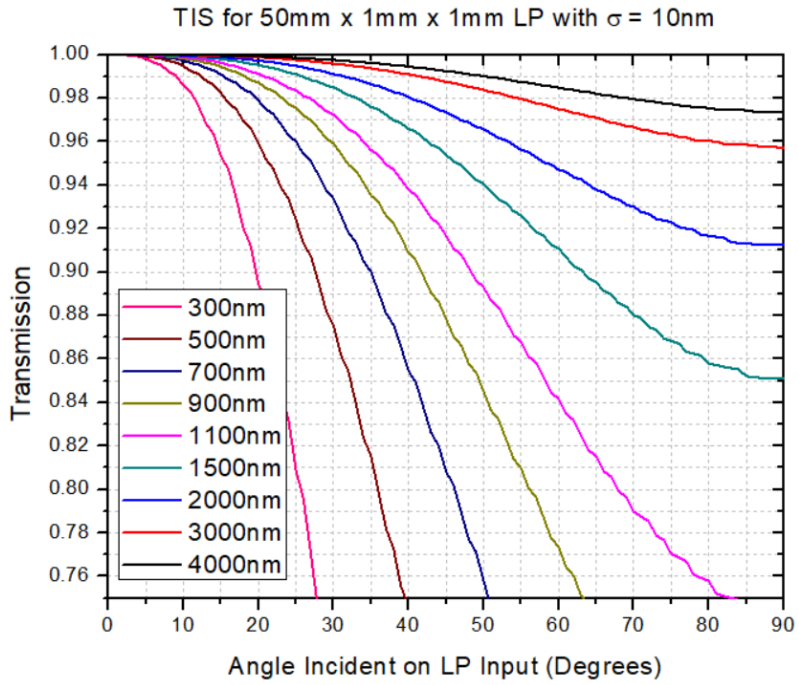


Figure 8 TIS for light incident on a 50 mm x 1 mm x 1 mm LP having an RMS surface roughness of $\sigma = 10\text{ nm}$ (top) and $\sigma = 100\text{ nm}$ (bottom), accounting for the number of internal reflections and refraction upon entering.

Total Internal Reflection Violation

As LPs perform their function of guiding light from their input to their output through the phenomenon of TIR, any violation of the TIR condition, namely that the light incident on an internal surface of the LP be greater than the critical angle between the boundary, will result in the vast majority of light being lost to the cladding. While the selection of cladding properties (such as the wavelength dependent complex refractive index) and geometries are optimized, TIR violations can occur as the result of LP core form deviations introduced in the polishing process, geometry changes of the cladding (perhaps due to excess optical adhesive finding its way to an undesired location) and random nicks and scratches that might be present on an LP surface as the result of cleaning and/or damage.

Evanescent Field

Light incident at the interface between a high refractive index region and one with a lower refractive index will undergo a phenomenon referred to as tunneling whereby the light, classically understood to be totally internally reflected at such a boundary when incident at an angle larger than the critical angle, penetrates beyond the boundary by some amount. The depth to which the transmitted wave penetrates such a barrier corresponding to a decrease in amplitude to 1/e its original amplitude can be shown to be [16]

$$|z| = \frac{\lambda}{2\pi \sqrt{\frac{\sin^2(\theta)}{n^2} - 1}} \quad (1.22)$$

where λ is the wavelength of light, θ is the angle of incidence on the interface, and n is the ratio of the refractive indices n_2/n_1 . Assuming a third medium is not close by and the second medium is not absorbing, the energy of the evanescent wave will return to the original medium. This phenomenon is of importance when one considers the cladding and mounting arrangements of LPs. Examples of this behavior are presented in **Figure 9** and **Figure 10** where the $1/e$ penetration depth is shown for a given wavelength as a function of incidence angle, and also as a function of wavelength for given distances away from the critical angle, respectively. As one would predict, significant penetration takes place very near the critical angle. This development and associated calculations provide a basis for establishing a minimum acceptable thickness for a given cladding layer, in order to avoid unwanted loss through leakage beyond a core/cladding barrier. In addition, they provide estimated for anticipated path lengths in a cladding material which can facilitate absorption related loss analysis.

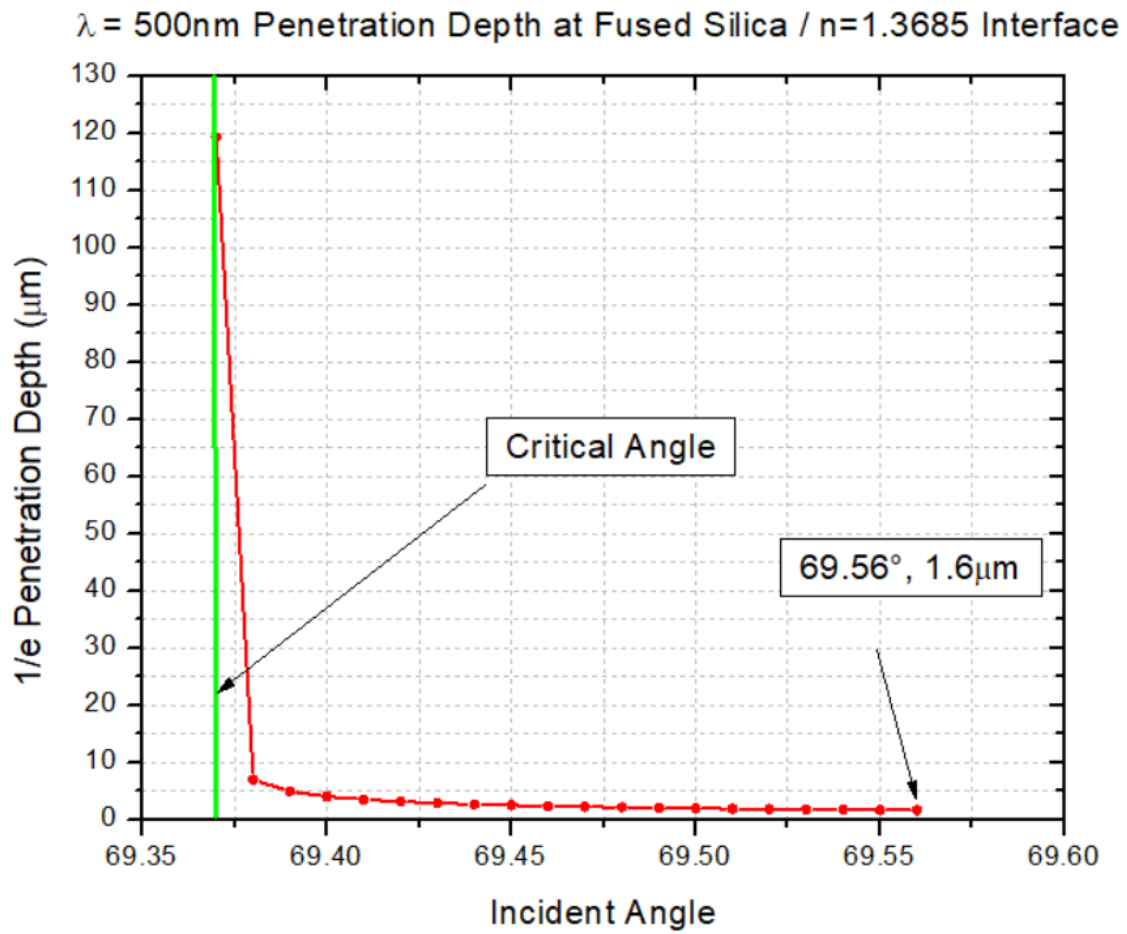


Figure 9 Evanescent field penetration depth for $\lambda = 500\text{ nm}$ incident from fused silica on a $n = 1.3685$ interface near the critical angle.

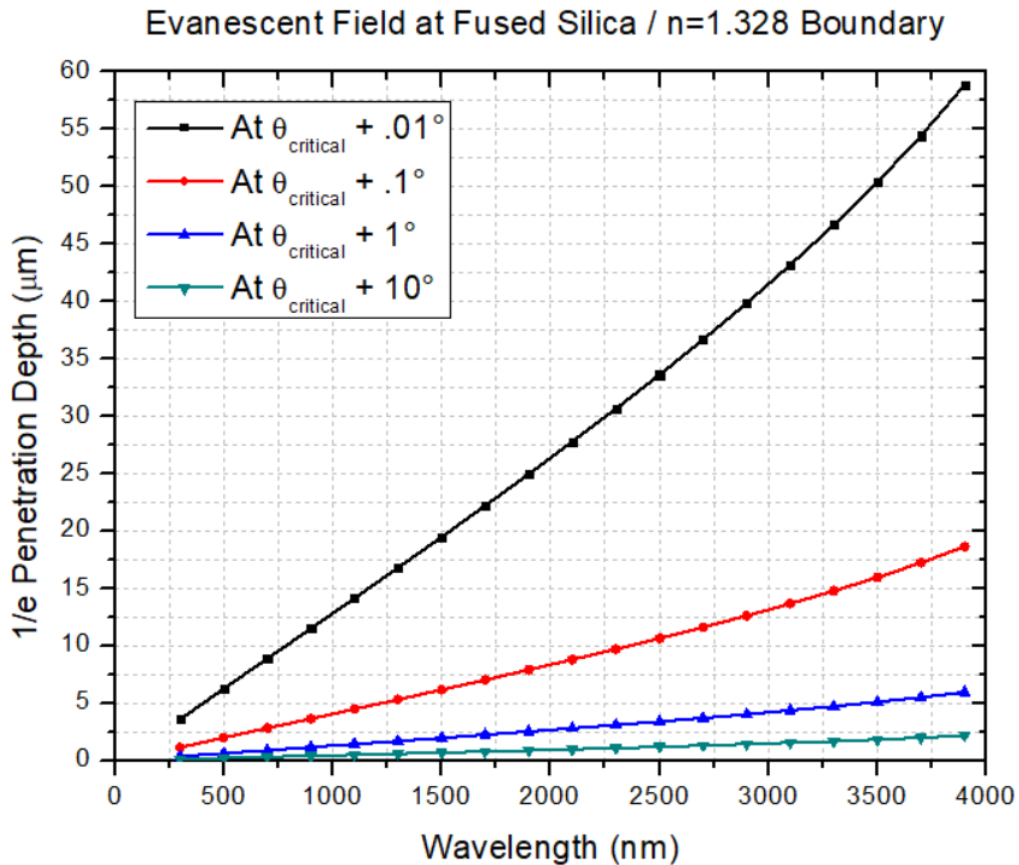


Figure 10 Wavelength dependence of evanescent field penetrating a fused silica / $n = 1.328$ boundary.

Frustrated Total Internal Reflection

Frustrated Total Internal Reflection (FTIR) is the phenomenon in which light that is incident upon a barrier at an angle larger than the critical angle of that n_1/n_2 interface tunnels through the interface and into the region beyond the n_2/n_3 interface as illustrated in **Figure 11**. This effect is important in planning and designing mounting specifics for a LP. If, for example, an LP were to be mounted using an adhesive of lower refractive index than the LP material (as is the case to provide TIR), and the adhesive layer were

too thin, light will tunnel beyond the adhesive and into the substrate potentially resulting in the throughput of the LP suffering enormously.

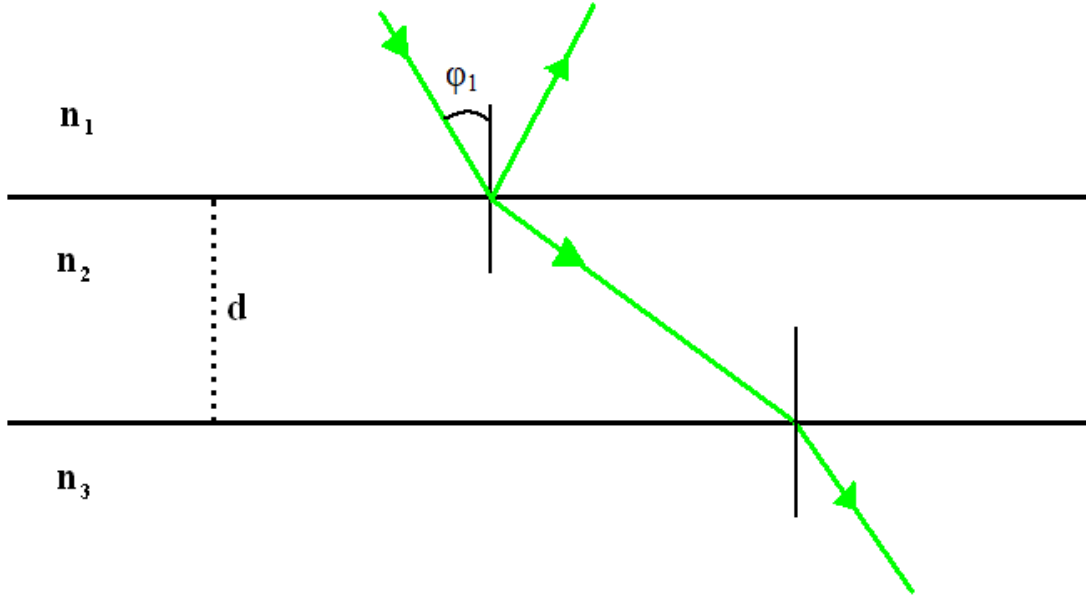


Figure 11 Frustrated total internal reflection. Light that is incident upon the n_1/n_2 interface satisfying TIR conditions tunnels across the n_2 barrier and into the n_3 region. Relating this to an LP in this work, the n_1 , n_2 , and n_3 regions would correspond to the core material, the mounting adhesive, and the mounting substrate, respectively.

The pertinent equation used to describe the FTIR transmission into the third medium is reproduced here from [14] as

$$T = [\alpha \sinh^2(y) + \beta]^{-1}, \quad (1.23)$$

where

$$\alpha_{\perp} = \frac{(N^2 - 1)(n^2 N^2 - 1)}{4N^2 \cos(\phi_1)(N^2 \sin^2(\phi_1) - 1)(n^2 - \sin^2(\phi_1))^{1/2}}, \quad (1.24)$$

$$\alpha_{parallel} = \frac{\alpha_{\perp}}{n^2} \left[(N^2 + 1) \sin^2(\phi_1) - 1 \right] \left[(n^2 N^2 + 1) \sin^2(\phi_1) - n^2 \right], \quad (1.25)$$

$$\beta_{\perp} = \frac{\left[(n^2 - \sin^2(\phi_1))^{1/2} + \cos(\phi_1) \right]^2}{4 \cos(\phi_1) (n^2 - \sin^2(\phi_1))^{1/2}}, \quad (1.26)$$

$$\beta_{parallel} = \frac{\left[(n^2 - \sin^2(\phi_1))^{1/2} + n^2 \cos(\phi_1) \right]^2}{4 n^2 \cos(\phi_1) (n^2 - \sin^2(\phi_1))^{1/2}}, \quad (1.27)$$

$$y = \frac{2\pi d}{\lambda} (n_1^2 \sin^2(\phi_1) - n_2^2)^{1/2}, \quad (1.28)$$

and,

$$n = \frac{n_3}{n_1}, \quad N = \frac{n_1}{n_2}. \quad (1.29)$$

Example plots using these equations applied to light pipes mounted on borosilicate glass using a binding medium having a refractive index of $n = 1.327$ are shown in **Figure 12** and in **Figure 13** which describe the transmission into the third medium upon a single internal reflection. Both of these plots are created using the angle of incident on a LP input, and the corresponding calculation is carried out using the appropriate refracted angle. This is why the plots suddenly stop at different locations, as the critical angle where this happens is, of course, wavelength-dependent. Beyond the critical angle, light is expected to penetrate fully from the LP core material into the second medium, where it is then expected to penetrate fully into the third medium (recall that $n_3 > n_2$ for the case of a borosilicate mounting substrate in the wavelengths of interest) when reflection, scattering, and absorption at each interface are not considered.

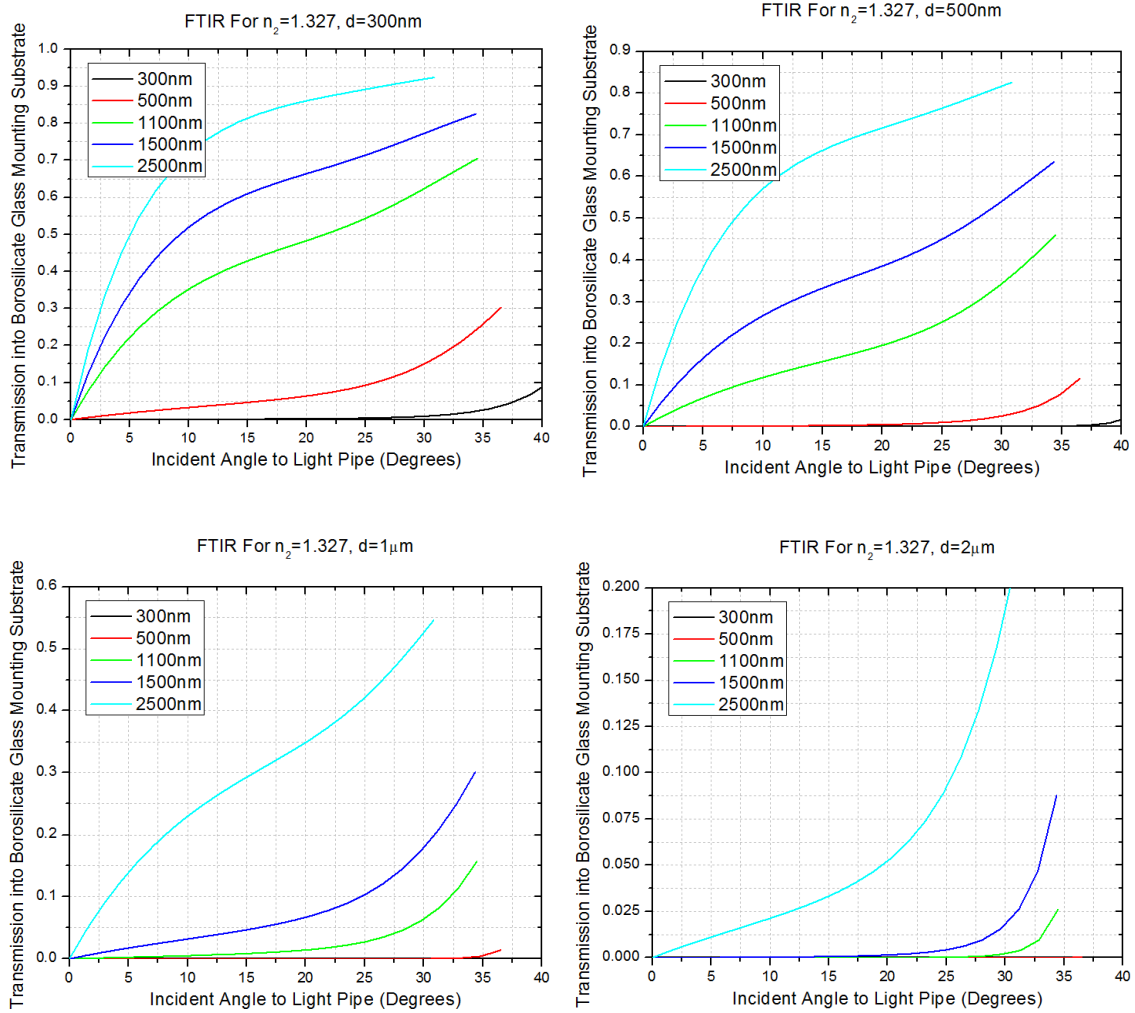


Figure 12 FTIR into a mounting substrate when $n_2 = 1.327$. The calculated lines end at approximately the corresponding critical angle between n_1/n_2 .

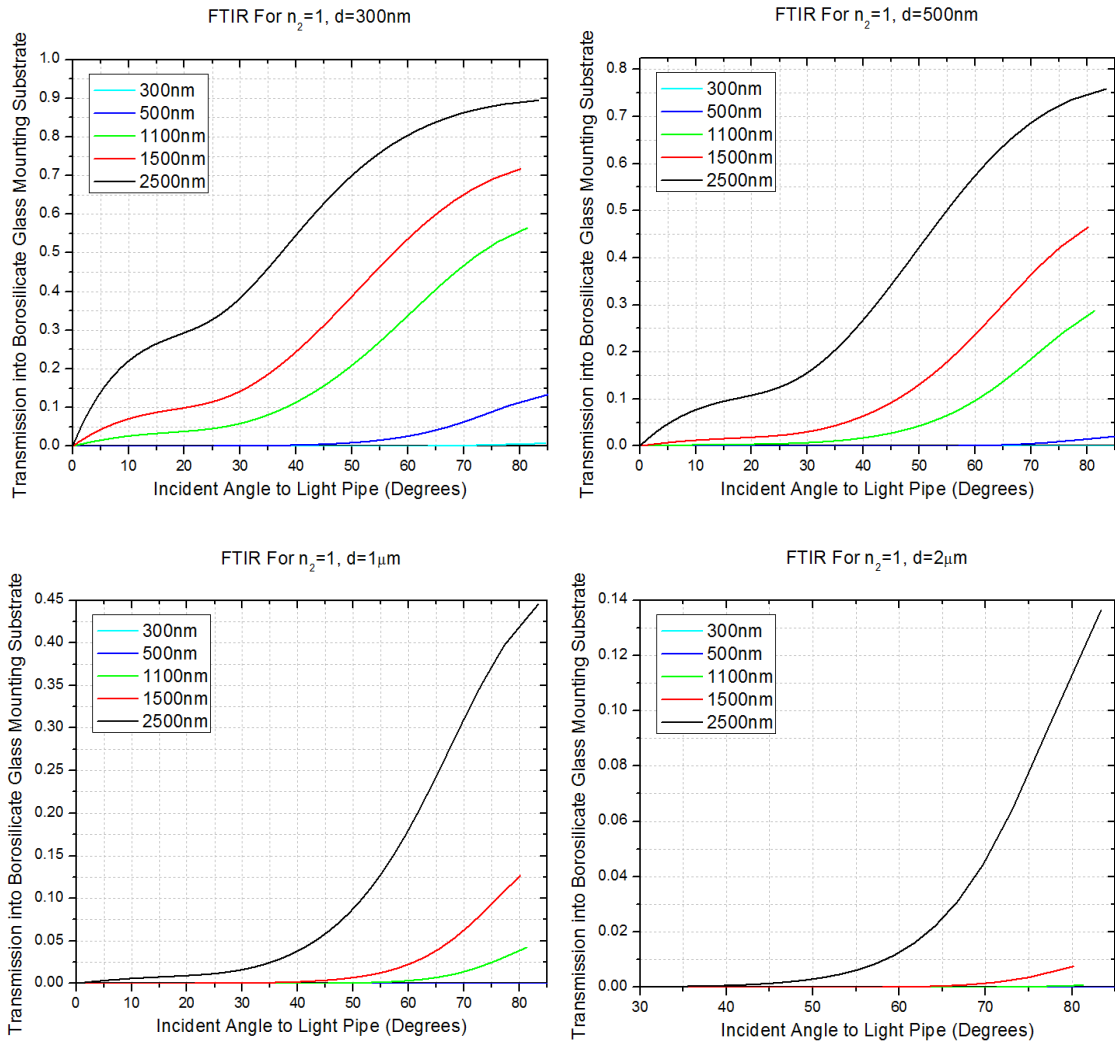


Figure 13 FTIR into a mounting substrate when $n_2 = 1$. The calculated lines end at approximately the corresponding critical angle between n_1/n_2 .

As one might expect, the wavelengths of light that are on the order of, and simultaneously greater than, the thickness of the n_2 medium are found to transmit significantly into the n_3 medium. This thickness dependence can be used to tailor LPs for the purpose of optical filtering. One can see from the 500 nm plots in quadrants three and four of **Figure 12** (i.e. the $d = 300$ nm and $d = 1 \mu\text{m}$ plots), for example, that

the transmission goes from near 0% to 15% at 30° with a 700 nm thickness difference. Various cladding combinations, such as a position-dependent adhesive thickness, could be implemented for optical filtering purposes.

Goos-Hänchen Shift

While it is predicted to be of negligible importance to the results in this work given the relatively short wavelengths under study, such a treatment on loss mechanisms pertaining to LPs would not be complete without mentioning the Goos-Hänchen shift. The Goos-Hänchen shift, as it pertains to this work, is illustrated in **Figure 14**, and pertains to the displacement of a ray reflecting from a boundary upon “reentry” into the guiding medium along the direction of propagation. The effect comprises more than just a shift in position (in more than more direction), and can refer to rotational aspects of the energy in question. A thorough overview of the subject is referenced for the interested reader [24]. From [23], a prediction of the displacement of a ray incident at approximately the critical angle can be found through

$$s = \frac{\lambda}{\pi n_1} \frac{\tan(\theta_{critical})}{(\sin^2(\theta) - \sin^2(\theta_{critical}))^{1/2}}, \quad (1.30)$$

where λ is the wavelength of light, n_1 is the medium of higher refractive index and also the medium the light is undergoing TIR in, θ is the incident angle on the interface with respect to surface normal, and $\theta_{critical}$ is the critical angle of the interface. For $\lambda = 514$ nm light with $n_1 = 1.4616$ and $n_2 = 1.327$, this shift is calculated to be on the order of

microns, or a couple of tens of microns, for an incident angle a degree away, or for an incident angle a tenth of a degree away, from the critical angle, respectively.

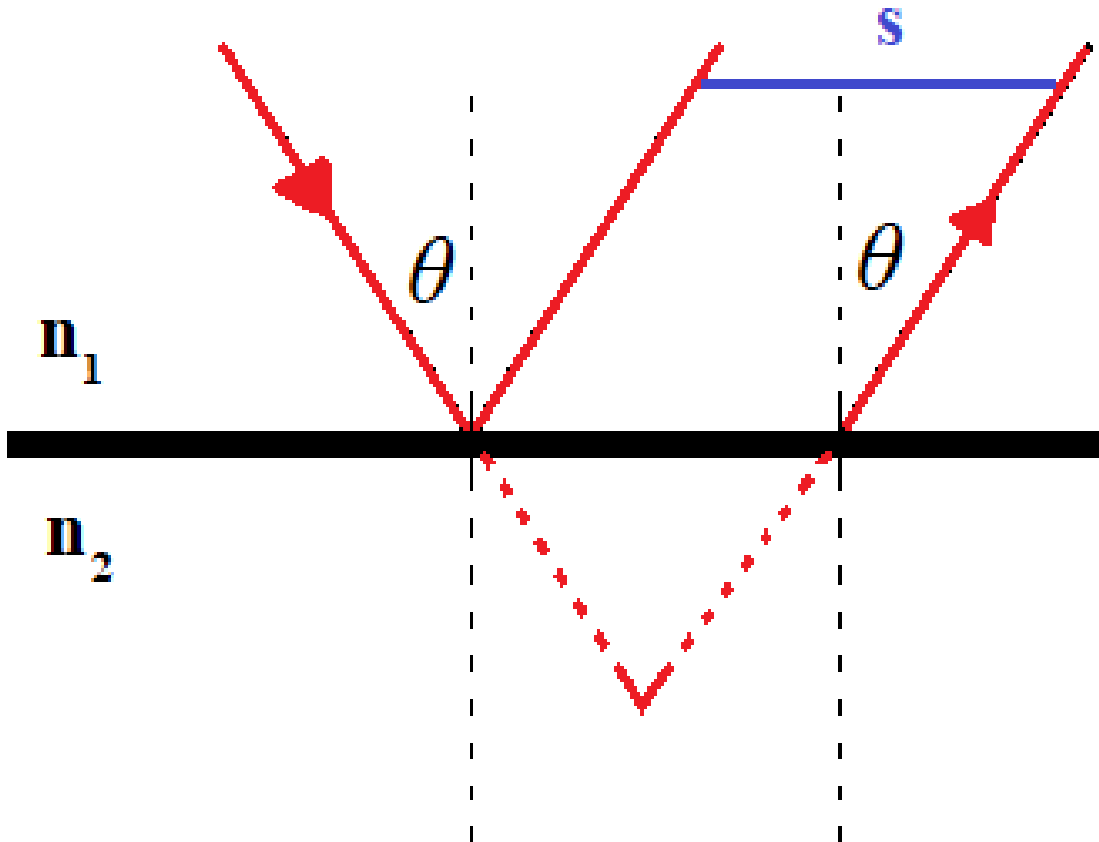


Figure 14 Illustration of the Goos-Hänchen shift. Rather than reflect from the point of reflection, the ray reflects from a location shifted by a distance s corresponding to the apparent emergence point from reflection within the second medium.

CHAPTER II

OPTICAL PATH ELEMENTS

2.1 Sources

Spectral Irradiance

For narrowband studies, three main sources were used throughout this work. They consisted of two laser diode modules from Thorlabs (the 1.2mW CPS635R red laser and the 4.5mW CPS520 green laser), and a NKT SuperK compact supercontinuum broadband source ($> 110\text{mW}$ throughout spectrum with $> 25\text{mW}$ in the visible region) used in conjunction with an Oriel monochromator. A sample spectral profile of the CPS520 source was measured with an optical spectrum analyzer (Thorlabs OSA 201) and shown in **Figure 15**. Most narrowband studies involving the supercontinuum source utilized a 514 nm center wavelength, with an example spectral output shown in **Figure 16**. The wavelength spread was adjusted by changing the input and output slits of the monochromator.

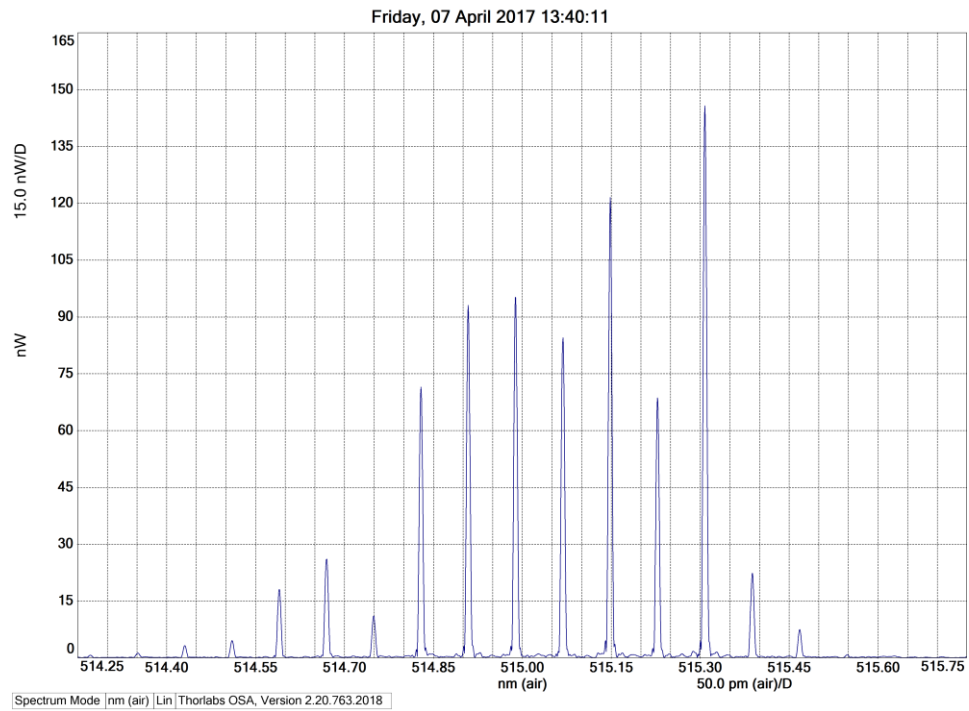


Figure 15 Sample spectral profile of the CPS520 source as measured with a Thorlabs OSA 201 optical spectrum analyzer.

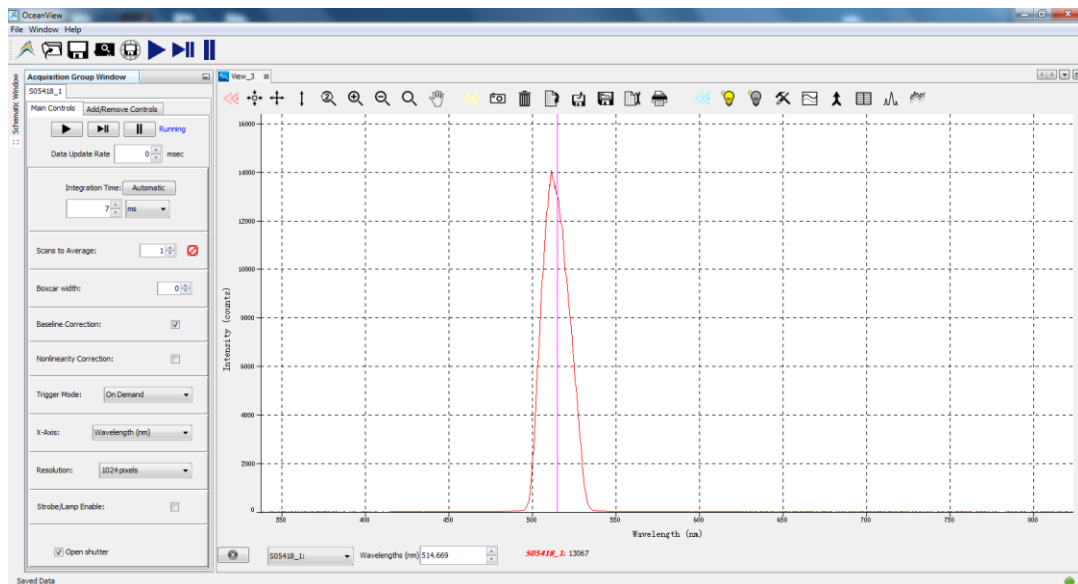


Figure 16 Example spectral output of monochromator delivery system used for testing. It should be noted that the profile depended on the coupling and alignment with the sampling spectrometer's input fiber.

Étendue

As the applications of the LPs considered in this work are those pertaining to solar concentrating systems, it is necessary to underscore the importance of the consideration of the angular distribution of light from input to output of the LPs. Furthermore, as LPs are often used in conjunction with highly divergent light sources, such as for homogenizing and guiding the output of a light emitting diode (LED), it is a pertinent quantity to address. A full treatment of the subject will not be presented here, and the reader is directed to [21] as it is an excellent resource on the matter from the perspective of concentrating systems, with treatments in the context of geometrical optics (including Lagrangian and Hamiltonian optics) and phase space. In essence, étendue is a description of the light receiving, or light emitting, ability of a given optic or optical system. It combines the angular space and surface area of light transmission. An important property of étendue is that it is a conserved quantity, which is why it is a useful quantity to reference when discussing the energy transport of a given optical system. This conservation can be stated as follows,

$$dU_{input} = dU_{output} \quad (2.1)$$

$$dA_{input} \cos(\theta_{input}) d\Omega_{input} = dA_{output} \cos(\theta_{output}) d\Omega_{output} \quad (2.2)$$

Where dA is the surface area of the receiver or emitter, $\cos(\theta)$ is the angle of incidence of the axis of the cone of rays with respect to the input/output surface normal, and $d\Omega$ is the solid angle that makes up the input or output ray cone. For a two dimensional application, this means that the product of the surface area times the angular spread of light at an input end must be the same as the product of the similar quantities at the

output end. Therefore, light of a given angular distribution incident on a tapered LP, whereby the input might be 1 mm^2 but the output might be $.1 \text{ mm}^2$ (as is the case for concentrating LPs), would be predicted to have ten times the angular spread at the output, assuming there are no violations of the acceptance angles on either end. It is for this reason that the angular studies performed in this work provide valuable feedback in concentrating LP design. The reader is directed to [29] for background pertaining to the use of étendue and other parameters in the context of optical coupling in systems utilizing a spectrometer, for example.

Spatial Coherence

The spatial coherence of a given source is ideally limited, so as to avoid unwanted interference effects within a LP, which could subsequently lead to loss being erroneously attributed to a LP's intrinsic transmission properties.

Numerical Aperture

As discussed in §1.1, the numerical aperture of a light guiding fiber or LP is a function of the core and cladding refractive indices. This presents a unique situation for the LPs investigated in this work as their cladding is not the same for every surface. While further analysis is necessary, the worst-case-scenario acceptance angle (or rather, the most pessimistic acceptance angle) is assumed to be that which is dictated by the usual radical expression when used with the cladding index of the highest refractive index.

2.2 Input Coupling

To properly account for light energy as it makes its way through the optical system, element to element coupling must be considered. While various coupling schemes exist in the setup, a standard approach for optical fiber to fiber coupling [13] is reproduced here, prior to specific remarks pertaining to respective coupling situations found within the measurement apparatus specific to this work. The three main types of mechanical misalignment between two optical fibers are illustrated in **Figure 17**, and are longitudinal misalignment, lateral misalignment, and angular misalignment.

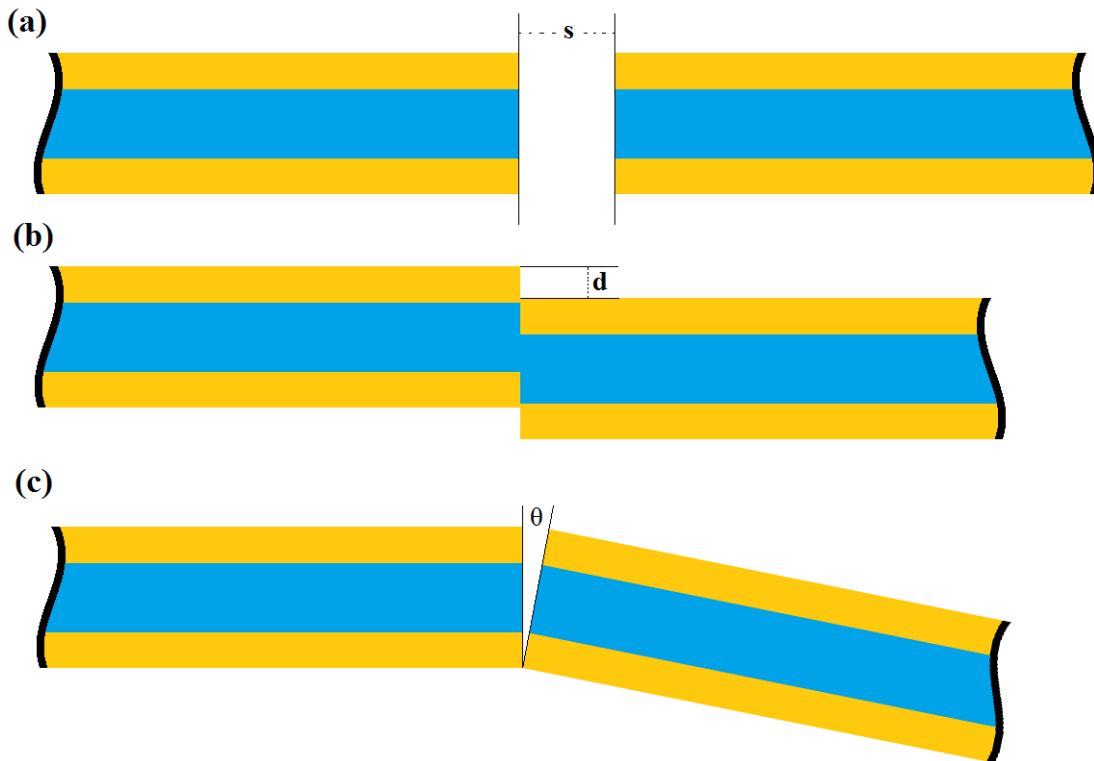


Figure 17 Mechanical misalignment situations between two optical fibers that show (a) longitudinal misalignment, (b) lateral misalignment, and (c) angular misalignment.

Longitudinal misalignment occurs when the fibers are coaxial, but their ends are separated by a distance s . This type of misalignment is sometimes referred to as end separation. Lateral misalignment refers to when the two fibers have a separation distance of zero, their core axes are parallel, but their axes are no longer coaxial and are displaced from one another by a distance d . This situation is also referred to as axial misalignment. For step-index fibers (those having a radially independent refractive index in their core area, as well as in their cladding area), the power coupling is related to the shared area, and the subsequent numerical aperture overlap. For such a step-index to step-index fiber situation, the coupling efficiency is

$$\eta_{step-index} = \frac{\text{Common Area}}{\pi a^2} = \frac{2}{\pi} \cos^{-1}\left(\frac{d}{2a}\right) - \frac{d}{\pi a} \left[1 - \left(\frac{d}{2a}\right)^2\right]^{1/2}. \quad (2.3)$$

Angular misalignment is the situation where the fiber are separated by an angle θ , and for the purposes of the following development it will be assumed that a corner of one fiber end is in contact with the corner of another fiber end. The loss (in dB) of such a misalignment is given as

$$Loss = -10 \log \left(\cos(\theta) \left\{ \begin{array}{l} \left[\frac{1}{2} - \frac{1}{\pi} p(1-p^2)^{1/2} - \frac{1}{\pi} \sin^{-1}(p) \right. \\ \left. - q \left[\frac{1}{\pi} y(1-y^2)^{1/2} + \frac{1}{\pi} \sin^{-1}(y) + \frac{1}{2} \right] \right] \right\} \right), \quad (2.4)$$

where,

$$p = \frac{\cos(\theta_c)(1 - \cos(\theta))}{\sin(\theta_c)\sin(\theta)}, \quad (2.5)$$

$$q = \frac{\cos^3(\theta_c)}{(\cos^2(\theta_c) - \sin^2(\theta))^{3/2}}, \quad (2.6)$$

and

$$y = \frac{\cos^2(\theta_c)(1 - \cos(\theta)) - \sin^2(\theta)}{\sin(\theta_c)\sin(\theta)\cos(\theta_c)}. \quad (2.7)$$

In the above three equations, θ_c refers to the angle the ray distribution from the emitting fiber makes with an imaginary line drawn from the fibers core edge, and θ refers to the angular separation angle.

Lens Array Element

A lens array was designed and developed by the group for use with the solar concentrating module and, with a focal length of 20.3 mm and an inscribed circle diameter of 10.74 mm, provides an angular spread, when measured in two dimensions, of $\sim 14.8^\circ$. Depending on the characteristics of the source it is used in conjunction with, the power distribution will not necessarily be uniform at the lens' output.

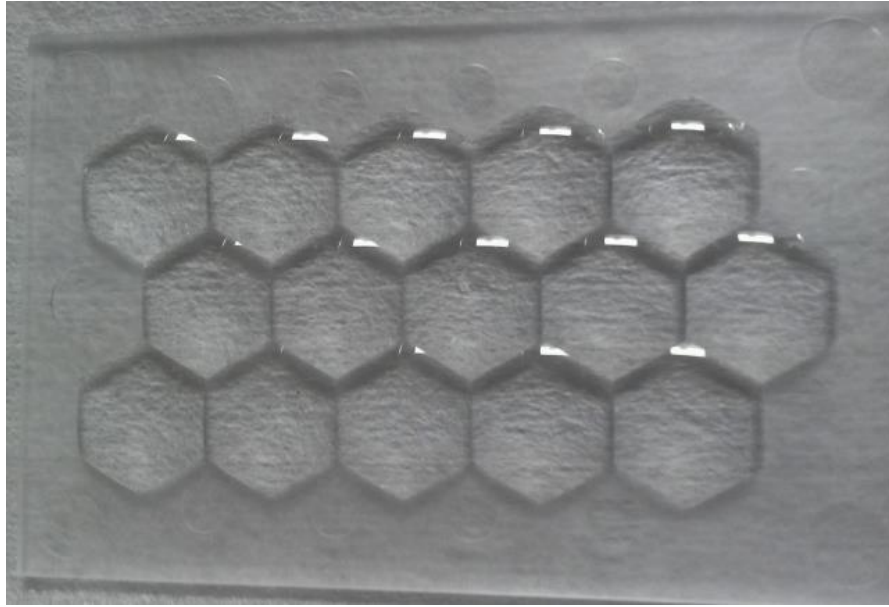


Figure 18 Polymer aspheric lens array made by Syntec Optics. One side of a hexagon is 6.2 mm in length, and the focal length of an individual lens element is 20.3 mm.

A singular lens element is characterized by scanning a narrow beam along a line that extends from one corner of a hexagonal lens to its opposing corner. In this way, a radially-dependent transmission function can be determined for a given lens element. This information is then compared to a transmission measurement whereby a beam is coaxial with the lens and is as wide as the setup allows. If testing near clear aperture (i.e. illuminating the lens input over near its entire surface area), care must be taken to ensure that the beam size is both not larger than a circle inscribed within the hexagon and not larger than the reference detector, in order to avoid clipping.

Ray Fan Producing Optics

A fan of rays can be produced through the use of various optics. Two such optics appropriate to this function are described below.

Cylindrical Lens

Cylindrical lenses take light at the input, and focus the beam along a singular axis. Two cylindrical lenses selected appropriately and oriented 90° with respect to each other can be used to create a rectangular spatial profile. Cylindrical lenses are common, and relatively inexpensive. One should note that, when using a cylindrical lens with a beam of a Gaussian profile, the beam profile at the output of the lens will have a non-uniform distribution with the center of the output having the greatest intensity, and the far sides having the least intensity.

Powell Lens

Powell lenses, also referred to as a type of laser-line lens, surmount the problem of a non-uniform power distribution at the output with its unique geometry. That is to say, that when light having a Gaussian distribution, such as a common laser beam, is incident on the lens, the line produced by the lens has a uniform intensity profile. This is accomplished by the lens' aspheric input which creates sufficient spherical aberration to redistribute the light so that the output of the lens is a line of uniform intensity [22].

2.3 Detector

Acceptance Angle

Through considerations of conservation of étendue, the very nature of LPs used for concentrating applications, such as those investigated in this work, necessitates the ability to capture highly divergent sources where, in this context, the source refers to the output of a LP. Full characterization of a light pipe should include a determination of angular acceptance, and the need for measuring large exit angles or, stated in a related way, measuring highly divergent sources, is a given. Integrating spheres have long been the go-to choice for such applications as they offer the intrinsic ability to capture light of poor collimation. This subject will be examined in detail in § 4.1.

Wavelength Dependence

A given detector's effective response is wavelength dependent. A given detector has an intrinsic electronic wavelength dependent response, usually described in terms of Amps/nm (this is referred to as its responsivity) as well as a structural wavelength dependent response due to its wavelength dependent reflection properties.

Detection Area Homogeneity and Relationship to Illumination Area

Photodiode-based detectors can suffer from inhomogeneities near their edges and, as such, the edge areas of detectors are often not recommended to be illuminated due to time-domain issues associated with unwanted capacitance and resistance [15].

Power Meter and Data Collection

Multiple data collection schemes were used and developed during the course of this work. The uncertainty associated with a given measurement as it pertains to data collection (as opposed to other factors) is touched upon in §6.3 and, depending on the measurement methodology can sometimes be on the order of 1% - 5% for a given data point. The power meter used for all measurements in this work (Thorlabs PM320E) is made by the same company that makes the detectors, and allows for easy interfacing between the two. The meter comprises two input channels (one for the reference arm detector and one for the detector reading an LP's output), and can provide a real-time analog voltage output that represents the ratio between the powers read by whatever two detectors are connected to it. The first data collection method discussed here utilizes the analog output of the meter. This analog voltage signal is fed to an Arduino microcontroller that is programmed to record 1000 voltage readings upon a button press and report the data to an open source Microsoft Excel macro code (PLX-DAQ). For a given data point, the sampling takes about 11 seconds to complete. Since the Arduino can only handle 0-5 VDC, the power meter's signal output is adjusted through the meter's output voltage offset setting in order to make sure that voltages corresponding to ~30%-100% in transmission fall within a 0-5 VDC output. The individual voltages that are recorded are corrected for this offset, and converted from dB to a percentage, for more instinctive transmission evaluation. This data collection scheme allows for real-time transmission measurements by comparing the signal from a LP's output to that of the signal from the reference arm. The main advantage of this is that this method is far

less sensitive to the stability of the source, as it is a comparison between signals that should fluctuate simultaneously with source fluctuations. Of course, the insensitivity holds only as long as the refresh rate of the two-channel readout is much faster than the rate of fluctuation of the source. While the Arduino/Excel system performs well, it sometimes suffers from an erroneous value during the macro writing process and is most likely an issue pertaining to memory limitations with the Arduino and computer running Excel. While such errors are noticed immediately by the user, and subsequently corrected for, its unpredictable nature make automation of data collection using this method, more involved. To alleviate this issue while still utilizing the analog output of the meter, a more long-term data collection solution would ideally consist of a dedicated PC-interfaced digital bench voltmeter.

The second method of data collection utilizes the meter's native data logging ability to a computer. A basic python script was developed by David Dolt and Sandheep Kumar to quickly read the log and return an average ratio with associated standard deviation for a given measurement. This method avoids the complexity introduced in the multiple correction factors and connections present in the first method, as is the method by which data is collected at the time of this document's preparation.

While the power meter interfaces with detectors easily, the user must specify the wavelength of detection, as each detector has a different response function in the form of (unit current)/(unit wavelength). The very fact that the response of a given detector

varies as a function of wavelength, precludes the ability to measure a broadband source easily. It is for this reason that spectrographic or other means are necessary for broadband transmission measurements of a LP or other optical conduit.

2.4 Reference Path

The reference path of the apparatus is shown in **Figure 19**. Light incident on a non-polarizing cube beam splitter (NPCBS) splits into a beam that continues along the original trajectory of the incident beam and one that travels on an orthogonal trajectory. The latter of the two beams is incident on a reference detector, which in turn reflects off of the detection surface and into a fiber collimator (after again passing through the NPCBS), where the light is guided to a spectrometer. This reference arm serves the purpose of sampling the power of the light after being split, and also the purpose of determining the spectral composition of the light used for the study while simultaneously allowing for a way to confirm the setting of the monochromator or other wavelength selection device used to filter the broadband source. Since the power readings of both primary beams exiting the NPCBS are not exactly equal (and vary based on wavelength), data collected when a LP is in the test arm is determined though the quotient of the ratios of the test arm power to the reference arm power with and without an LP in place as shown by the following equation

$$Power_{Transmitted} = \frac{Power_{Test Arm With Sample} / Power_{Reference Arm}}{Power_{Test Arm Without Sample} / Power_{Reference Arm}} \quad (2.8)$$

To isolate the measurement from the stability (or rather, the instability) of a given source, the power in the test arm with and without a LP in place cannot be compared directly. This is why ratios are compared. Also, the NPCBS does not split the incident light exactly 50/50, and the ratio of the exiting beam powers is dependent upon the wavelength. In addition, this scheme allows for the use of non-matched detectors in either arm of the split. For these reasons, it is necessary to utilize a reference arm for real-time data collection.

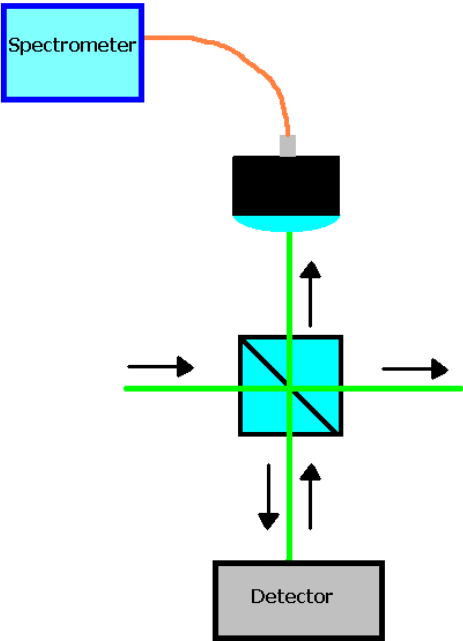


Figure 19 Reference path of measurement apparatus.

2.5 Spectral Filtering

When a broadband source is used as the starting point for a narrowband source, it is necessary to isolate the wavelength/wavelengths of interest. This is commonly accomplished through various means. In the case of the setup used in this work, a monochromator is used. Alternatively, other means could be employed to provide filtering, such as thin film interference filters (often available as long-pass, short-pass, band-pass, or notch filters), bulk volume absorption filters, or more exotic routes such as by using the phenomenon of electromagnetically-induced transparency (EIT).

Monochromator

Monochromators accomplish their filtering through the use of dispersive optics such as a prism or diffraction grating. Various geometries/types exist that provide different trade-offs (e.g. Czerny-Turner, Fastie-Ebert, holographic, etc.). Care should be taken that, in the case of a monochromator utilizing a diffraction grating, other orders of different wavelengths are not present in the output. This necessitates the need to characterize the exit light using a spectrometer, or similar device.

Ocean Optics Spectrometer

The spectrometer used to sample the reference beam was an Ocean Optics STS-VIS miniature visible light spectrometer sufficiently sensitive to ~450 nm – 850 nm light. Its spectral resolution is advertised to be 1.5 nm, and utilizes a SMA fiber input connection that has an approximate numerical aperture of .125.

Optical Spectrum Analyzer

A more accurate and precise spectral analysis device is that of an optical spectrum analyzer. Such an instrument provides significantly higher spectral resolution than a portable spectrometer and reports an absolute power instead of arbitrary intensity counts.

2.6 Calculating the Estimated Transmission

The throughput of an LP is the ratio of the amount of light exiting a LP to the light that entered the LP. A measurement, or prediction thereof, of this must take many factors into consideration. Ultimately, the measured power can be described by the following which includes the major contributors to a throughput measurement

$$P_{Measured} = P_{Source} \eta_{Input} \eta_{Detector} \eta(\lambda, \theta)_{Conversion} \prod_i^n (1 - i) \quad (2.9)$$

where P_{Source} is the power of the light before the LP; η_{Input} is the coupling efficiency at the input of the LP and is treated by comparing the angular distribution of the incident light to the acceptance angle of the LP; $\eta_{Detector}$ is the coupling efficiency into the detector; $\eta_{Conversion}$ is the wavelength and angle-dependent efficiency of the detector to detect and convert the coupled light energy into a power; and the product term represents the various loss mechanisms described in §1.2 which include the wavelength and angle-dependent reflection at the LP input described by the Fresnel reflection equations given, the wavelength and path length dependent bulk attenuation/absorption coefficient of the LP material, the wavelength and path length dependent bulk attenuation/absorption coefficient of the LP material, the wavelength and angle-dependent reflection at a

cladding interface (keeping in mind that there are different cladding materials at different interfaces), and the wavelength and angle-dependent reflection at the LP output whose incident angular distribution might differ from the distribution upon launching due to form and surface imperfections. In physical samples, non-zero surface roughness on all sides of the LP causes a deviation in predicted behavior that can only be completely defined if the entire surface profile of the LP is known, in conjunction with complete knowledge of the angular, spatial, and power distributions of the incident light.

CHAPTER III

GLASS LPS FOR OPTICAL TESTING

The LPs used in this work were fabricated and profiled on-site by Yusuf Dogan through a femtosecond laser irradiated assisted chemical etching (FLICE) process [30] whereby a structure is written in a substrate (fused silica in this case) and liberated from the substrate through chemical etching. As such, the laser irradiated sidewalls of a given structure require polishing in order to be of optical quality. Examples of the endface quality prior to polishing are shown in **Figure 20**. The reported roughness values of the original substrate surfaces, the after-etched surfaces with and without a 80 μm Gaussian filter, and the polished surfaces after filtering at LP sidewalls were 6.4 nm over a .69 mm x .76 mm area, 490 nm with filtering and 830 nm without, and 6.36 nm over a .5 mm x 2.65 mm area, respectively. Multiple routes to achieve a high quality optical surface on the liberated surfaces have been used and are in various stages of process development and include, but are not limited to, CO₂ laser polishing, surface treatments of optical adhesive with a known refractive index, and the attachment of an optical window using index-matched liquids and/or adhesives. Each method introduces a form deviation of some kind and, until such processes are refined further, makes for imperfect LPs for characterization. Similar statements can be made regarding the FLICE and liberation processes.

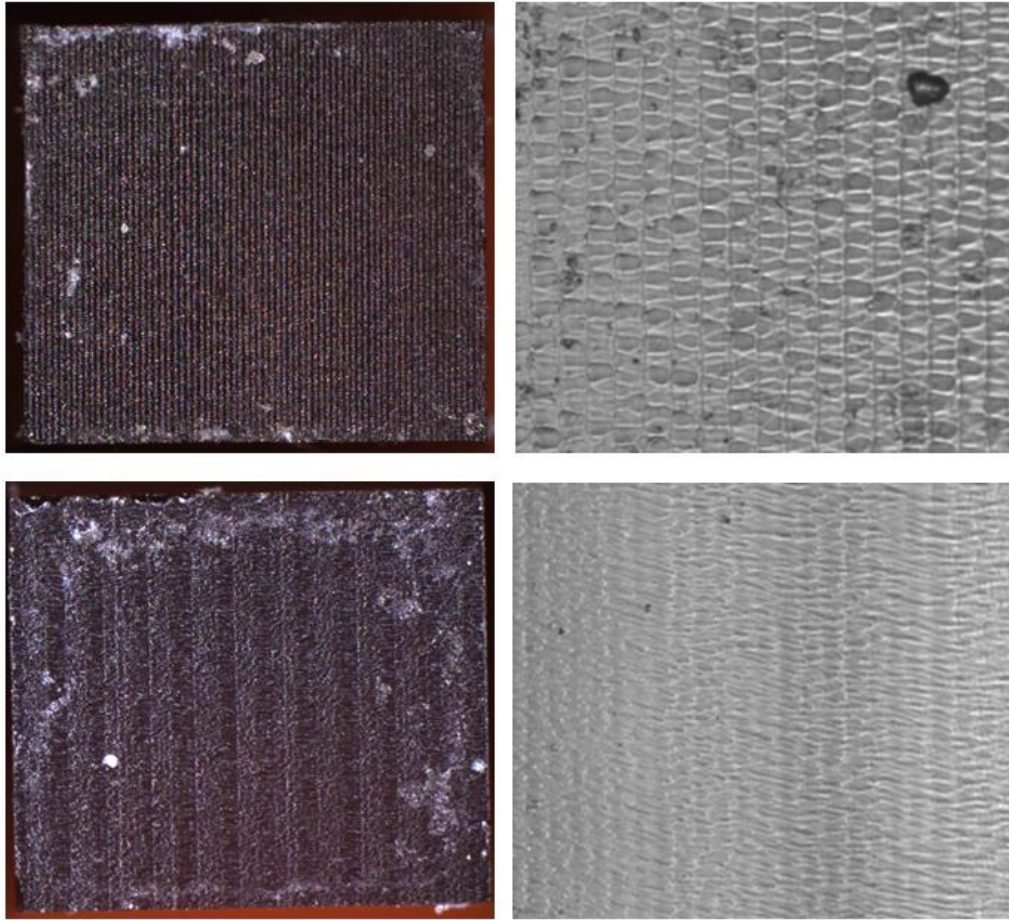


Figure 20 LP endface quality before polishing processes. The top and bottom rows show samples created using different fabrication parameters and display a 1 mm² endface. The right column shows a zoomed in view of a selected region of a respective sample.

3.1 Light Pipe Assembly

The light pipes used in this work were fused silica lengths having a square millimeter cross section. Multiple mounting schemes were tested but almost always included the use of ultraviolet-cured optical adhesives of known refractive index. In order to achieve a good level of control over the attachment process, a microscope stage was modified to

hold a vacuum pickup tool, or other implement, as shown in **Figure 21**. This modified microscope stage offers precise three-axis translational ability, as well as tip/tilt ability to its stage.

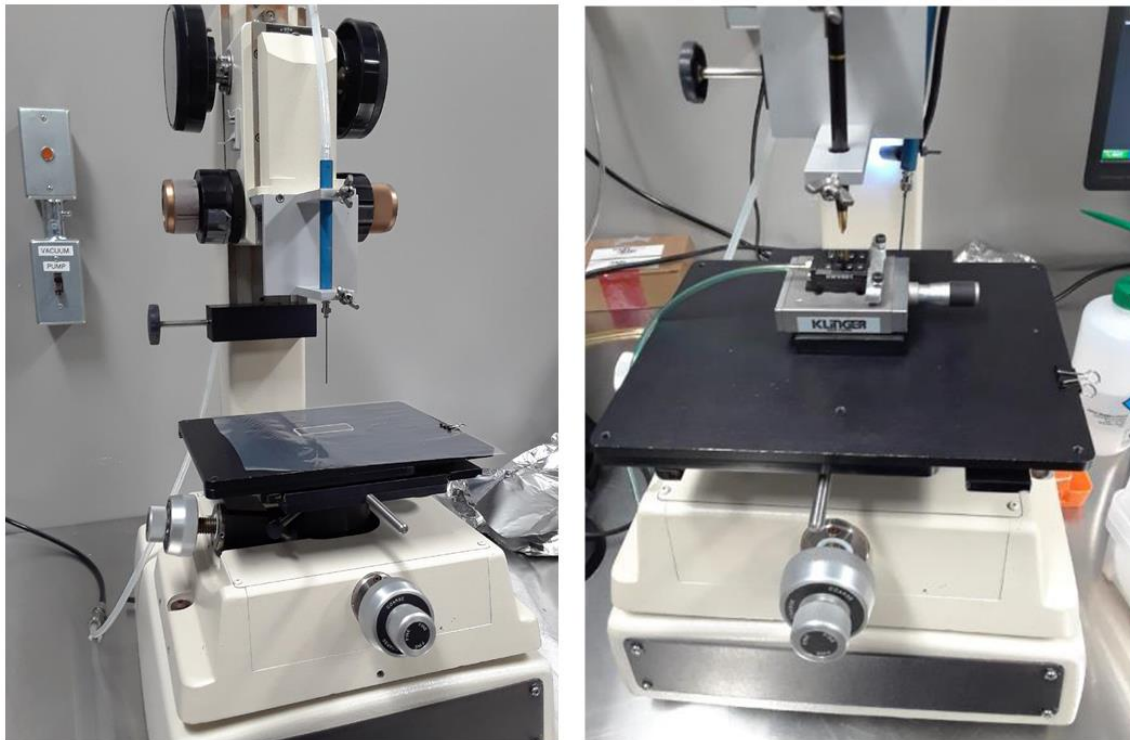






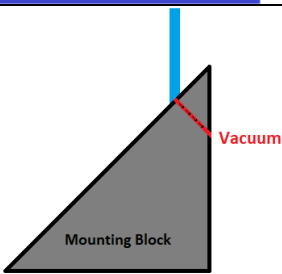
Figure 21 LP assembly stage shown with a vacuum pickup tool in place (left) and with a diamond scribe pen and translation stage-mounted vacuum chuck (right).

Mounting Schemes

Testing a given LP requires mounting it, in some fashion, to either a substrate, a testing fixture of some kind, or to a combination of both. As physical contact with a given LP defines the cladding parameters at the contact locations, mounting has been accomplished through the use of materials possessing a fairly well known optical

refractive index. These materials have almost always been optical adhesives from Norland Products, Inc., and are the subject of the next section. Throughout the course of this ongoing work, multiple mounting arrangements have been tested and are summarized in **Table 1**. In general, mounting schemes consist of a LP's base being in > 85% contact with optical adhesive, or in partial contact only at select locations (and otherwise in contact with atmosphere) where, at those locations, adhesive is applied to a glass support which will be referred to as a crossbar, and might possess a high reflection coating applied in-house consisting of 150 nm layers of silver and silicon dioxide. Original majority contact mounting schemes were > 95% contact with adhesive, but an ~5 mm overhang on the output side was determined to be desirable in order to provide the ability to translate the end of a given sample into the integrating sphere detector that was used to measure the output power of the sample.

Table 1 Selected mounting arrangements for LP testing.

A	B	C
1	Mounting Arrangement Description	Graphical Representation
2	Rectangular Prism Light Pipes	
3	LP base in full contact with adhesive joining to borosilicate glass microscope slide mounting substrate	
4	Cross Bar Supports	
5	Light Pipe With Singular 45° Turning Surface	
6	LP base in full contact with borosilicate glass microscope slide mounting substrate.	
7	Cross bar support	
8	Vacuum held by turning surface	

Representations of a LP mounted in majority contact are shown in **Figure 22** and **Figure 23**. Images of LPs mounted on crossbar supports are shown in **Figure 24** and **Figure 25**.

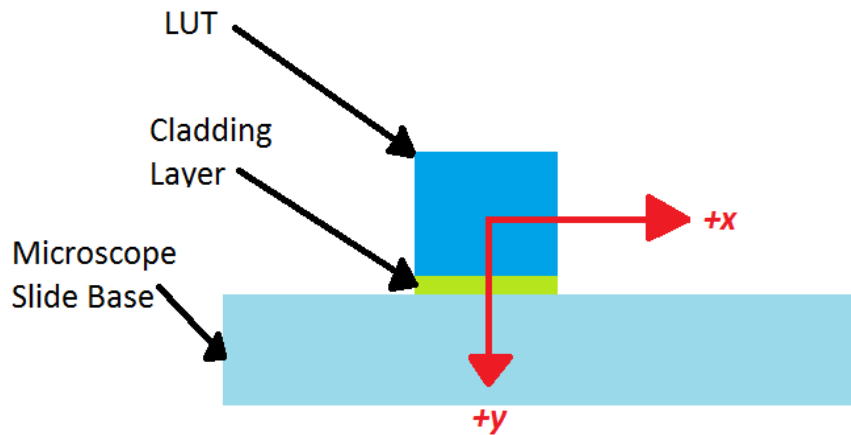


Figure 22 End-on view of a rectangular prism LP mounted in majority contact with a substrate. It should be noted that, for a given LP, one set of parallel sidewalls as well as both endfaces, will be polished post FLICE process and the remaining parallel sidewalls will possess very nearly the original substrate surface properties.

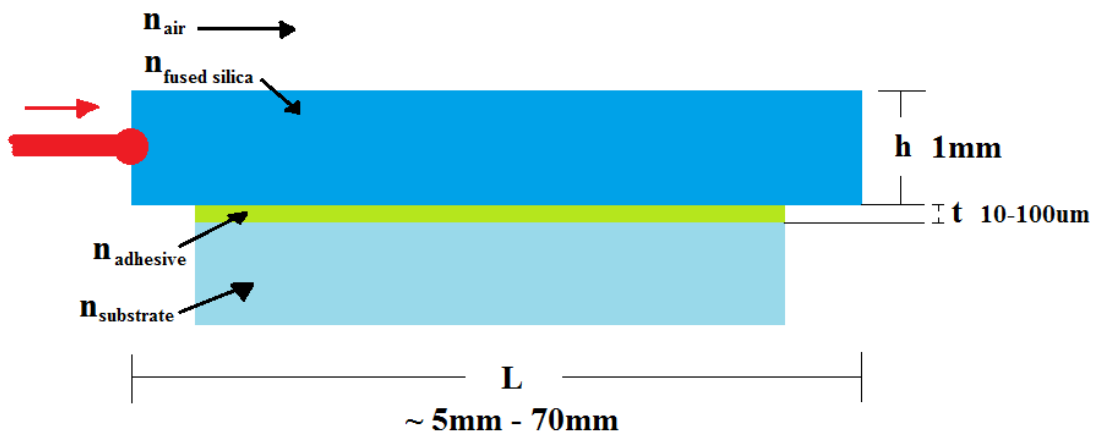


Figure 23 Side view of a rectangular prism LP mounted in majority contact with a substrate.

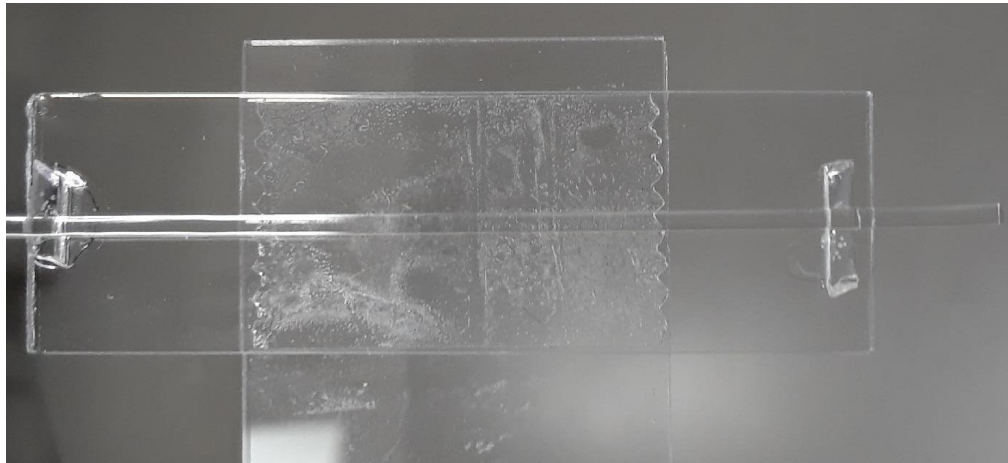


Figure 24 Rectangular prism LP mounted on two crossbars. The cross bars are mounted on a borosilicate base, which is subsequently mounted, via double sided tape, to a bottom microscope slide for holding purposes.



Figure 25 LP with 45° face mounted on high reflection coated crossbar and utilizing a microscope slide cover slip at its output.

Adhesive is either applied to the underside of the LP, and then lowered onto a mounting substrate or, alternatively, adhesive is applied to the mounting substrate and then the LP is lowered onto the adhesive. Both methodologies are depicted in **Figure 26**. One issue that arises from this process is the excess adhesive that finds its way onto the sidewalls of the sample through displacement, evaporation, and capillary forces inherent to a given adhesive. This is depicted in **Figure 27**. A possible way to mitigate this effect, is to

create, perhaps through the use of a wafer dicing saw, a pedestal mounting structure, such as the one depicted in **Figure 28**.

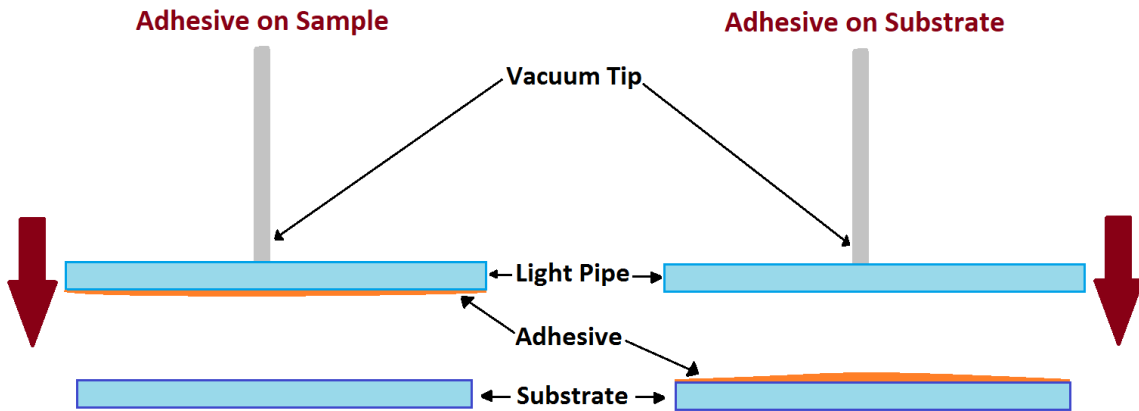


Figure 26 Two different methodologies to adhere a sample directly to a mounting substrate.

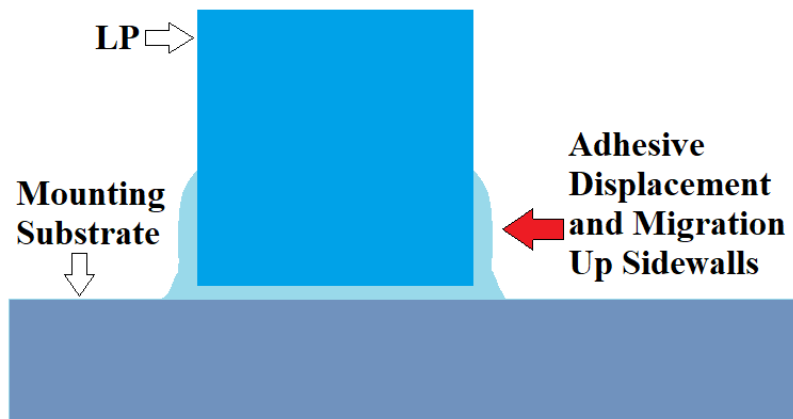


Figure 27 End-on depiction of adhesive displacement and migration along the vertical sidewalls of the LP.

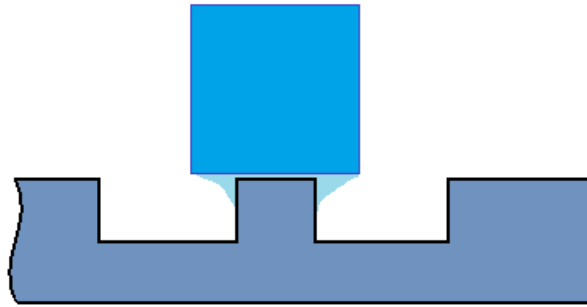


Figure 28 Pedestal mounting structure to mitigate adhesive sidewall creep.

Optical Adhesives

Many optical adhesives were used throughout the course of this work and most of them and their corresponding properties are tabulated in Table 2.

Table 2 Various Norland Products Inc. optical adhesives and associated properties.

Product / Adhesive	Listed Refractive Index	Viscosity (cps)	Shore Hardness
13685	1.3685	15-25	55 (Shore D)
1328	1.328	2000-3000	15, 70 (Shore D, A)
1327	1.327	4500-5500	15, 70 (Shore D, A)
1315	1.315	15	Not Specified
142	1.42	20-40	70 (Shore D)
85	1.46	200	40 (Shore D)
146H	1.46		

End Facet Preparation

To provide optical quality surfaces for transmission testing while the polishing processes are being optimized, it became necessary to investigate alternative routes to optical quality endfaces.

Cover Slips

This method utilizes a borosilicate glass microscope slide cover slip that is scribed/cut using a diamond-tipped scribe pen to produce small $\sim 1.5 \text{ mm}^2$ pieces to adhere, either via index-matched adhesive or index-matched liquid, to the endfaces of a given LP. An example of the concept is shown in **Figure 29**. Images of cover slips attached to a LP are shown in **Figure 30** and **Figure 31**.

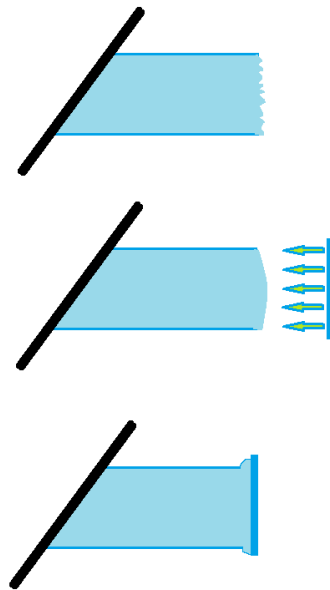


Figure 29 Microscope slide cover slip surface roughness enhancement concept.

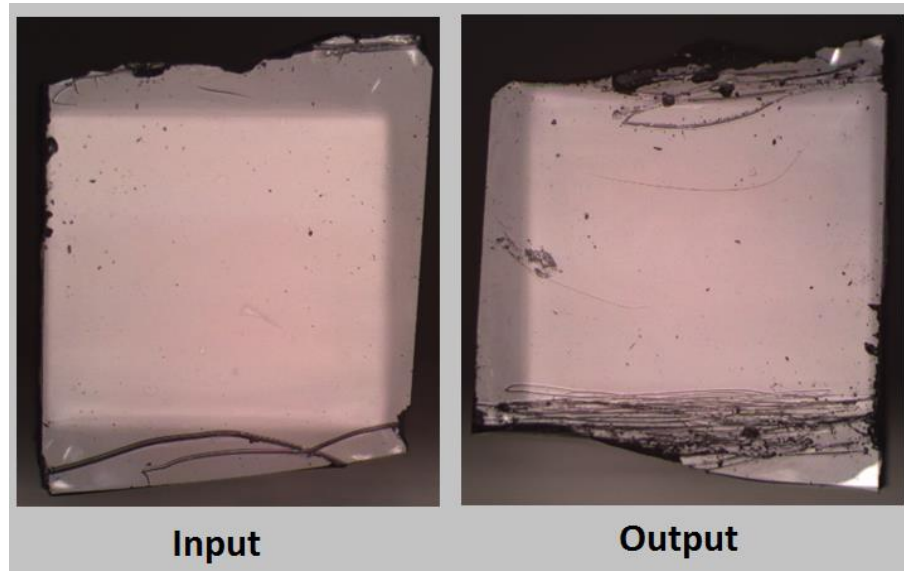


Figure 30 Microscope slide cover slips as an LP endface enhancement – end view.

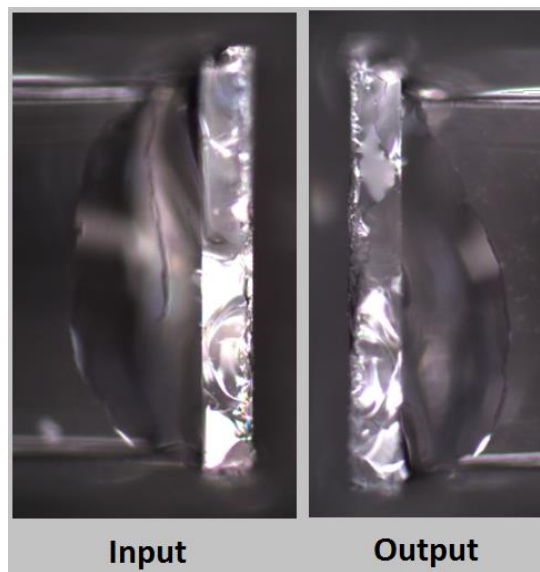


Figure 31 Microscope slide cover slips as an LP endface enhancement - side view.

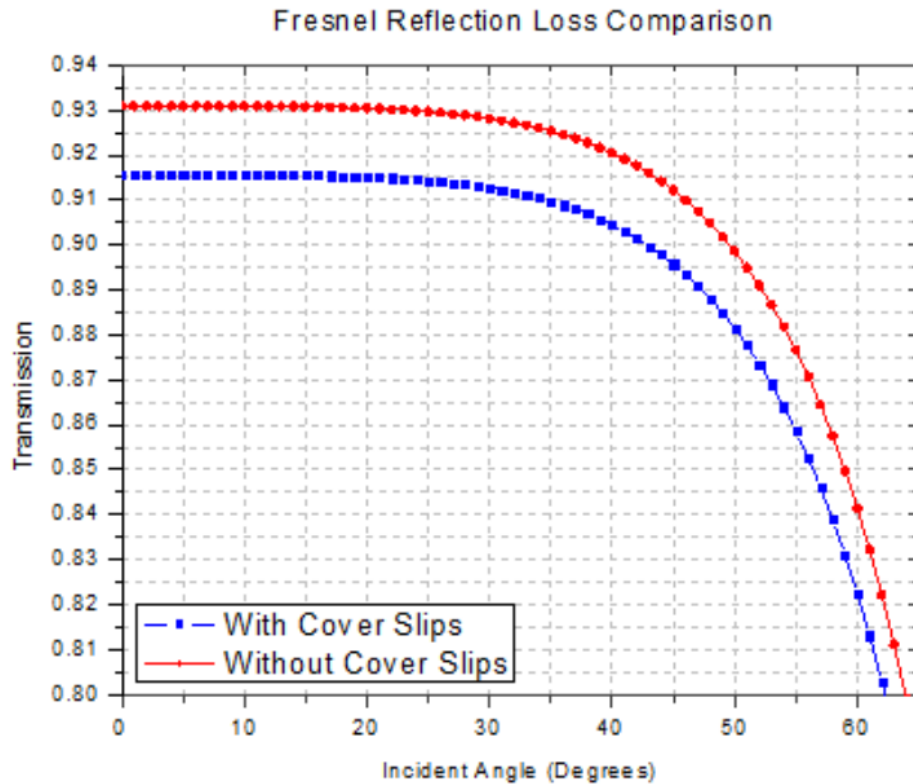


Figure 32 Fresnel reflection loss comparison between microscope cover slips use on LP endfaces. The negligible change in angle due to refraction from the cover slips is considered. Calculations performed for 514 nm light and associated refractive indices. Perfect index matching at interfaces is assumed.

Adhesive Endcaps

An alternative method to produce optical quality endfaces is similar to that described in [19] and is shown in **Figure 33**. This method consists of applying optical adhesive, ideally index matched to the LP material, to the endface of a LP and lowering it onto a form surface, where it would be cured and inherent the shape and roughness of the form surface. With this method, the choice of release agent to apply to the form surface before adhesive contact is critical. Multiple release agents were tested, including

Polytetrafluoroethylene (PTFE)-based and oil-based release agents, but a silicone release agent has proven to offer the best results. A white light interferometry produced surface profile is shown for a surface created in this fashion with a non-ideal release agent in **Figure 34**, as well as with a silicone based released agent in **Figure 35**. One issue observed with the adhesive endcap PTFE-based release agent, was that the release agent appeared to create a seal around its extends, which in turn created a vacuum at the center of the endcap when attempting to pull it away from the form surface, thereby creating a centralized bulge to the adhesive endcap. This was not observed with the use of the silicone-based release agent.

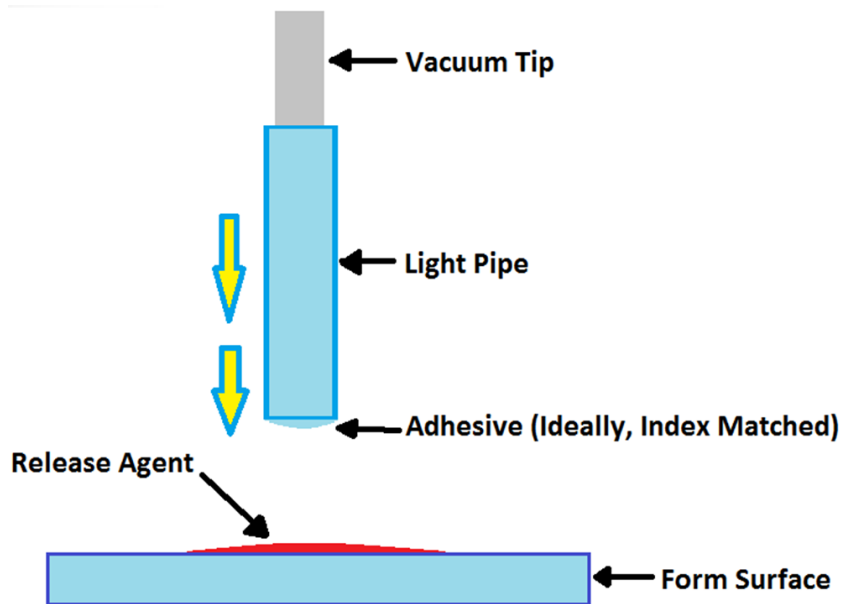


Figure 33 Adhesive-made endface caps production methodology.

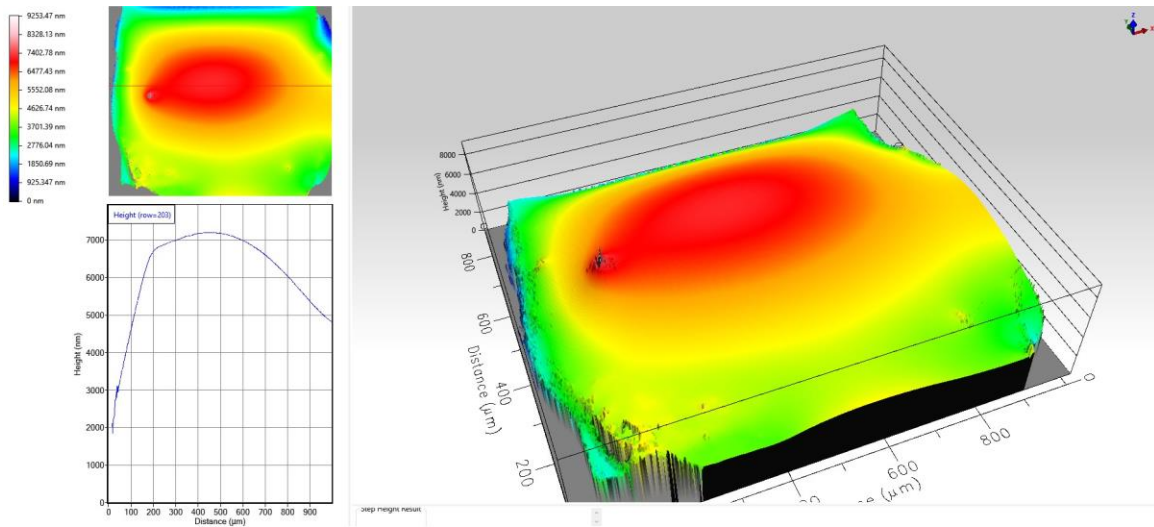


Figure 34 White light interferometer created surface profile of adhesive endcap created with a non-ideal release agent.

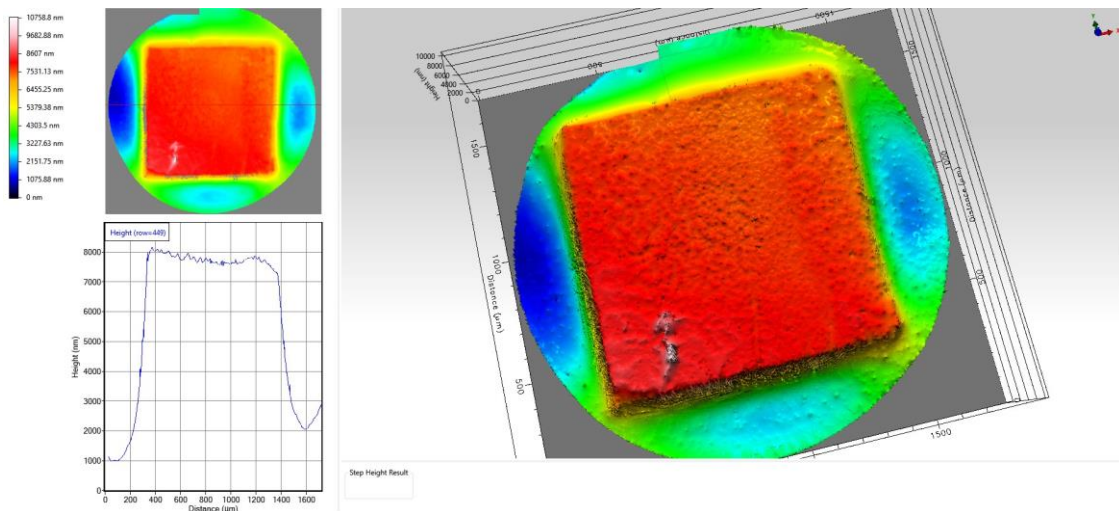


Figure 35 White light interferometry created surface profile of adhesive endcap created using a silicone-based release agent.

One is able to coat two microscope slide cover slips with the silicone release agent and sandwich a couple of drops of optical adhesive to create a sheet of polymer with known refractive index. Such a sheet is shown in **Figure 36**.



Figure 36 Polymer sheet of $n = 1.327$.

High Reflectance Coated Cover Slips and Crossbars

Various borosilicate cover slips as well as borosilicate and fused silica crossbars (square millimeter cross-sectioned lengths) were given a high-reflection coating through the deposition of 150 nm – 350 nm of silicon dioxide on top of 100 nm – 150 nm of silver. These were fabricated by Robert Atkins, Chihying Lee, and Javed Ali on-site.

3.2 Module Assembly

Baseplate Preparation and Subsequent Light Pipe Alignment and Mounting

LP structures are mounted to a glass baseplate. Alignment of the total module is an exercise that involves only the lens array and the baseplate and not the individual LPs.

For this reason, it is imperative to align and attach the LPs to the baseplate precisely, as the LPs will not be able to be moved relative to one another after they are attached to the baseplate. To better accomplish this task, an alignment grid is created on the mounting surface of the baseplate using a CO₂ laser cutter/engraver made by Full Spectrum Laser. A sample alignment grid pattern is shown in **Figure 37** and shows three sets of three long line segments that correspond to the three columns of lenses in the lens array. The intersections of each of the three central line segments with an orthogonal line segment centrally located within a set correspond to the center of a lens element, if a lens element is present at that location. The existence of the line segments between the intersections allows for alignment of a LP using an LP's outer dimensions and helps ensure parallelism among desired directions.

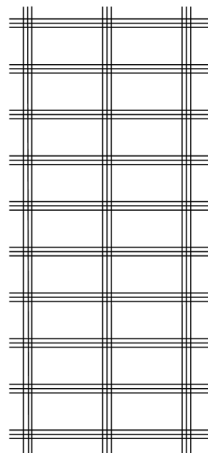


Figure 37 Baseplate alignment grid.

LPs are mounted to either crossbar supports or directly to the baseplate, where optical adhesive is used to create a bond in either case.

Total Module Alignment

A test bench for total module alignment and testing was developed and shown in **Figure 38**. The apparatus accomplishes the ability to translate the lens array in all three Cartesian axes with respect to the bottom plate that the LPs are attached to, as well as provides relative tip/tilt and rotation to the two entities thereby allowing for all degrees of freedom necessary for precision alignment.

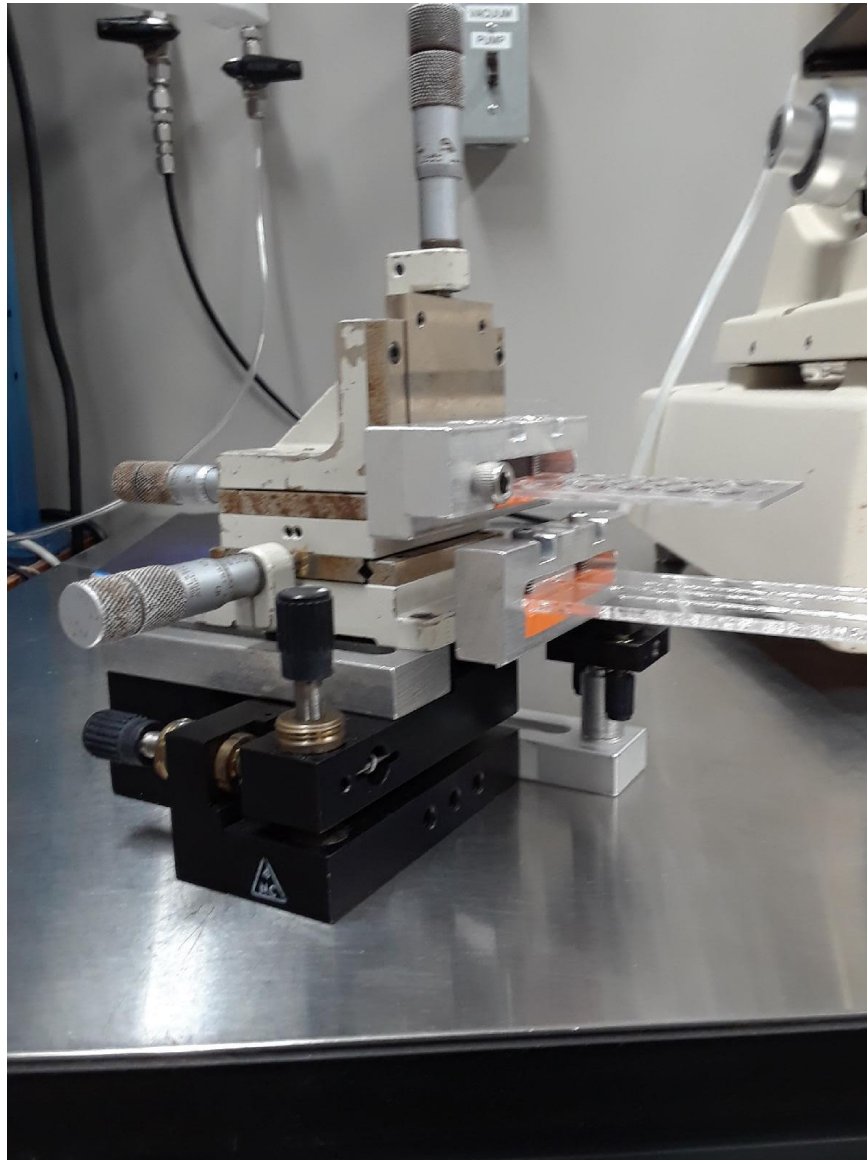


Figure 38 Total module testing apparatus

CHAPTER IV

COLLIMATED BEAM - ANGULAR SWEEP CHARACTERIZATION

4.1 Measurement Setup

Figure 39 shows the measurement apparatus which consists of a supercontinuum or other broadband source paired with a monochromator. The linewidth of the source is controlled through the exit slit on the output of the monochromator. Light is delivered from the monochromator to a non-polarizing cube beam splitter via a multimode fiber free space coupled at both ends to microscope objectives, both having three-axis translational ability, as well as tip/tilt ability. Coupling adjustment allows for control of beam size and divergence. One arm of the beam splitter is directed to a detector and used to determine a reference reading for measurements. The light pipe under test (LUT) is positioned in a motorized rotation mount providing φ control (see Fig. 2), which has three-axis translation ability, as well as tip and tilt control for precise alignment. An integrating sphere (IS) detector is positioned at the output of the LUT and also has three-axis translation ability. An IS detector is chosen over a standard photodiode detector due to its intrinsic ability to accept divergent light, which is expected from the output of concentrating light pipes familiar to solar applications. Both the LUT and the IS can be rotated about a common rotation axis to provide θ adjustment. This constitutes a testing apparatus that allows for wavelength and arbitrary incidence angle and launching location selection.

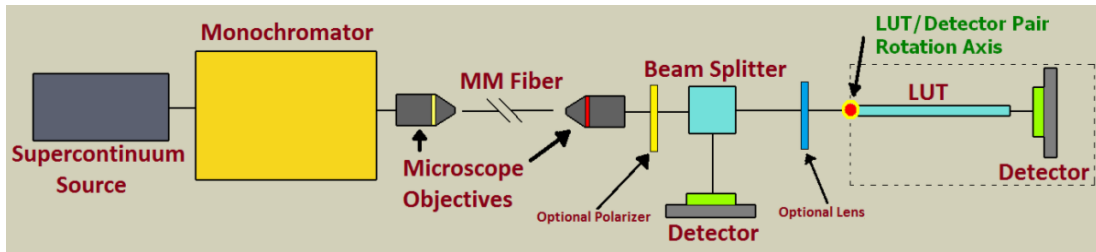


Figure 39 Light pipe optical throughput measurement apparatus.

The reference detector used was a photodiode detector from Thorlabs (S130C), as was the IS (S142C). The supercontinuum source was from NKT (SuperK Compact) and provides $\sim 450 \text{ nm} - 2350 \text{ nm}$ output. The Oriel monochromator used has a wavelength selectivity from $\sim 133 \text{ nm} - 1050 \text{ nm}$ with its current diffraction grating. The initial and final microscope objective lenses carried 10X and 5X magnifications, respectively. The power meter used was also from Thorlabs (PM320E) and interfaced with the detectors easily. The powers of the unobstructed reference and test beams vary due to the stability of the supercontinuum source, the wavelength selected, thermal considerations, and alignment, but are on the order of $250 \mu\text{W}$ and $100 \mu\text{W}$, respectively, for the measurements portrayed utilizing a central wavelength of 514 nm . The linewidth was measured to be 30 nm as determined using an Ocean Optics spectrometer (STS-VIS). This was accomplished by setting up a fiber coupled to a lens opposing the reference arm detector on the other side of the beam splitter, and aligning it to the reflected beam from the reference detector's active area. The beam diameters delivered to the LUTs under test were between $200 \mu\text{m} - 500 \mu\text{m}$, as measured through mechanical and visual means.

Beam Divergence Characterization

A screen and razorblade are attached to a rail mounted translation stage as shown in **Figure 40**. The beam focus is determined by translating the razor blade into the beam path, and moving its position along the rail such that, when the razor blade is translated into the beam path, the resulting spot on a far field screen uniformly attenuates. Following this, the beam on a screen is measured using a caliper at multiple locations beyond the focus such that a plot can be fit to a line, and the slope extracted and used as the full angle divergence, as is illustrated with the example plot of this in **Figure 41**. The intercept of the plot can give an estimation of the beam waist. It should be noted that this method is measuring the full beam size, and not its full width at half maximum (FWHM).



Figure 40 Divergence measurement apparatus.

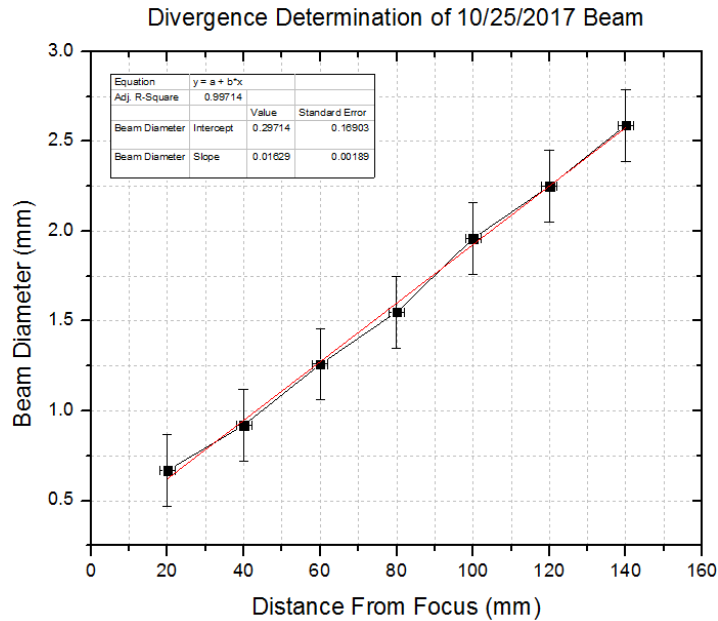


Figure 41 Beam full angle divergence determination.

Here we have assumed that the beam is Gaussian, and not uniform, for example. It should be noted that the measured divergence is not necessarily a divergence of the entire beam, but a beam's exterior component. One can imagine a collimated beam surrounded by a strongly diverging component. A better method of beam characterization would be to use a beam profiler, in order to map the spatial power distribution and divergence. This was not possible with our setup, however, due to the power of the beams used being below that required of the beam profilers available to us.

θ Rotation Ability

All sample holding fixtures and detector fixtures are mounted to a common plate that is subsequently attached to a rotation stage that is operated through the turning of a singular fine tuning knob. Through a series of manual tests, which consisted of turning

the knob and counting the turns until the attached mounting plate rotated 90° , it was determined that it takes ~ 2.08 turns of the knob to complete a 1° rotation. Based on this, a Microsoft Excel formula was created to aid in adjusting the knob to a desired angular setting. Appendix IV gives more detailed information regarding this operation.

ϕ Rotation Ability



Figure 42 Rotation mount insert (top left) providing ϕ adjustment ability. Sample LP on mount in place within rotation stage (top right). 50 mm x 1 mm x 1 mm LP testing in situ (though translated out of the detector for the image) using insert and stage (bottom).

Integrating Sphere (IS) Characterization and Performance Comparison With Photodiode Detector

One practical consideration with using integrating spheres, is that light with a direct line-of-sight to the detection element of the integrating sphere (or output port) can cause erroneous readings. This is why integrating spheres often employ an internal baffle near a sampling port or integrated detector which is simply a physical flap to block light from having a direct line-of-sight to the area. This issue is illustrated in **Figure 43**. An angular sweep (i.e. rotation about an axis through the input aperture of the unit) with a collimated laser source was performed with the integrating sphere (Thorlabs S142C) used for the majority of measurements in this work, in order to better understand the detector's coupling function. The test was repeated with a photodiode detector (Thorlabs S130C) and the results of both are plotted together in **Figure 44**. It is clear that at -50° , for example, (the negative direction leads to direct line-of-sight with the detector element with how the axes have been defined), there is an issue as the power being reported is greater than the power of the source used. The same issue is encountered when testing a physical sample, and is shown in **Figure 45**.

Another practical consideration of using an integrating sphere, is clipping that could result from a divergent source being placed too far away from the input aperture of the integrating sphere. This is illustrated in **Figure 46**. For this reason, most LPs tested with the integrating sphere were positioned slightly beyond its aperture plane.

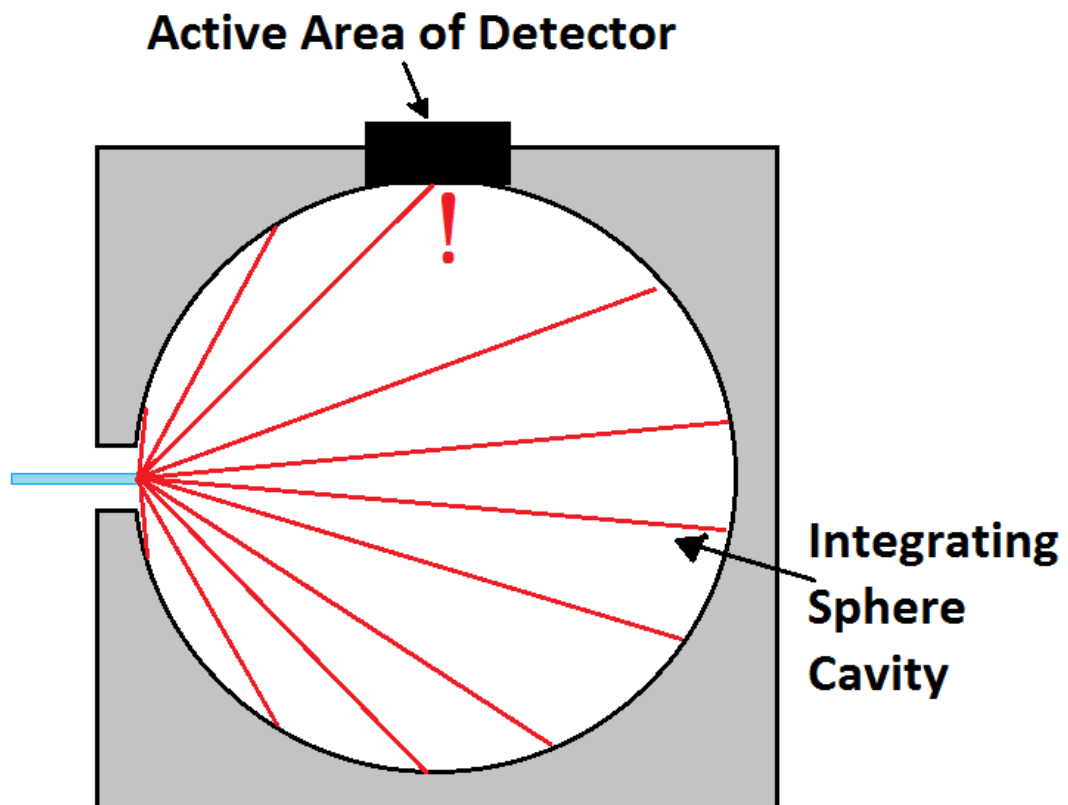


Figure 43 Line-of-sight concern with integrating spheres that do not possess an internal baffle.

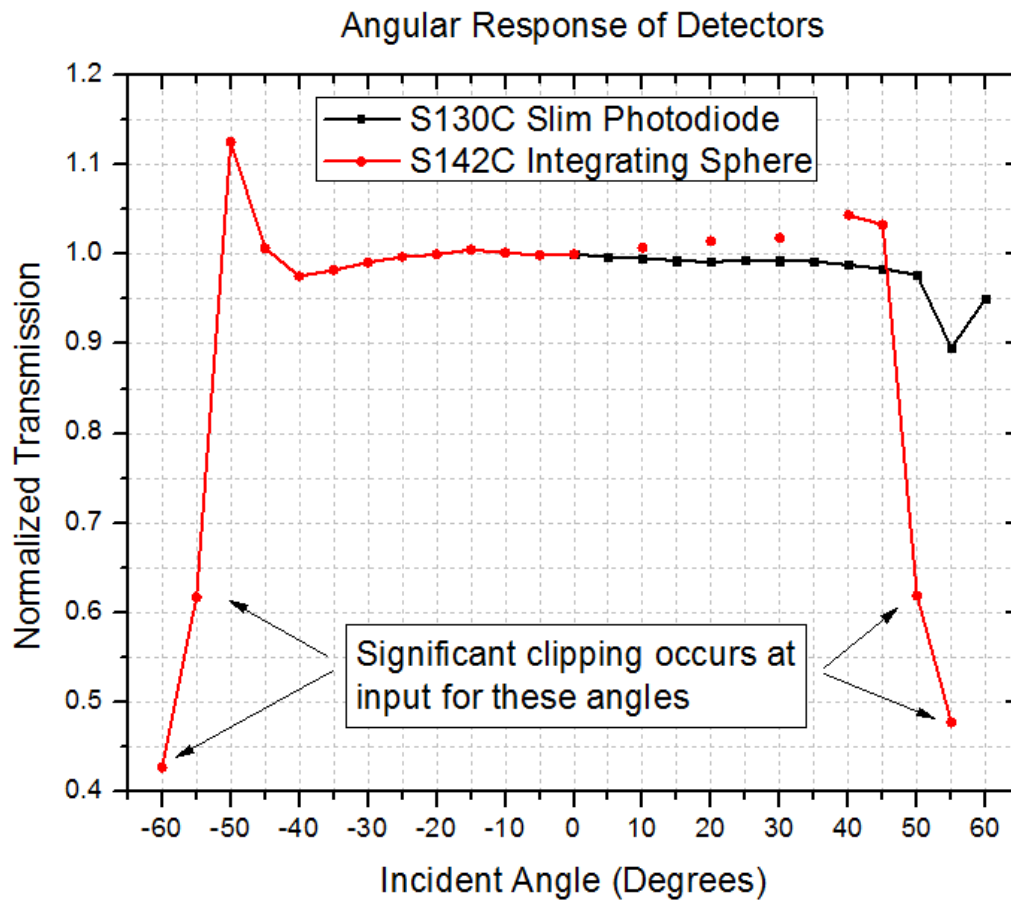


Figure 44 Measured angular response of detectors.

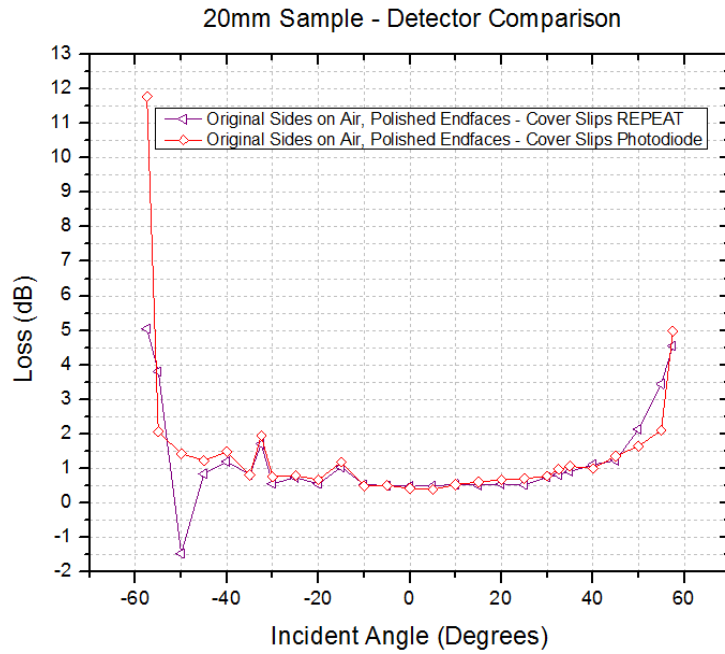


Figure 45 Detector performance comparison when a sample is in place. Note the dip at -50° when an integrating sphere is used.

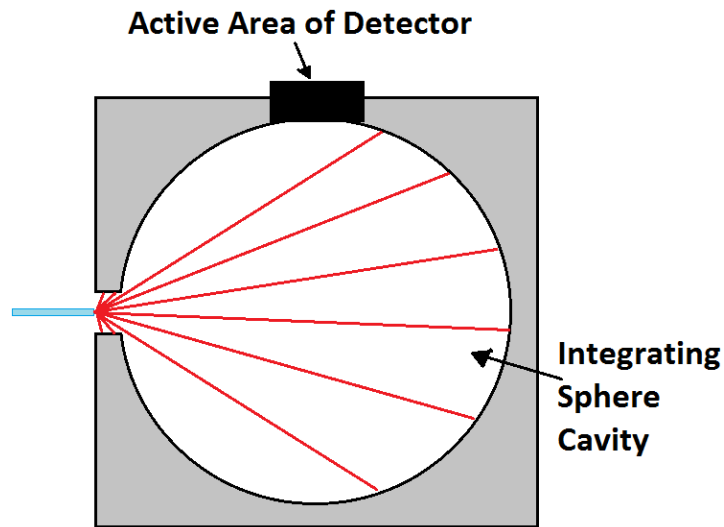


Figure 46 LP Output clipping as a result of poor sample placement.

4.2 Single Channel Light Pipe Measurement Results

Throughout the development of this work, LP mounting, data collection, and preparation quality evolved. In almost all cases, however, testing consisted of varying the incident angle θ as defined in **Figure 47** for rectangular prism LPs, and as defined in **Figure 48** for 45° surface containing LPs. In all results that follow, Fresnel reflection losses are not subtracted from the data.

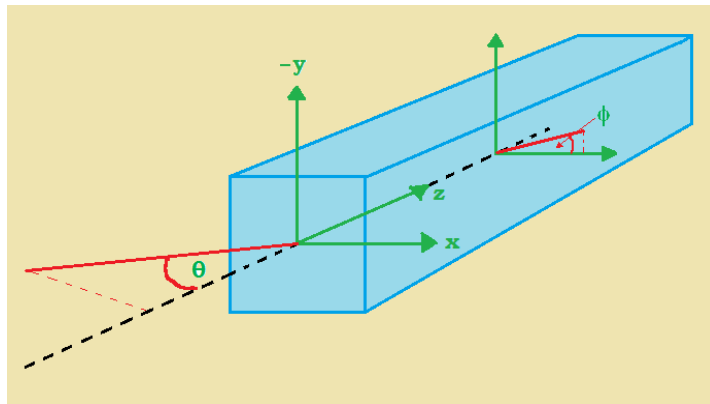


Figure 47 Axis and angular definitions for rectangular prism LPs.

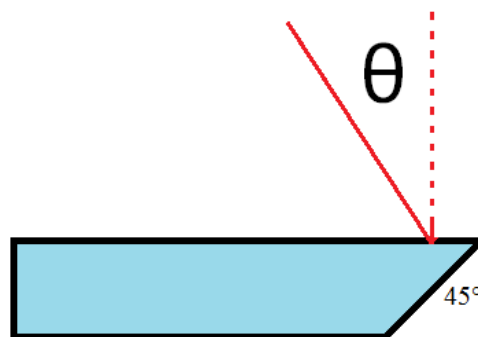


Figure 48 Sign convention for 45° sample input angles.

Rectangular Prism Light Pipes

Early studies utilized a diode laser module (Thorlabs CPS635R and Thorlabs CPS520) and produced results as those shown in the blue plot in **Figure 49**. In the same figure, one can see the same sample subjected to light originating from a supercontinuum source, and passing through a monochromator whereby the linewidth was selected through the monochromator slits to be 30 nm FWHM. A difference in the transmission spectrum is apparent between these two sources and one can infer that, given little change in all other experimental parameters, the loss spikes were related to interference effects within the LP. It should be noted that the study was performed with the sample mounted on a 200 μm deep trench in the substrate, so that $> 60\%$ of the contact area between the LP and the substrate was sure to have a sufficiently thick adhesive layer so as to avoid issues with the evanescent field penetrating into the substrate.

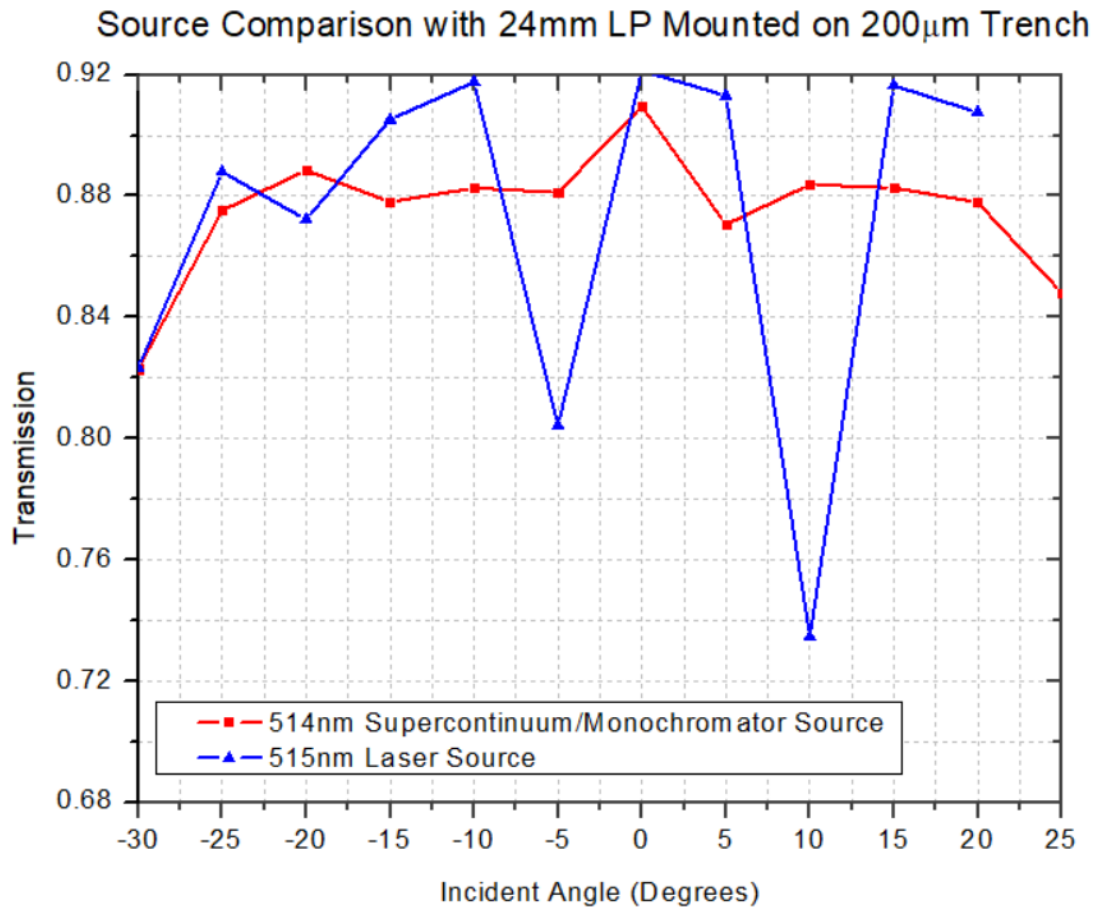


Figure 49 Source comparison between a ~1 nm linewidth source (laser) and a ~30 nm linewidth source (monochromator output). The LP was mounted on top of a 200 μ m deep notch cut in the mounting substrate.

Brief investigations pertaining to polarization dependence were performed and an example result is shown in **Figure 50**. For this study, a polarizer was positioned so that light would be P-polarized (i.e. polarized parallel to the plane of incidence) entering the LP. No significant polarization dependence was observed.

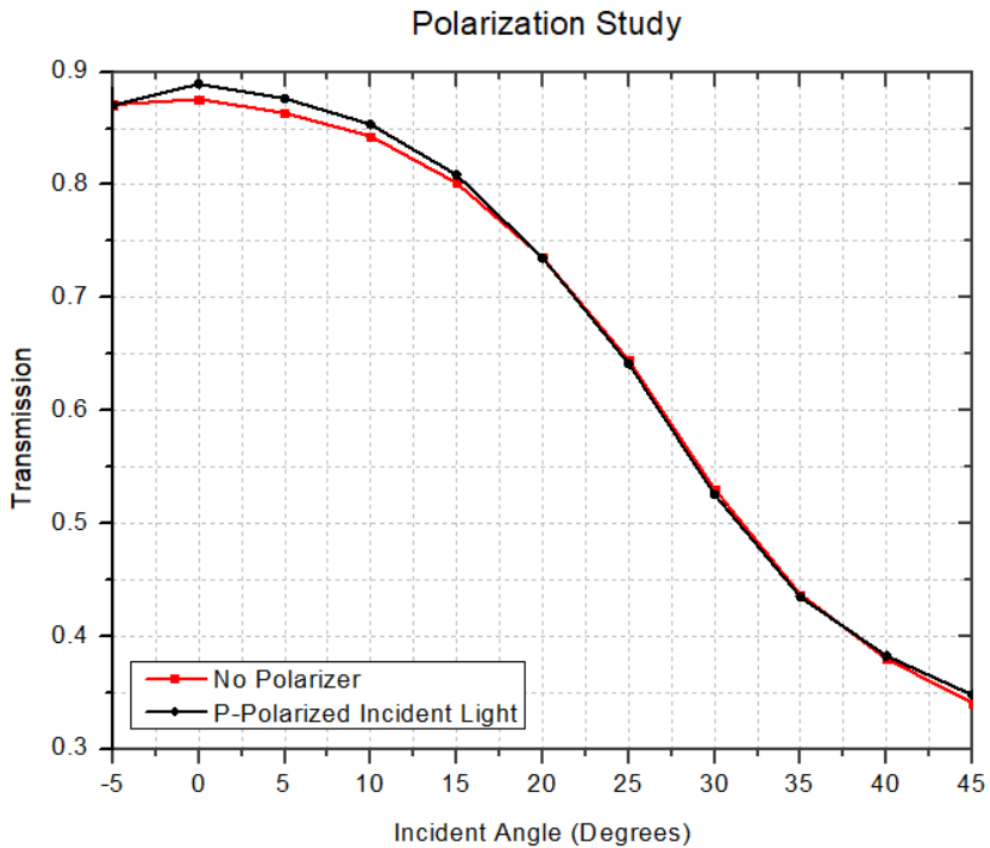


Figure 50 Investigation of polarization dependence on LP transmission properties. The LP used was a 20 mm long sample where the original (i.e. non laser irradiated) sides were interrogated.

In the results that follow, the filtered light of $\lambda = 514 \text{ nm}$ (described in more detail in §4.1) had a full angle divergence of $.92^\circ \pm .11^\circ$, (or $16.3 \text{ mrad} \pm 2 \text{ mrad}$) unless

otherwise stated. Also, it should be assumed that non-coated coverslips were attached to the ends of every sample through an index matched liquid or adhesive, unless otherwise stated.

An LP 70 mm in length was tested such that the θ plane existed orthogonally to the original sides of the LP where one of the original sides provided contact to the two non-coated crossbars through the use of a $n = 1.328$ optical adhesive. An image showing the LP's mounting configuration, as well as the LP during test, are shown in **Figure 51**, while the results of the scan are shown in **Figure 52**. The average transmission of the LP from $\theta = 0^\circ$ to $\theta = 20^\circ$ was 90.1%. This value is not corrected for any loss or coupling mechanisms. Multiple defects and an overall torsion of the sample was observed.

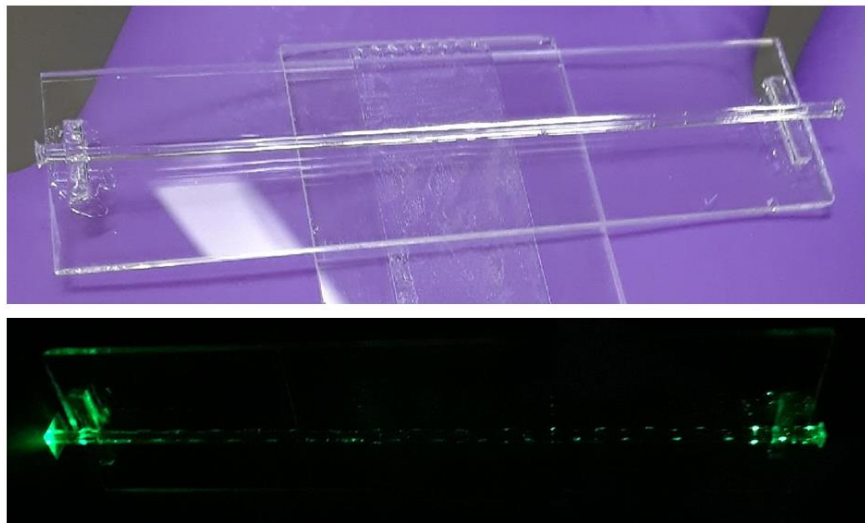


Figure 51 70 mm LP mounted on non-coated crossbars (top) and during testing at $\theta = 45^\circ$ (bottom).



Figure 52 Scan interrogating original sides where one is mounted at two locations to non-coated crossbar supports through the use of a $n = 1.328$ adhesive.

LPs 50 mm in length were tested using multiple mounting arrangements including, but not limited to, bottom surface in majority contact with optical adhesive and the mounting substrate, crossbar supports, and high reflection coated crossbar supports. In the cases of crossbar supports, the crossbars consisted of two sections of 1 mm square glass (borosilicate glass in the uncoated case, and either fused silica or soda lime glass in the

coated cases). Example transmission results between these cases are shown in **Figure 53** and **Figure 54**. Loss is observed in the form of escaping light seemingly originating from the optical adhesive attaching the LP at two individual points to separate high reflection coated crossbars.

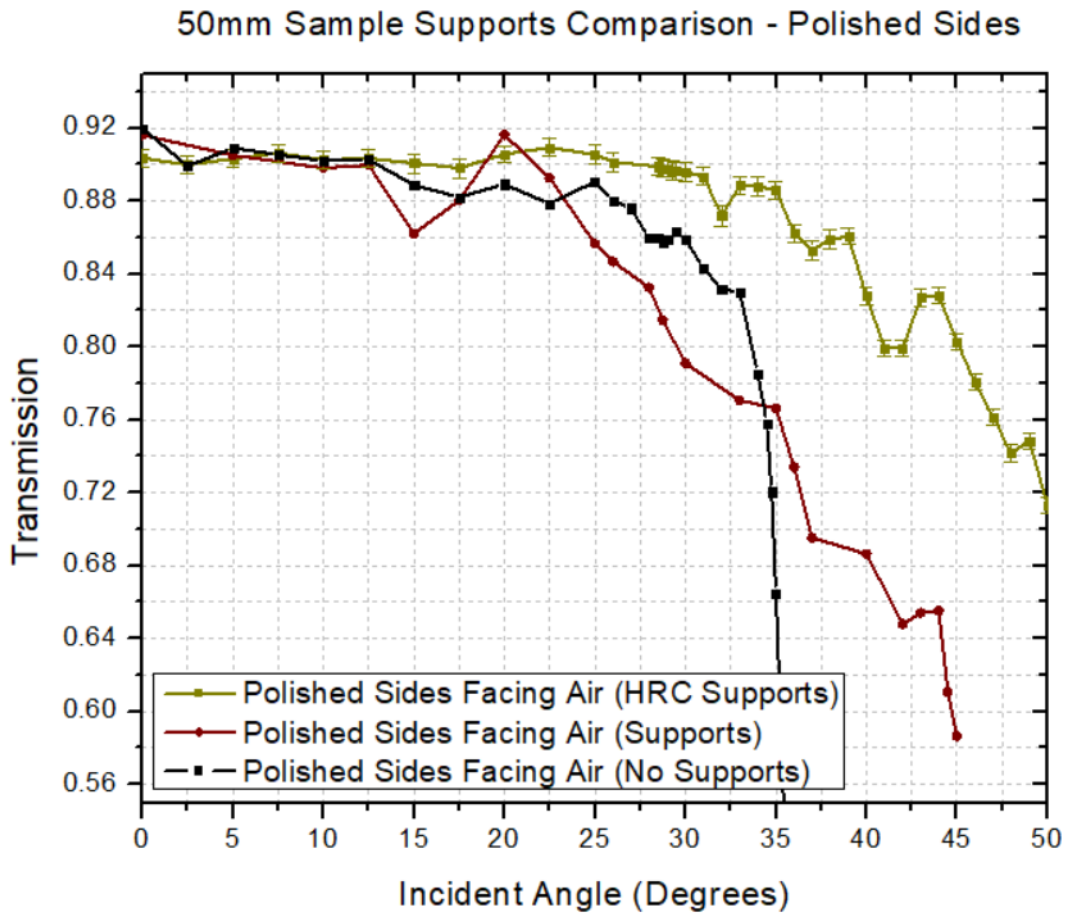


Figure 53 50 mm LP transmission results when the θ scanning plane is orthogonal to the polished sides (of which were facing air) of the LP. The errors bars in the golden plot indicate the latest data collection methodology was used in the measurement process.

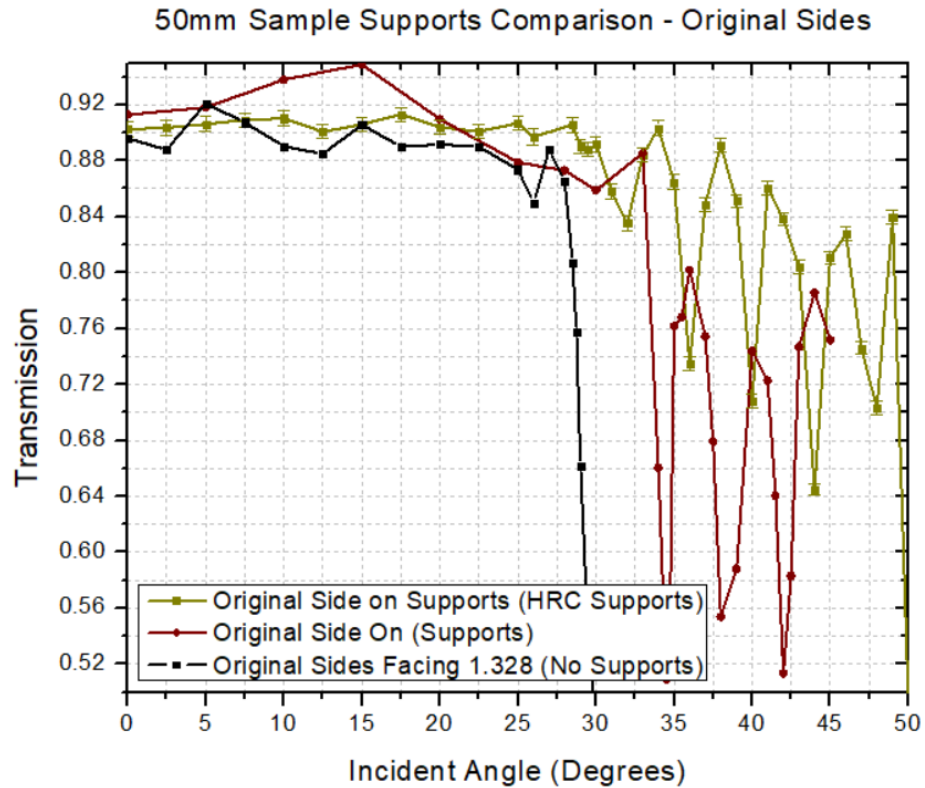


Figure 54 50 mm LP transmission results when the θ scanning plane is orthogonal to the original sides of the LP (one, of which, being in contact with the crossbar supports). The errors bars in the golden plot indicate the latest data collection methodology was used in the measurement process.

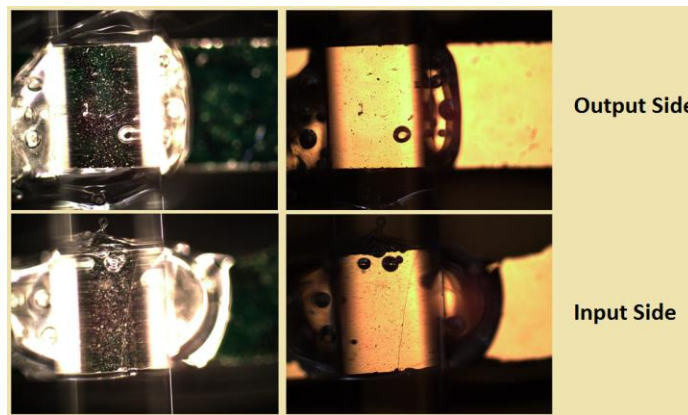


Figure 55 Bond quality between the 50 mm sample and the two crossbar supports. The column on the left features images created using dark field microscopy, while the column on the right features images created using bright field microscopy.

The periodic nature of the original sides scan arises from the fact that, as the incidence angle to the LP is increased, the trajectory of the beam within the LP changes such that an internal reflection does not always avoid a location directly above a bond with a crossbar.

In **Figure 56**, selected plots from the above 50 mm data are plotted along with plots of the loss mechanisms developed in §1.2 that have parameters similar to those corresponding to those of the measured results. This LP was chosen for comparison to loss models over other LPs as it suffered the least form deviations and was closest to an ideal sample though, it should not be considered ideal. It should be pointed out that, while the advertised refractive index of the adhesive used as the lower cladding was 1.328, comparison with the manufacturer's dispersion curve for a representative product (Norland Products Inc. NOA 61) indicates that at the $\lambda = 514$ nm wavelength used for testing, one could possibly expect an index of refraction of closer to $n = 1.338$, which is why this value was chosen as the cladding layer for the calculated curves. While the red and black curves (i.e. the "P. Sides Facing Air (No Supports)" and the " $k = .0001, n_c = 1.338$ " curves) correlate well, the measurement corresponds to an air cladding while the calculation corresponds to an adhesive cladding. While, at the surface this might seem concerning, this actually appears to indicate that there was indeed adhesive on the sidewalls that were not in contact with supports. The reader is reminded of the issue of adhesive migration along the surface of a LP's sidewalls depicted in **Figure 27**. The indication of "(No Supports)" means that the base of the sample, which was an

original/non-polished sidewall, was in full contact with the mounting substrate and was observed to have adhesive existing on at least 25% of its height.

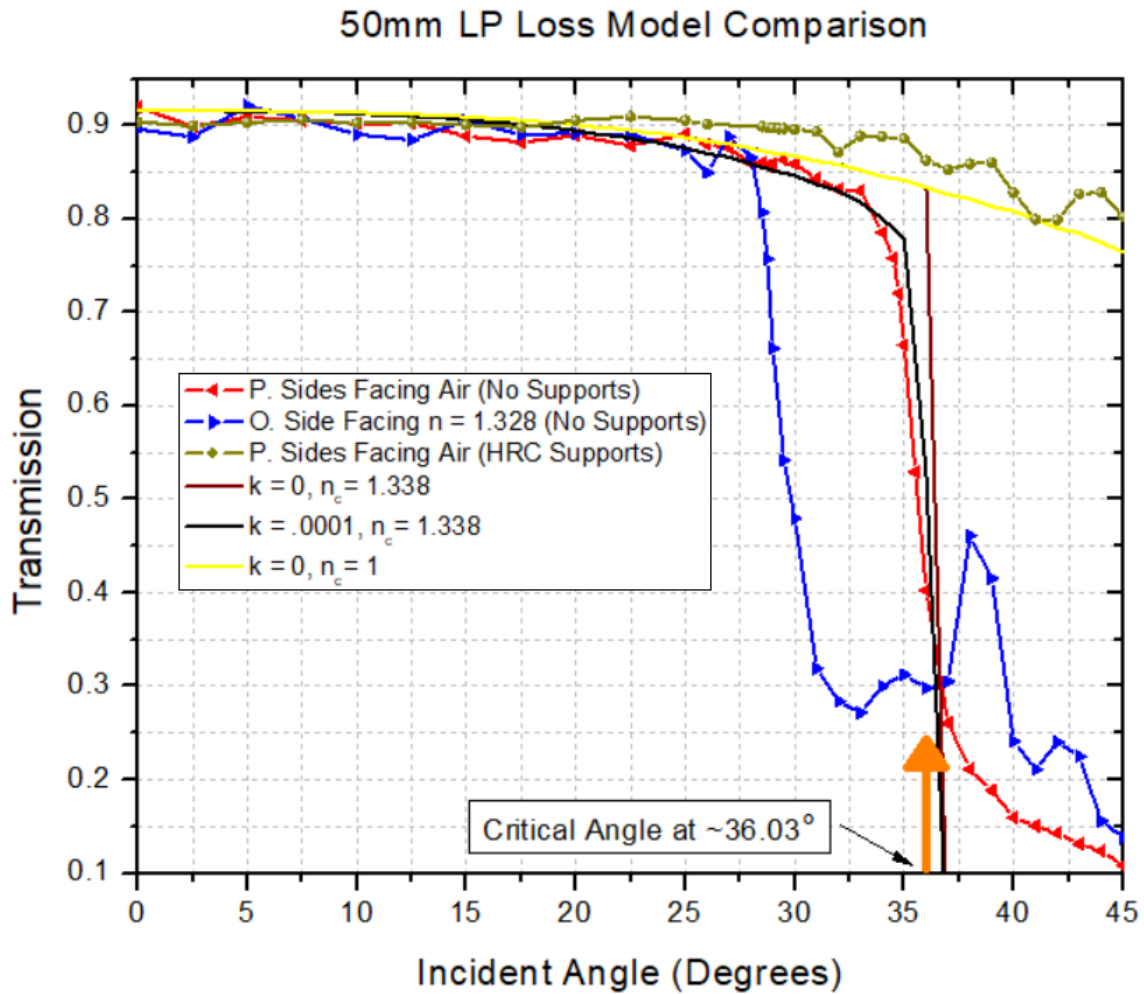


Figure 56 Loss model comparison with data for 50 mm LP. Measured and calculated curves correspond to $\lambda = 514$ nm. The critical angle indicated shows the required incident angle on the LP surface that corresponds to an internal propagation angle equal to the critical angle of the fused silica / adhesive interface. Note that the critical angle for a fused silica / air interface is not achievable even for extreme angles of incidence at the LP input. An RMS surface roughness of 6.36 nm is assumed in all cases.

The notion of adhesive existing on a sample sidewall is further supported by the fact that the transmission of the red curve experiences a sharp roll-off near an angle corresponding to the critical angle between fused silica and the adhesive used when the critical angle between fused silica and air is simply not achievable for any angle of launching at the input of an ideal LP. A similar curve is calculated and shown for the case of $k = 0$, a non-absorbing layer. The comparison between this curve and the $k = .0001$ counterpart illustrates the influence of the absorption on the overall transmission behavior. For acclimation purposes, [28] reports an absorption coefficient of .0004065 for the core and cladding of a polymer-clad fused silica multimode fiber at 1064 nm. Comparing the yellow and gold curves, corresponding to calculated and measured, respectively, light propagation along sidewalls having a true air cladding, one see similar general behavior with fair correlation. Of course, form deviations obfuscate direct comparison, as is the case for all measured data with this LP. One will notice the blue plot in **Figure 56** which corresponds to data from the LP taken when light is launched in a plane orthogonal to the original sidewalls of the LP, with one sidewall in majority contact with the adhesive. One would expect this data to show a roll-off in transmission near the incident angle corresponding to the critical angle of the fused silica / adhesive interface, but it occurs at an earlier angle $\sim 5^\circ$ prior. This can potentially be explained by a rotation of the input face about an axis running through its center and orthogonal to the polished sidewalls (i.e. a “tilted” input facet). This would impart a deflection only in one plane for a perfectly flat endface. Recall that a cover slip was attached to the endfaces of the 50 mm LP, and, while the surface of the endface might have experienced

a finite curvature at its edges due to sidewall polishing, the attached cover slip would provide a far more flat surface for ray-launching. Another explanation could be the change in angular distribution upon launching, perhaps due to the roughness of the input interfaces. The apparent horizontal asymptotes in the blue and red plots are indicative of light that has been scattered and subsequently successfully propagates through the LP. It should be noted that the 50 mm LP was subjected to a methylene chloride liberation, remounting, and an optical alignment process for each dataset.

Results showcasing the full angular rotation ability of the test bench, which includes a φ rotation in addition to the previously presented θ rotation studies, are shown in **Figure 57**. For this study, the full angle divergence of the $\lambda = 514$ nm light source used was 12 degrees, or $210.6 \text{ mrad} \pm 15 \text{ mrad}$. The LP is believed to be the same LP from the previous presented results. For an ideal sample, one would expect a constant value at $\theta = 0^\circ$ for all φ . Additionally, one would expect the same results for $\varphi = 90^\circ$ and $\varphi = 270^\circ$ for all θ , as the theta plane exists parallel to the optical table. Considerations of the non-idealities such as form deviations/imperfections, scratches, non-uniform/non-symmetric adhesive distributions, non-uniform cladding thicknesses at the supports, adhesive migration to unwanted surfaces through surface tension prior to full cure, etc. coupled with the divergence of the beam are predicted to account for much of the variation. As Fresnel losses have not been removed from this data, the report of transmission beyond the expected Fresnel limit at $\theta = 25^\circ$ is attributed to the integrating sphere's integrated detector's line-of-sight issue discussed in §2.3.

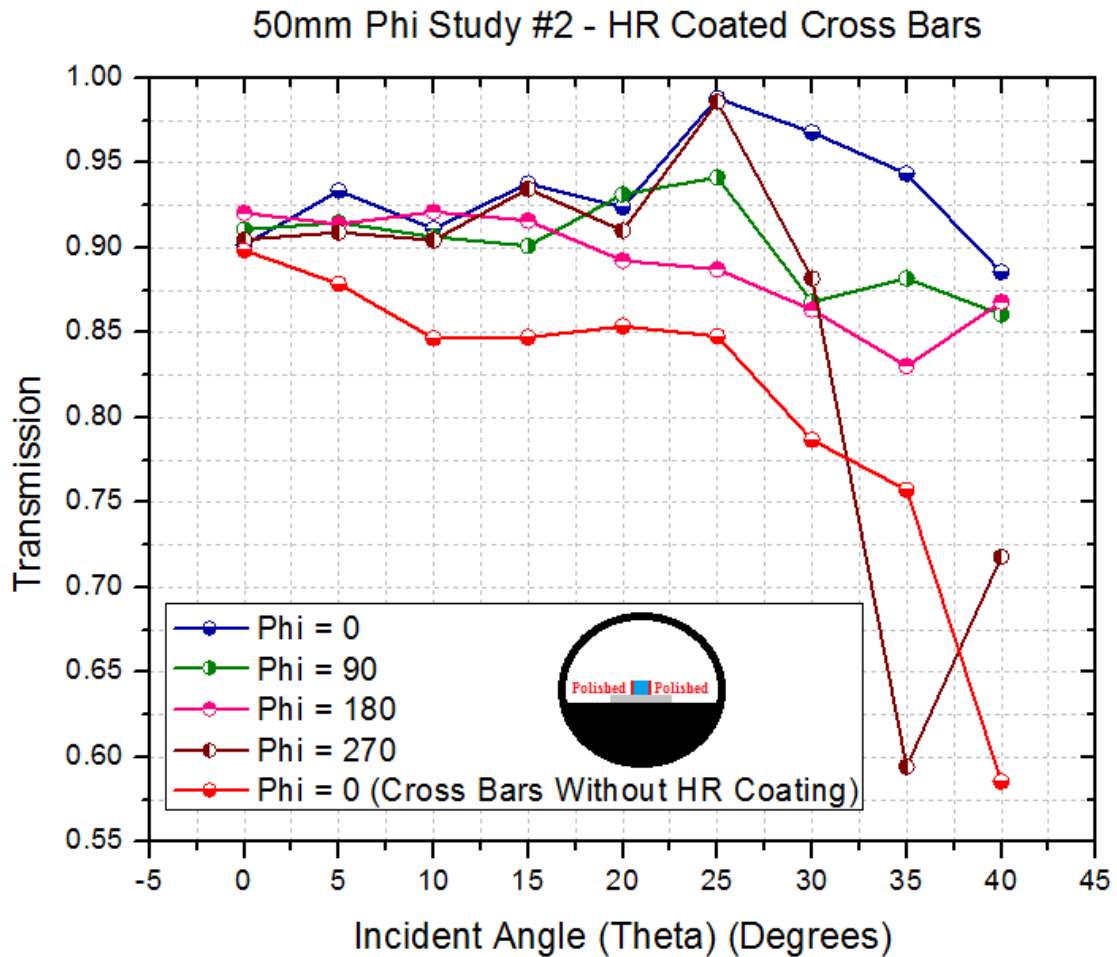


Figure 57 50 mm LP results utilizing the full angular (ϕ in addition to θ) ability of the testing apparatus.

Light Pipes with 45 Degree Turning Surface

Turning surfaces represent a complex polishing issue, due to the bulk volume gradient that exists along a given depth of the surface (i.e. the sharp corner). Early testing of LPs with a 45° turning surface indicated significant loss at positive θ angles. Such a result is shown in plot “1” of **Figure 58** which showcases the transmission results of various LPs whose parameters are described in **Table 3**. This loss is predicted by the fact that the

critical angle between the turning surface and $n = 1$ atmosphere is reached at $\theta \sim 2.67^\circ$, as indicated in **Figure 59**.

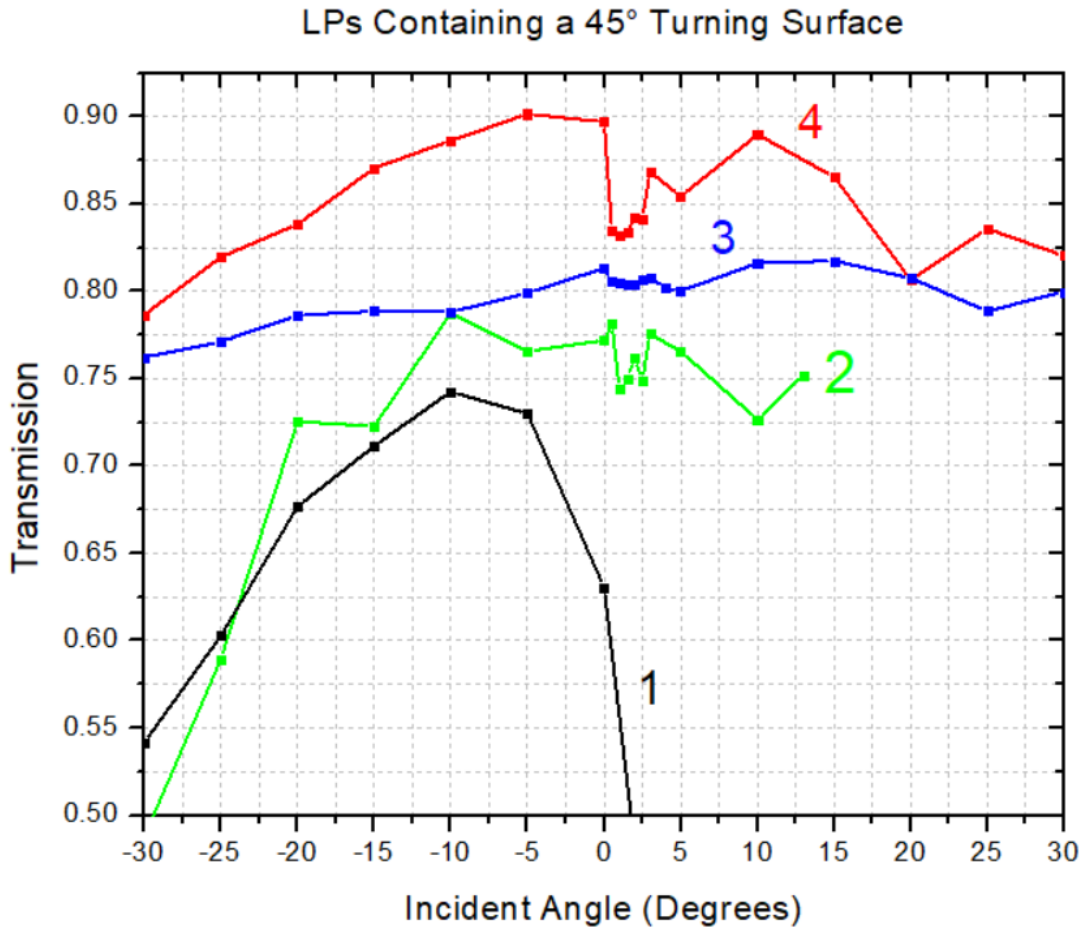


Figure 58 Transmission results of LPs containing a 45° turning surface under various preparation configurations.

Table 3 Properties pertaining to tested, non-identical, LPs containing a 45° turning surface tested with 514 nm center wavelength light.

Label	Length (mm)	Mounting Arrangement	Endface Preparation
1	15	Majority contact with $n = 1.328$ lower cladding/adhesive to mounting substrate.	Unpolished endfaces were bare.
2	10	Mounted on a singular high reflection coated crossbar near the base of the turning surface, which was subsequently mounted to a mounting substrate.	High reflection coated cover slip attached to turning surface, and a non-coated cover slip attached to output. Both were attached via a fused silica index matching liquid.
3	30	Turning surface held by vacuum chuck, no other contact with LP was made.	A high reflection coated cover slip was attached to the turning surface and a non-coated cover slip was attached to the output face. Both items were attached via Norland Products Inc.'s 146H adhesive.
4			A high reflection coated cover slip was attached to the turning surface and a non-coated cover slip was attached to the output face. Both items were attached via Norland Products Inc.'s 85 adhesive.

To mitigate loss arising from the turning surface quality, critical angle violations at the turning surface for positive θ angles, and from LP contact with adhesive, a high reflection coated cover slip piece (see §3.1) was attached to the turning surface using index-matched optical adhesive (Norland Products Inc. 146H or 85) and a high reflection coated crossbar was used as the mounting support for the LP, or the sample was held by vacuum at the back of the high reflection coated cover slip surface. The improvement from a preliminary implementation of these items is evident when comparing plot “1”

with plots “3” and “4” in **Figure 58**. In the cases of plots 2-4, the output of the LP was translated into the integrating sphere detector by ~5 mm. It should be noted that, in the case of the two 30 mm LPs, physically different samples were utilized. In addition, not all LPs were fabricated from the same grade of fused silica substrate.

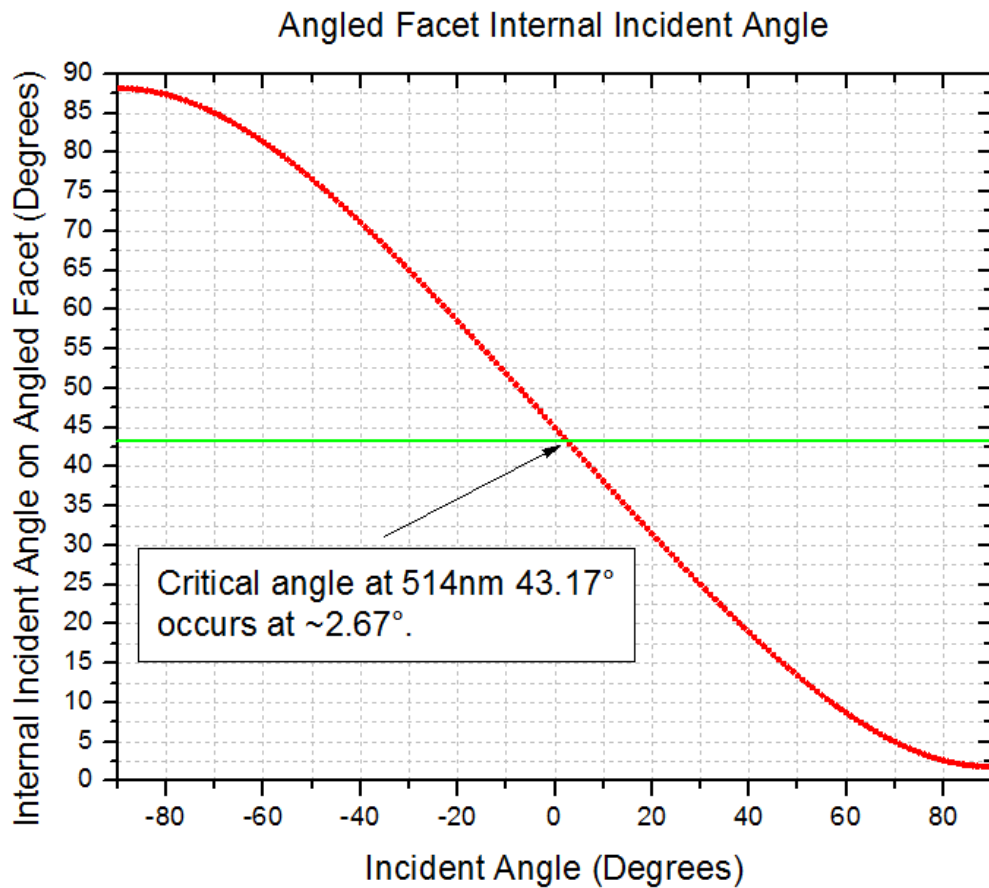


Figure 59 Relationship between the angle incident on the input surface of a 45° sample and the angle incident on the turning surface.

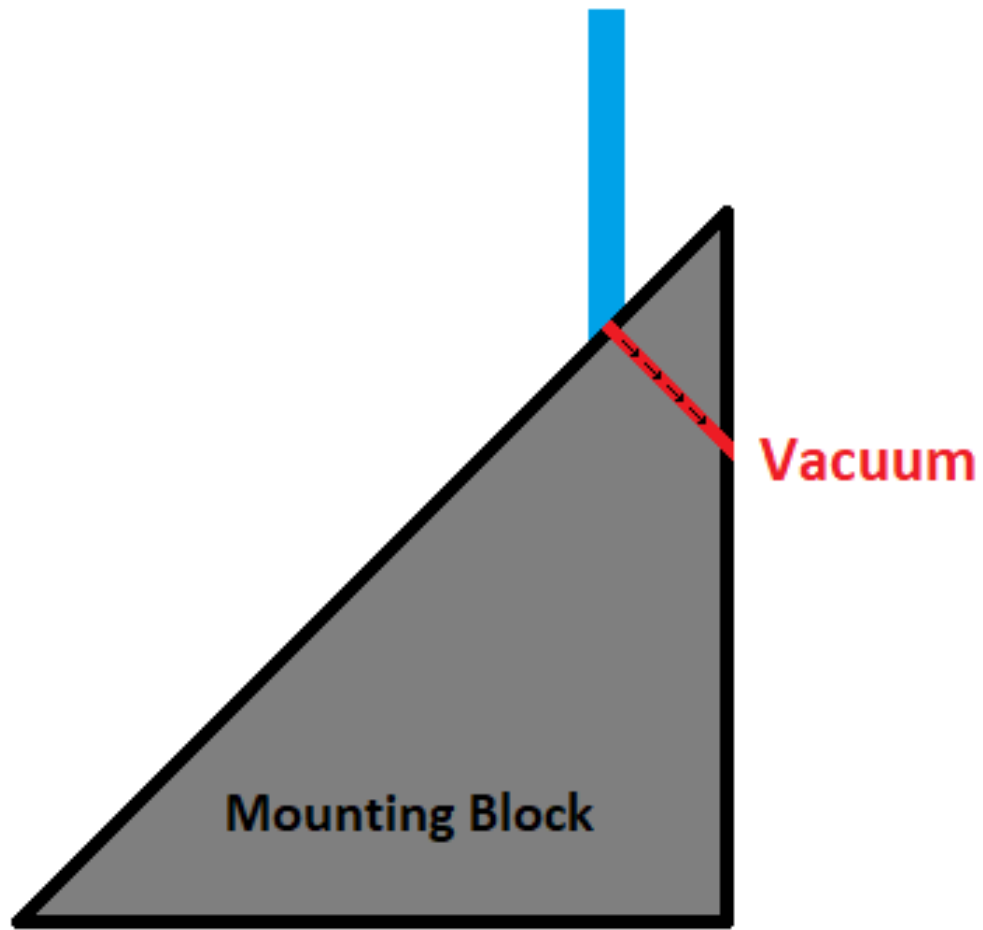


Figure 60 Top view depiction of mounting block used to hold 45° containing LPs via vacuum.

CHAPTER V
SPECTRAL CHARACTERIZATION

5.1 Broadband Source Measurement Apparatus

A block diagram of the broadband measurement configuration of the apparatus is shown in **Figure 61**. In essence, the detector in **Figure 39** is replaced with a 1500 μm core diameter optical fiber (Thorlabs M107L01) connected to an Ocean Optics integrating sphere, which is then subsequently connected to a spectrometer via a multimode fiber optic patch cable. Broadband output from the monochromator is achieved by setting its wavelength (really, the angle of incidence of light on its internal diffraction grating) to its lowest possible setting. This results in making the diffraction grating perform as a broadband mirror, though not with a uniform reflection spectrum. This is not an issue, as the detection methodology simply reports a percentage of the incident power.

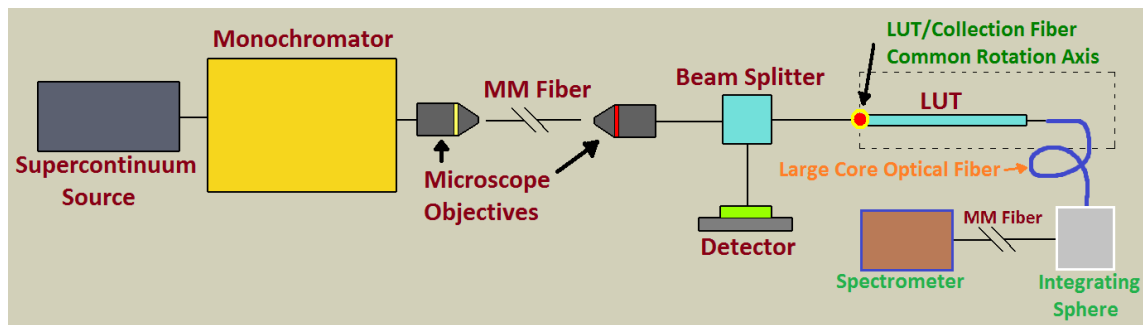


Figure 61 Broadband transmission measurement apparatus.

5.2 Results

Broadband LP transmission measurements for the spectral range of 525 nm to 750 nm are shown in **Figure 62**. The sample used is the same 50 mm sample used to produce the results from §4.2, and was mounted on crossbars. Due to the fact that the light sampled by the spectrometer is from the integration sphere and represents a small fraction of the total power of the original beam (on the order of 100 mW at full transmission), it was necessary to set the integration time of the spectrometer to 1 second, and 10 averages were performed per collection. Using a higher power light source would result in far smoother plots, as the signal would be farther in proximity to the device's noise floor. The variance in the signal increases at increasing wavelengths due to the detection limitations of the detector integrated into the spectrometer. The design of the apparatus allows for the broadband characterization of LPs, with the spectral range currently limited by the choice of spectrometer or other spectral analysis device. At 525 nm, the transmission at zero incidence is ~87%, compared with a previous result using a narrowband source with a photodiode-equipped integrating sphere of ~90%. In order to provide data to validate the wavelength-dependence of the appropriate loss mechanisms, a greater wavelength range is required for testing. This setup allows for the fiber-coupled attachment of additional spectrometers or other similar devices in order to achieve that in the future.

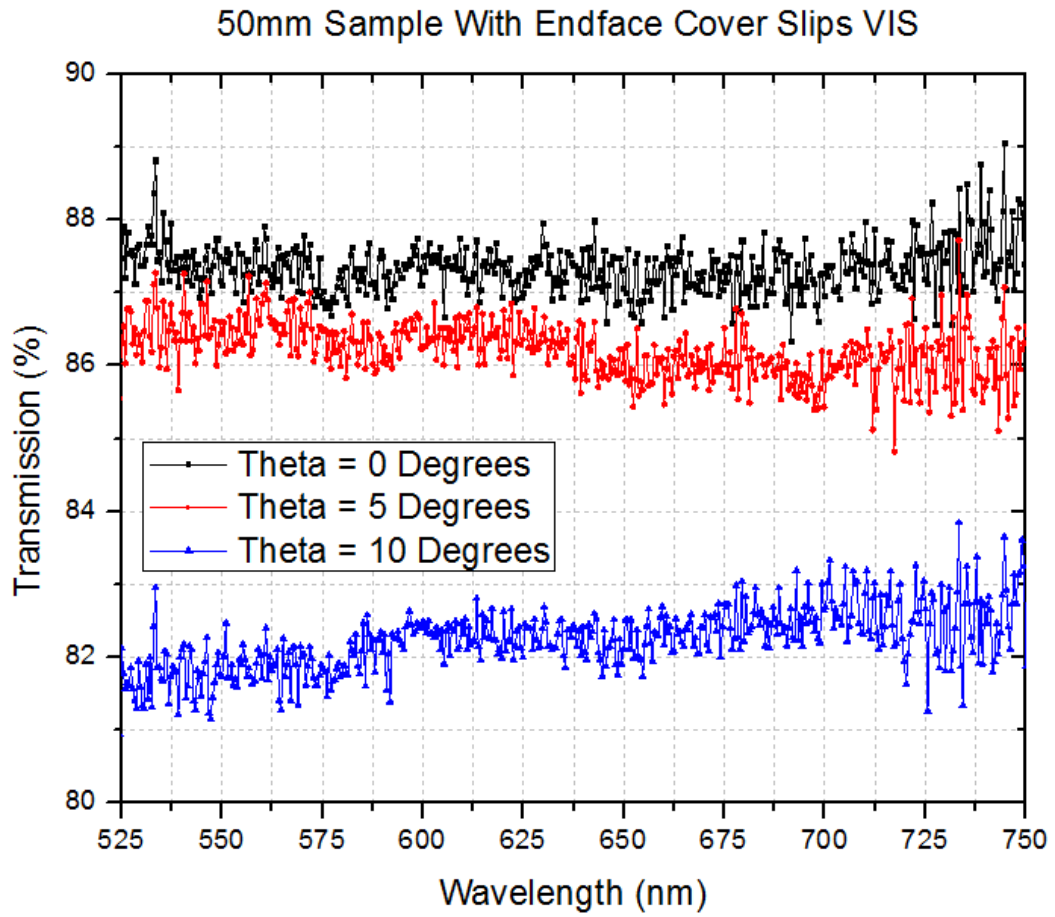


Figure 62 Broadband testing result as a function of incidence angle using a 50 mm x 1 mm x 1 mm sample.

CHAPTER VI

PREPARATIONS TOWARD MULTI-LENS ELEMENT COUPLED TO MULT-LUT - DETECTOR CHARACTERIZATION

The LPs fabricated in this work were intended to be used in a solar concentrating prototype and used in conjunction with multijunction photovoltaic cells (MJPVs) for energy harvesting. The first stage of this realization involves the testing of a single channel LP with a 45° turning surface used in conjunction with a silicon photodiode, in order to provide a basis for process and methodological development and is the subject of this chapter.

6.1 Experimental Arrangement

The apparatus used to test the single channel LP is shown in **Figure 63**. A 2800 lumen high intensity lamp (Thorlabs HPLS-30-04) was used as the source of the measurements. A large iris was positioned at the output of the lamp in order to provide less divergent rays to the 10x microscope objective (having a corresponding numerical aperture of .25) as well as to block the more divergent light from the lamp from directly seeing the photodiode used for measurement. The LP followed the microscope objective and was held via vacuum by the back of the high reflection coated cover slip adhered to its turning surface. The LP used was the same LP used to create plot “3” featured in **Figure 58** however, the cover slip adhered to the output was removed and the adhesive was left on the output in the form of the cover slip surface.

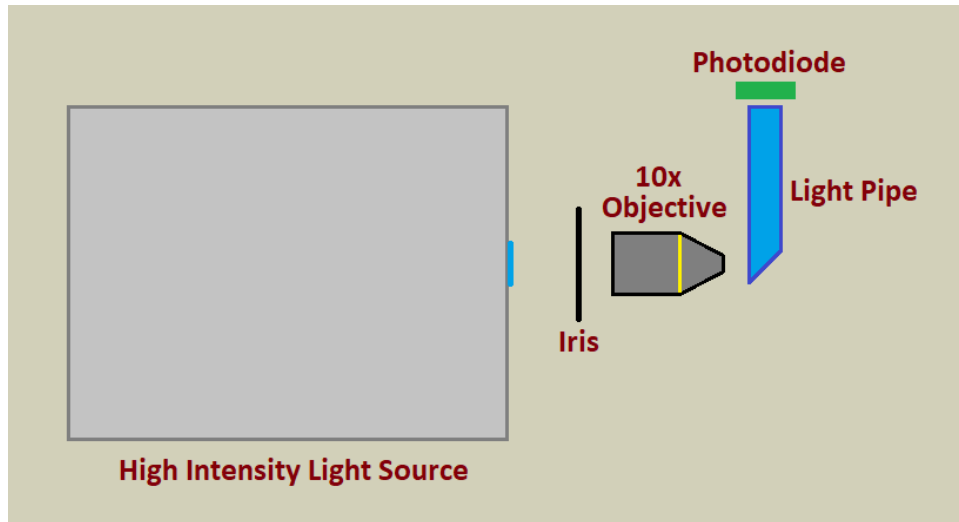


Figure 63 Block diagram of single channel LP photodiode testing apparatus.

6.2 Silicon Photodiode

Silicon photodiodes were obtained from Digikey (751-1015-ND). These particular photodiodes have a ~1 mm thick encapsulant/coating on them which adds another reflection interface when used for measurements. A fairly standard photodiode amplifier circuit was built from [20] and is shown in **Figure 64**. It was necessary to choose the value of the resistor such that the output would not saturate when exposed to light having a power density of $\sim 500 \text{ W/m}^2 - 1000 \text{ W/m}^2$, as this is the power density we could expect from outdoor testing conditions. The resistor value was also chosen such that the corresponding voltage output approached, but was less than, 5 V when used with light of the previously stated power density. This was done so that the voltages could be read simultaneously by Arduino analog voltage inputs which have a maximum input voltage rating of 5 V. The source specified in the previous section (Thorlabs HPLS-30-04) was

used for this process. The operational amplifier integrated circuit used was a Texas Instruments LF356N JFET input operational amplifier (they offer high bandwidth and low voltage and current noise, among other attractive features for this application), and a low tolerance 5-band 1.5 k Ω resistor was used. Three identical circuits were constructed on an electronics prototyping board to be used with three identical photodiodes as shown in **Figure 65**. The voltage across the output to ground was fed into an Arduino Uno board in order to collect the voltages from all three photodiode circuits at approximately the same time in order to avoid deviation in values arising from the movement of the sun through the sky relative to the module on the surface of the Earth when tested outdoors, or from the fluctuation in source intensity when used indoors. One photodiode is intended for mounting to the lens array at the input side to provide a reference value, another for mounting after the lens array to speak to the performance of a lens array element, and a third photodiode for being placed at the output of a given test structure to provide total performance information in the wavelength range applicable to the photodiodes. An example of this is shown without a LP in place in **Figure 66**.

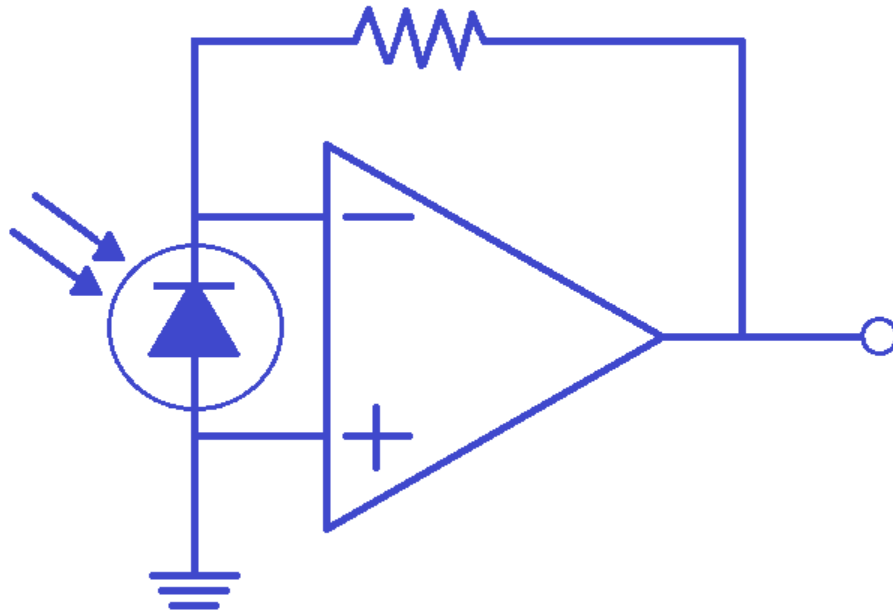


Figure 64 Amplifier circuit used with photodiodes for testing solar module performance.

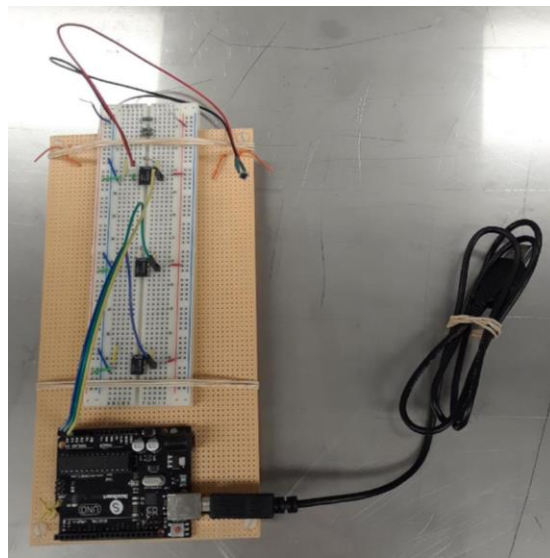


Figure 65 Arduino/protoboard layout of amplifier circuits used with the silicon photodiodes.

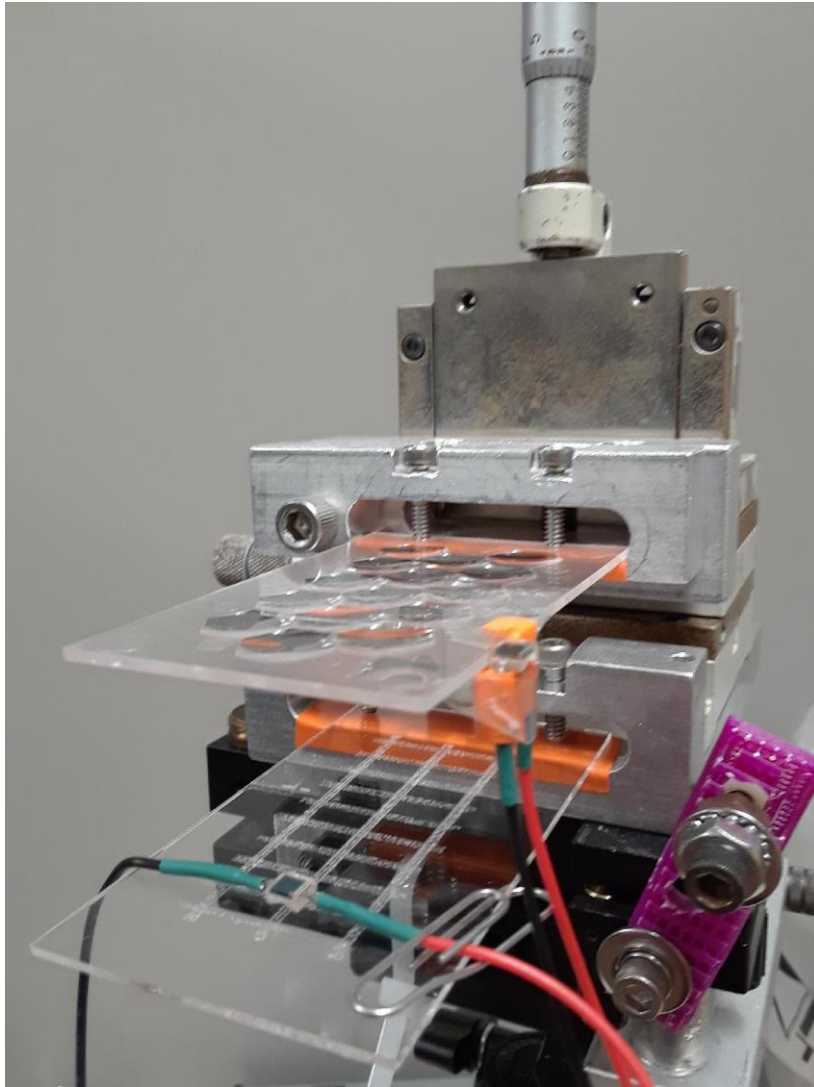


Figure 66 Total module testing apparatus with silicon photodiodes attached to provide at-lens and after-lens reference values.

6.3 Results

The voltage measurements of the experiment are tabulated in **Table 4**. Comparing voltages only, this yields a LP with a high reflection coated cover slip assisted turning surface efficiency of $77.06\% \pm .40\%$. It is thought that the performance of the LP suffered from the non-ideal quality of the turning surface and this result is not representative of the best LPs created thus far.

Table 4 Results of silicon photodiode testing of 45° containing LP.

Description of Measurement	Measured Voltage (V)
Photodiode positioned after microscope objective at LP input location	$4.12 \pm .02$
Photodiode positioned at end of LP with adhesive flat (no cover slip but adhesive remaining) separated by air gap	$2.838 \pm .005$
Photodiode positioned at end of LP with adhesive flat (no cover slip but adhesive remaining) using fused silica index matching liquid (no air gap)	$3.175 \pm .006$

The transfer function of a lens array element was characterized by scanning an approximate 800 um diameter beam from the corner of one lens element to its opposing corner (recall that the shape on an individual lens element is a hexagon). This was done using the three different data collection methodologies used throughout the course of this work and their results are shown in **Figure 67**. From extensive use and observation, the

data collection methods used to create the red and black plots (i.e. not the “Python Script” method), carried an ~5% uncertainty at worst case, with results varying by 2% during repeatability tests.

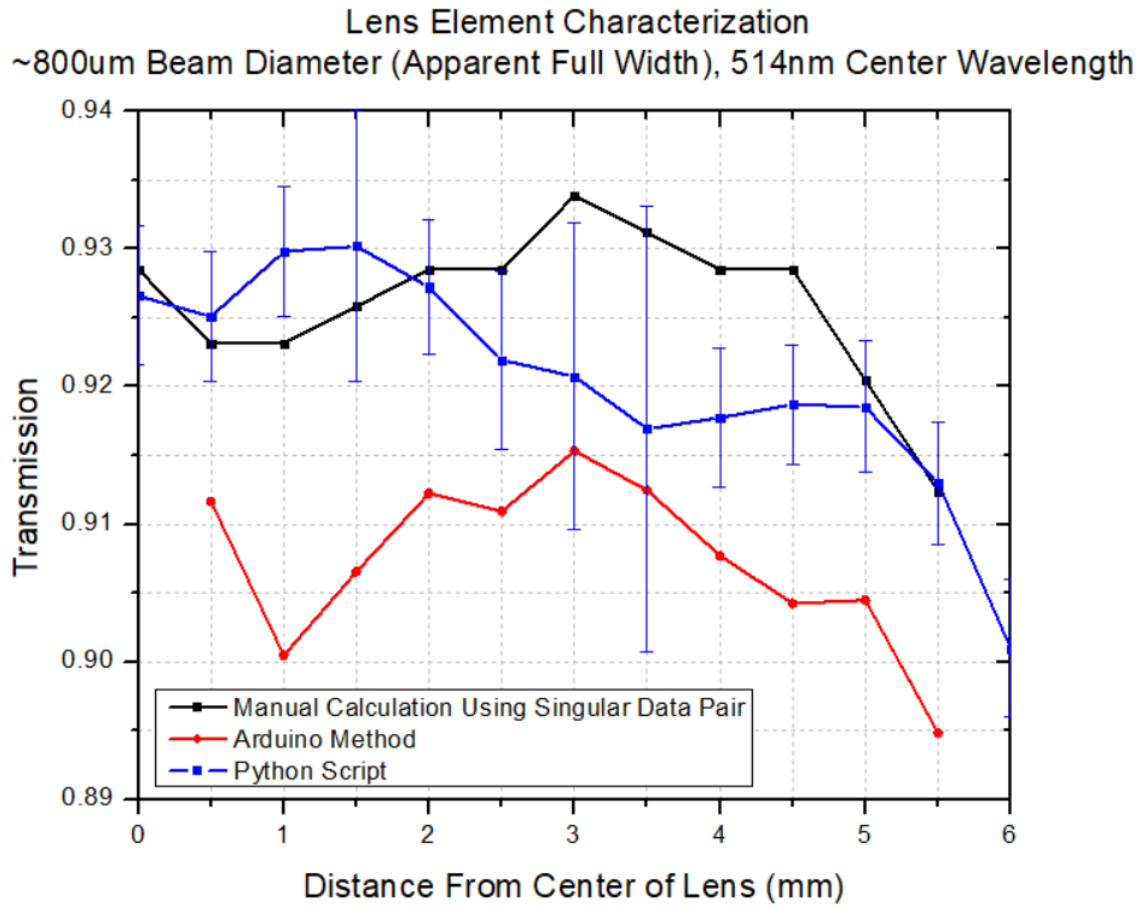


Figure 67 Lens element characterization.

CHAPTER VII

SUMMARY, CONCLUSIONS, AND FUTURE WORK

This work serves as a common-ground starting point for the detailed analysis of the transmission of light through light pipes. Light pipe assembly methodologies were created with feedback from measurement results and loss analysis that directed their evolutionary path to provide effective mounting that minimizes the introduction of loss. Culprits of assembly loss often deal with adhesive migration during mounting to unwanted areas. As one would expect, a lower refractive index cladding provides better transmission over a larger distribution of propagation angles, which is why minimizing light pipe contact with higher than unity refractive index adhesives maximizes performance. The physical application of adhesive to a light pipe and/or its mounting substrate was investigated through various means that would offer the possibility of large volume scaling. This endeavor led to the conclusion that a key parameter related to dispensing adhesive is its viscosity, with the higher viscosity adhesives being more easily contained to an intended area. Future studies should work to enhance adhesive control, as such an ability would allow for better characterization of loss mechanisms and overall LP performance.

The mitigation of end facet roughness by means other than polishing was investigated and led to the development of endcap production and application processes. The most promising endcap choice was to use commonly available microscope cover slips cut to

size and attached via liquid or adhesive index-matched to the light pipe material. Critical factors to the success of using such endcaps were essentially the same factors encountered with the adhesive investigations, namely, the change in cross-sectional geometry of the light pipe due to the unwanted migration of the index-matching material to sidewalls driven by behavior related to the viscosity of the index matching material. A logical and prudent future investigation would be related to lifetime studies pertaining to the adhesives and index-matching materials. As the optical adhesives are ultraviolet-cured polymer based adhesives, it would be indicated to look into the effects of photodegradation on the transmission ability of a light pipe mounted using such a material, especially if the intended application of the assembled unit includes significant exposure to ultraviolet light, as is the case for light pipes used in solar concentrators.

A two-axis rotation test bench was developed that offers the ability to launch broadband light similar in spectral content to the broadband source used, or narrowband light, both of which are determined by the use of a monochromator in conjunction with a supercontinuum light source. The two-axis rotation ability, merged with precision translational control, allows for the launching of rays at an arbitrary location and incidence angle, offering the ability to perform unique and numerous transmission/loss studies including, but not limited to, skew ray studies, meridional ray studies, and launching into light pipe core/cladding interfaces. These abilities provide a way to experimentally test various loss mechanisms with physical samples. A logical future step would be to enhance the speed by which measurements can be made while

simultaneously minimizing the need for human presence through automation, in addition to increasing the available wavelength-detection range for broadband verification of loss dependencies.

A result made possible by the aforementioned accomplishments is the identification of various dominant loss mechanisms inherent to light pipe structures used in this work. A significant concern, that of evanescent field coupling to a mounting substrate, is easily avoided through the use of a sufficiently thick cladding layer. In the case of visible light with the optical adhesives used in this work, a thickness layer of $> 10 \mu\text{m}$ is sufficient to contain visible light incident on a core/cladding interface at angles approaching within $.1^\circ$ of the associated critical angle. The identification of various loss mechanisms also provides possibilities for tailoring light pipe structures and mounting for intentional loss and subsequent filter applications. This is evidenced by the preliminary frustrated total internal reflection analysis.

Preliminary testing of a single channel light pipe containing a turning surface using an inexpensive silicon photodiode with $\lambda = 514 \text{ nm}$ light yielded a LP efficiency of $77.06\% \pm .40\%$ when produced voltages were used with a less than ideal sample.

A 70 mm and 50 mm LP were shown to, under particular mounting conditions and without subtracting Fresnel reflection losses, guide an average of 90.1% of light from $\theta = 0^\circ$ to $\theta = 20^\circ$, and 90.6% of light from $\theta = 0^\circ$ to $\theta = 25^\circ$, respectively.

REFERENCES

- [1] “Light Pipes - Homogenizing Rods | Edmund Optics.” Edmund Optics Worldwide, 2017, www.edmundoptics.com/optics/prisms/light-pipes-homogenizing-rods/.
- [2] W. J. Cassarly, “Lightpipe Design,” in *Illumination Engineering: Design with Nonimaging Optics*, John Wiley & Sons, Inc., 2013.
- [3] A. J. Whang, J. Chuang Chun-Hsien, and Y.-Y. Chen, “Analysis of light guiding property in light piped based solar concentrator,” 2008, vol. 6896, p. 68961A–68961A–10.
- [4] Y. Liu, R. Huang, and C. K. Madsen, “Design of a lens-to-channel waveguide system as a solar concentrator structure,” *Opt. Express*, vol. 22, no. 102, pp. A198–A204, Mar. 2014.
- [5] C. Hu, Dogan Y., Morrison M. T., Nanda A., Ma D., et al., “High Efficiency Glass Waveguiding Solar Concentrator,” presented at the IEEE Photovoltaic Specialist Conference, Washington DC, 2017.
- [6] J. T. Remillard, M. P. Everson, and W. H. Weber, “Loss mechanisms in optical light pipes,” *Appl. Opt.*, vol. 31, no. 34, pp. 7232–7241, Dec. 1992.
- [7] J. F. Van Derlofske and T. A. Hough, “Analytical model of flux propagation in light-pipe systems,” *Opt. Eng.*, vol. 43, no. 7, pp. 1503–1510, 2004.
- [8] R. J. Koschel and A. Gupta, “Characterization of lightpipes for efficient transfer of light,” in *SPIE*, 2005, vol. 5942, pp. 594205-594205–12.

- [9] H. Baghsiahi, K. Wang, W. Kandulski, R. C. A. Pitwon, and D. R. Selviah, "Optical Waveguide End Facet Roughness and Optical Coupling Loss," *J. Light. Technol.*, vol. 31, no. 16, pp. 2959–2968, Aug. 2013.
- [10] H.-M. Lee, M.-C. Oh, H. Park, W.-Y. Hwang, and J.-J. Kim, "End-face scattering loss in integrated-optical waveguides," *Appl. Opt.*, vol. 36, no. 34, pp. 9021–9024, Dec. 1997.
- [11] Y. Park, "Surface Roughness Effects on Light Propagation in Optical Light Pipes," *Grad. Theses - Phys. Opt. Eng.*, Jul. 2016.
- [12] Nahida J.H. Spectrophotometric analysis for UV-irradiated PMMA // *International of basic & Applied Science, IJBAS-IJENS 2012. Vol.12. No.02. P. 58-67.*
- [13] Keiser, Gerd. *Optical Fiber Communications*. 3rd ed., McGraw-Hill, 2000.
- [14] Zhu, S., Yu A. W., Hawley D., and Roy R., "Frustrated Total Internal Reflection: A Demonstration and Review." *American Journal of Physics*, vol. 54, no. 7, 1986, pp. 601–607., doi:10.1119/1.14514.
- [15] "Photodiodes." *Photodiodes*, Thorlabs, 2018, www.thorlabs.com/newgrouppage9.cfm?objectgroup_id=285.
- [16] Pedrotti, Frank L., Pedrotti, Leno M., Pedrotti, Leno S. *Introduction to Optics*, Cambridge University Press, 2007.
- [17] Malitson. "RefractiveIndex.info." *Refractive Index of SiO₂ (Silicon Dioxide, Silica, Quartz)* – Malitson, 2018, refractiveindex.info/?shelf=main&book=SiO2&page=Malitson.

- [18] Harvey, James E. "Total Integrated Scatter from Surfaces with Arbitrary Roughness, Correlation Widths, and Incident Angles." *Optical Engineering*, vol. 51, no. 1, June 2012, p. 013402., doi:10.1117/1.oe.51.1.013402.
- [19] Baghsiahi H., Wang K., Kandulski W., Pitwon R. C. A., Selviah D. R., "Optical Waveguide End Facet Roughness and Optical Coupling Loss." *Journal of Lightwave Technology*, vol. 31, no. 16, 2013, pp. 2659-2668., doi:10.1109/jlt.2013.2271952.
- [20] Protopopov, Vladimir. *Practical Opto-Electronics an Illustrated Guide for the Laboratory*. Springer International Publishing, 2014.
- [21] Chaves, Julio C. *Introduction to Nonimaging Optics*. CRC Press / Taylor & Francis Group, 2008.
- [22] Canada, Laserline Optics. "Powell Lens Buyer's Guide." Laserline Optics Canada, 2018, www.laserlineoptics.com/powell_primer.html.
- [23] Snyder, Allan W., Love, John D., "Goos-Hänchen shift." *Journal of Applied Optics*, vol. 15, pp. 236-238, 1976.
- [24] Bliokh, K.Y., Aiello, A., "Goos-Hänchen and Imbert-Fedorov beam shifts: an overview." *Journal of Optics*, vol. 15, n. 1, 2013.
- [25] G. Y. Chen, D. Otten, Y. Q. Kang, T. M. Monro, and D. G. Lancaster, "Measuring the Radial Position of Defects within Optical Fibers Using Skew Rays," *Journal of Sensors*, 2017.

- [26] G. Y. Chen, T. M. Monro, and D. G. Lancaster, “Detection of microscopic defects in optical fiber coatings using angle-resolved skew rays,” *Opt. Lett., OL*, vol. 41, no. 17, pp. 4036–4039, Sep. 2016.
- [27] G. Y. Chen, C. A. Codemard, P. M. Gorman, J. S. Chan, and M. N. Zervas, “Angle-Resolved Characterization and Ray-Optics Modeling of Fiber-Optic Sensors,” *Journal of Lightwave Technology*, vol. 33, no. 24, pp. 5210–5217, Dec. 2015.
- [28] G. Y. Chen, C. A. Codemard, M. N. Zervas, T. M. Monro, and D. G. Lancaster, “Enhanced Pump Absorption of Active Fiber Components With Skew Rays,” *Journal of Lightwave Technology*, vol. 34, no. 24, pp. 5642–5650, Dec. 2016.
- [29] Horiba. “Throughput and Etendue – HORIBA.”
<http://www.horiba.com/us/en/scientific/products/optics-tutorial/throughput-etendue/>. 2018.
- [30] Loturco, S, et al. “Hybrid Chemical Etching of Femtosecond Laser Irradiated Structures for Engineered Microfluidic Devices.” *Journal of Micromechanics and Microengineering*, vol. 23, no. 8, 2013, p. 085002., doi:10.1088/0960-1317/23/8/085002.

APPENDIX I

2D GEOMETRICAL AND MATHEMATICAL DESCRIPTIONS OF SINGULAR RAY TRAJECTORIES IN BASIC LIGHT PIPE STRUCTURES

A1.1 2D Rectangular Prism LP

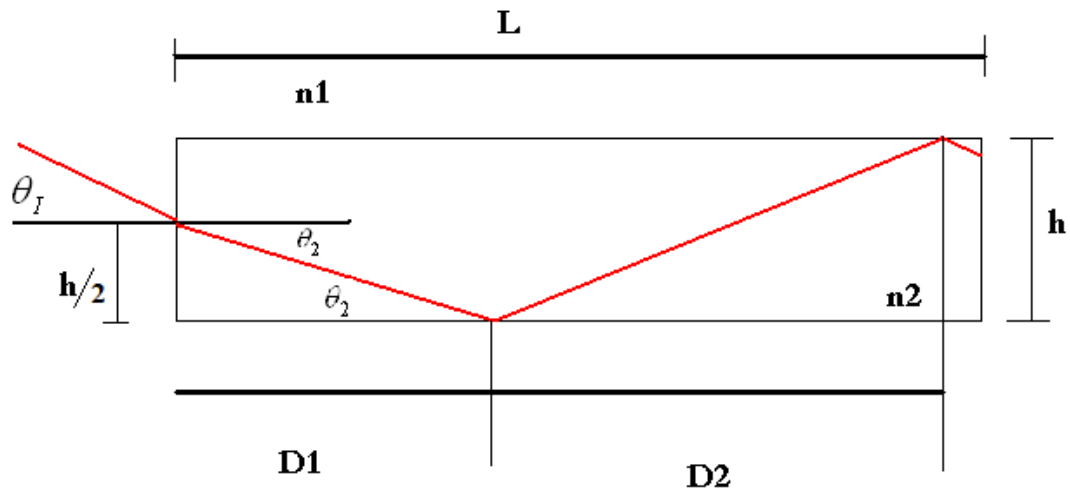


Figure 68 Angular definitions in rectangular prism LP.

When the incident angle is 0° , the only reflections come from the input and exit facets. When the incident angle is sufficiently larger, it is possible for there to be a third reflection resulting from a singular internal reflection from a sidewall. When the incident angle is sufficiently larger than that, multiple internal reflections occur. Therefore, in a single plane, there will be three cases for incident light: no internal reflections, a singular internal reflection, or multiple internal reflections. To facilitate appropriate definitions, a basic cross section is presented and labeled in **Figure 68**. Here,

$$D_1 = \frac{h/2}{\tan(\theta_2)} \quad (A1.1)$$

$$D_2 = \frac{h/2}{\tan(\theta_2)} = 2D_1 = \frac{h}{\tan(\theta_2)}$$

The refracted angle is given by,

$$\theta_2 = \sin^{-1} \left[\frac{\sin(\theta_1)n_1}{n_2} \right]. \quad (A1.2)$$

Substituting (A1.2) into (A1.1),

$$D_1 = \frac{h/2}{\tan \left(\sin^{-1} \left[\frac{\sin(\theta_1)n_1}{n_2} \right] \right)} = \frac{\pm h/2\sqrt{\theta_1^2 - \sin^2(\theta_1)n_1^2}}{\sin(\theta_1)n_1}, \pm \theta \quad (A1.3)$$

$$D_2 = \frac{h}{\tan \left(\sin^{-1} \left[\frac{\sin(\theta_1)n_1}{n_2} \right] \right)} = \frac{\pm h\sqrt{\theta_1^2 - \sin^2(\theta_1)n_1^2}}{\sin(\theta_1)n_1}, \pm \theta$$

Assuming the internal reflection angles are greater than the critical angles, the total number of reflections can be found by

$$N_{Total} = \begin{cases} 2 & , D_1 > L \\ 3 & , 0 < L - D_1 < D_2 \\ 3 + \left\lfloor \frac{L - D_1}{D_2} \right\rfloor & , L - D_1 > D_2 \end{cases} \quad (A1.4)$$

$$N_{Total} = \begin{cases} 2 & , D_1 > L \\ 3 & , D_1 < L < 3D_1 \\ 3 + \left\lfloor \frac{L - D_1}{2D_1} \right\rfloor & , L > 3D_1 \end{cases}$$

where two of the reflections are the reflections associated with the endfaces of the LP.

This can be alternatively represented by

$$N = 1 + \left\lfloor \frac{1}{2} \left(\left(\frac{h}{2} \right)^{-1} L \tan \left(\sin^{-1} \left[\frac{\sin(\theta_1) n_1}{n_2} \right] \right) - 1 \right) \right\rfloor \quad (\text{A1.4c})$$

Where n_1 is air, n_2 is the LP material, h is the input height, L is the length, and θ_1 is the incident angle.

When considering power transmission when loss at each reflection point is nonzero, it is important to note that **the total reflected power is NOT the sum of the losses from individual reflections.** Power is lost along the way so even if the same percentage of power is reflected from one bounce to the next, the total power lost at each bounce will be different. This means one must consider products instead of sums for determining accumulated loss. When considering loss at each reflection, the total transmitted power can be expressed simply as

$$P_{\text{Transmitted}} = P_{\text{Initial}} \prod_{n=1}^N (1 - \mathfrak{R}_n) \quad (\text{A1.5})$$

where N is determined through the preceding equations and \mathfrak{R} represents the total loss at a given reflection point from all loss contributors at that point. The contribution to loss by reflection can be found through the standard Fresnel reflection relationships.

$$\begin{aligned}
R_S &= \left| \frac{n_1 \cos(\theta_i) - n_2 \sqrt{1 - \left(\frac{n_1}{n_2} \sin(\theta_i)\right)^2}}{n_1 \cos(\theta_i) + n_2 \sqrt{1 - \left(\frac{n_1}{n_2} \sin(\theta_i)\right)^2}} \right|^2 \\
R_P &= \left| \frac{n_1 \sqrt{1 - \left(\frac{n_1}{n_2} \sin(\theta_i)\right)^2} - n_2 \cos(\theta_i)}{n_1 \sqrt{1 - \left(\frac{n_1}{n_2} \sin(\theta_i)\right)^2} + n_2 \cos(\theta_i)} \right|^2
\end{aligned} \tag{A1.6}$$

Where, of course, the indices of refraction are wavelength dependent. For the case of incident angles larger than the critical angle, total internal reflection occurs for a perfectly smooth interface. However even in these cases, loss from frustrated total internal reflection can exist, given the geometry and structure of the sample. For an uneven distribution of energy over the polarization states, the treatment must be applied to all states. The case of light composed of only s or p polarized light would use the following equations, for example,

$$\begin{aligned}
P_{P_{\text{Transmittal}}} &= P_{P_{\text{Initial}}} \prod_{n=1}^N (1 - R_{P_N}) \\
P_{S_{\text{Transmittal}}} &= P_{S_{\text{Initial}}} \prod_{n=1}^N (1 - R_{S_N}) \\
P_{\text{TotalTransmittal}} &= P_{P_{\text{Transmittal}}} + P_{S_{\text{Transmittal}}}
\end{aligned} \tag{A1.7}$$

If it is assumed that the percent loss is the same for all internal reflections, then one can construct the following equation

$$P_{\text{Transmitted}} = P_{\text{Initial}} (1 - R_{\text{Fresnel}_{\text{Input}}}) (x)^N (1 - R_{\text{Fresnel}_{\text{Output}}}) \tag{A1.8}$$

with N being the number of non-endface reflections. Rearranging this for x,

$$x = \left(\frac{P_{Transmitted}}{P_{Initial} (1 - R_{Fresnel})^2} \right)^{1/N} \quad (A1.9)$$

which is the coefficient of reflection of light reflected from a single internal reflection assuming all internal reflections impart the same loss. In this simplistic development, the angular distribution of light, or its change upon reflection (as the result of a non-ideal surface, for example), is not considered.

A1.2 Rectangular LP with 45° Input Face

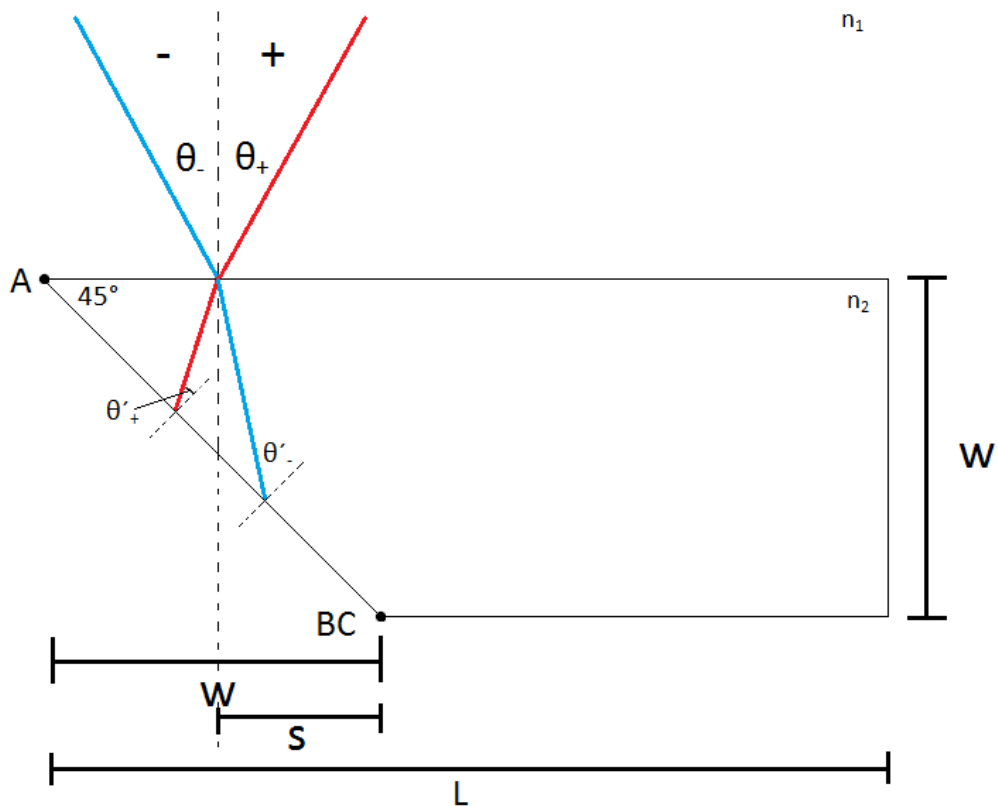


Figure 69 Angular definitions in rectangular LP with an angled face (45°) for light incident on the central location.

Using the variables defined in **Figure 69** and Snell's Law, the following relationships can be made,

$$\begin{aligned}\theta'_+ &= 45 - \sin^{-1}\left[\frac{n_1 \sin(\theta_+)}{n_2}\right] \\ \theta'_- &= 45 + \sin^{-1}\left[\frac{n_1 \sin(\theta_-)}{n_2}\right]\end{aligned}\tag{A1.10}$$

Combining these,

$$\theta'_\pm = 45 \mp \sin^{-1}\left[\frac{n_1 \sin(\theta_\pm)}{n_2}\right]\tag{A1.11}$$

Consider now the positive angle situation. At direct incidence, θ'_+ is already at 45° . Increasing θ_+ will decrease θ'_+ and will very quickly approach the critical angle of the input face's fused silica/air interface (for 514 nm light this happens around a 2.67° original incident angle). Violation of total internal reflection is not an issue for the negative angle situation. However, (A1.10b) is only valid so long as the refracted light reflects off of the input face. Let us now determine the incident angle for which the refracted light reflects off of the bottom corner of the LP. For an arbitrary incident location a lateral distance s from point BC , light will refract and encounter point BC internally when

$$\theta_- = \sin^{-1}\left\{\frac{n_2}{n_1} \sin\left[90 - \tan^{-1}\left(\frac{w}{s}\right)\right]\right\}\tag{A1.12}$$

For a 45° input face and light incident on a central location (upward projection of midpoint onto the input wall) this becomes

$$\theta_- = \sin^{-1} \left\{ \frac{n_2}{n_1} \sin \left[90 - \tan^{-1}(2) \right] \right\} \quad (\text{A1.13})$$

In the case of 514 nm light incident on fused silica, this corresponds to a negative angle of magnitude 40.8° . Negative angles having a magnitude larger than this will result in refracted light not being incident on the input face.

Turning attention to **Figure 70**, the distance to the first internal reflection is now considered, as it is the starting point in determining the number of internal reflections.

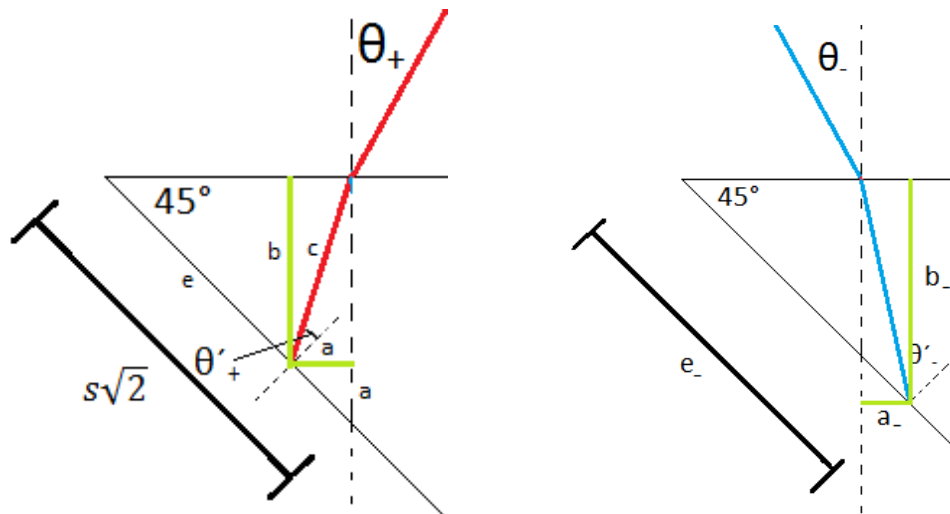


Figure 70 Quantities used to determine the number of internal reflections in a 45° LP.

It can be shown multiple ways that, for the case of a LP with a 45° input facet,

$$b_{\pm} = s \mp a \quad (\text{A1.14})$$

Using trigonometry then, one obtains

$$b_{\pm} = \frac{s}{1 \pm \tan(\theta_{\pm \text{Re } fractured})}, \quad (\text{A1.15})$$

which is rewritten as

$$b_{\pm} = \frac{s}{1 \pm \tan\left(\sin^{-1}\left(\frac{n_1 \sin(\theta_{\pm})}{n_2}\right)\right)}. \quad (\text{A1.16})$$

The lateral distance from the point of reflection on the endface to the first reflection with the sidewalls will occur at

$$\text{Lateral Distance} = b_{\pm} \tan(90 \mp (45 - \theta'_{\pm})) \quad (\text{A1.17})$$

Of course, this is already a distance b from the beginning of the LP. Therefore, the lateral distance *from the beginning of the LP* to the first reflection (DTFB) with the sidewalls will be, after rewriting,

$$\text{DTFB} = \frac{s + s \tan(90 \mp (45 - \theta'_{\pm}))}{1 \pm \tan\left(\sin^{-1}\left(\frac{n_1 \sin(\theta_{\pm})}{n_2}\right)\right)}, \quad (\text{A1.18})$$

or,

$$\text{DTFB} = \frac{s + s \tan\left(90 + \sin^{-1}\left[\frac{n_1 \sin(\theta_{\pm})}{n_2}\right]\right)}{1 \pm \tan\left(\sin^{-1}\left(\frac{n_1 \sin(\theta_{\pm})}{n_2}\right)\right)}. \quad (\text{A1.19})$$

2D Taper

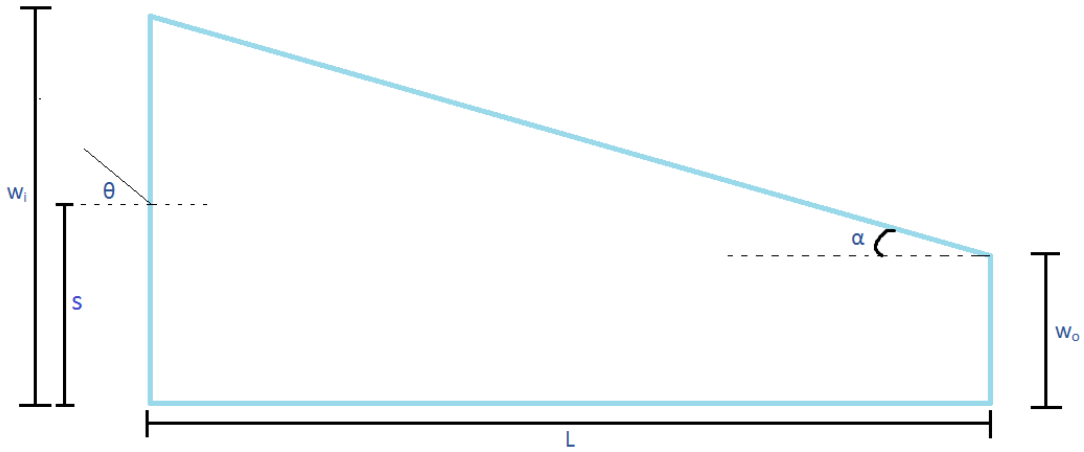


Figure 71 2D Tapered LP

Figure 71 shows the two dimensional geometry of a LP tapered in one direction where w_i is the width of the input face, w_o is the width of the output face, α is the taper angle, S is the input location of the interrogating beam, and L is the length of the LP. α is given by the arctangent of the quotient of the width difference over the length of the sample as

$$\alpha = \tan^{-1}\left(\frac{w_i - w_o}{L}\right). \quad (\text{A1.20})$$

From the input side, the width of the sample at an arbitrary location ℓ along L is given by

$$w(\ell) = w_o + (L - \ell)\tan(\alpha) \quad (\text{A1.21})$$

For a given input location, there are five general cases that can occur depending on the angle of incidence. These five cases are illustrated in order of decreasing $+\theta$ in **Figure 72 for when $S > w_o$** . The first three cases will be addressed presently.

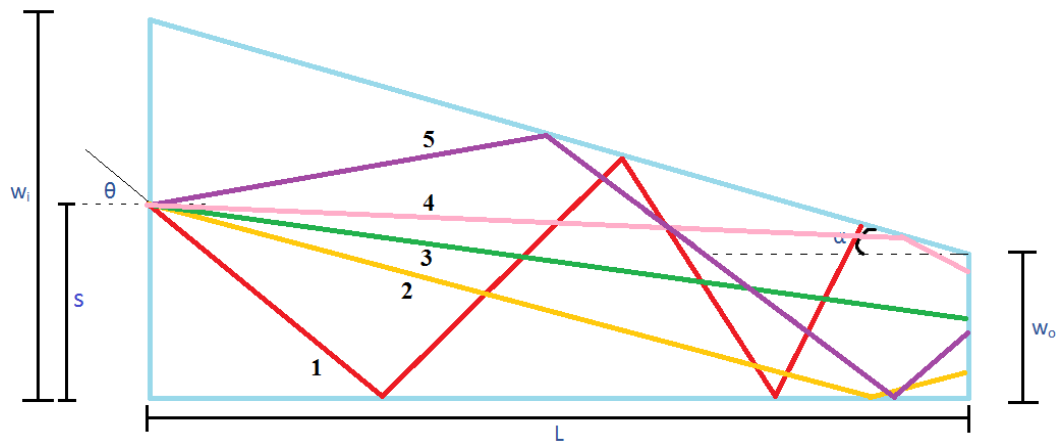


Figure 72 Propagation cases in 2D tapered LP.

Case 1

For rays incident first on the bottom of the LP after entrance, and then incident on the top surface, internal reflection angles will be given by

$$\theta_{R_n} = 90 - \theta_{Re\ fractured} - \alpha(n - 1) \quad , \quad n \geq 1 \quad (A1.22)$$

With the condition to travel in the forward direction being

$$\theta_{R_n} > \alpha \quad (A1.23)$$

This indicates that, for an incidence angle of 16° and a taper angle of 5.14° (assuming a 10 mm sample with an output end 1/10th the width of the input), it takes about eight internal reflections before the critical angle is reached (assuming fused silica in air). It is important to note that these equations might lead to non-physical situations and the results of a given computation should be verified to correspond to a physical situation.

To understand when case one is anticipated, let us look at **Figure 73**

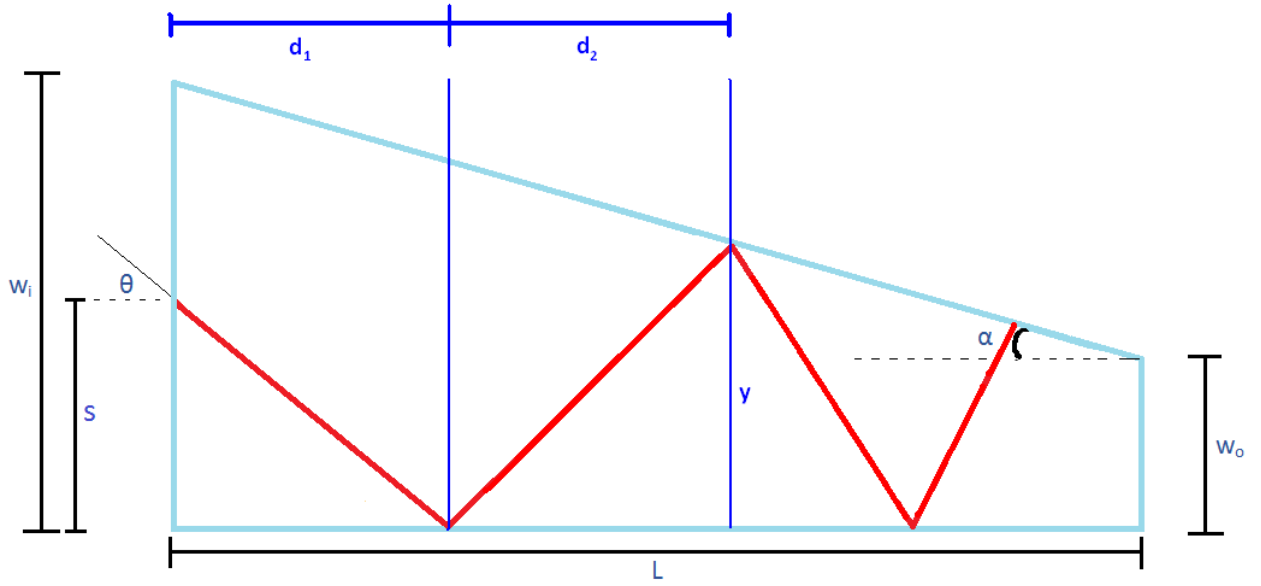


Figure 73 Case 1.

This case is anticipated when $d_1 + d_2 < L$. Noting that the complement of the first internal incidence angle is the refracted angle, the following relationships can be shown

$$d_1 = \frac{s}{\tan(\theta_R)} = s \tan(90 - \theta_R) \quad (\text{A1.24})$$

$$d_2 = \frac{y}{\tan(\theta_R)} = \frac{w_o + (L - d_1) \tan(\alpha)}{\tan(\theta_R) + \tan(\alpha)} \quad (\text{A1.25})$$

Therefore, case one applies when

$$\frac{s}{\tan(\theta_R)} + \frac{w_o + \left(L - \frac{s}{\tan(\theta_R)} \right) \tan(\alpha)}{\tan(\theta_R) + \tan(\alpha)} < L \quad (\text{A1.26})$$

The next step is to determine the number of internal reflections for a given angle of incidence and input location. The general idea is to determine how many complete

internal reflections can take place (integer value) in the given sample length. To accomplish this, we turn our attention to **Figure 74**.

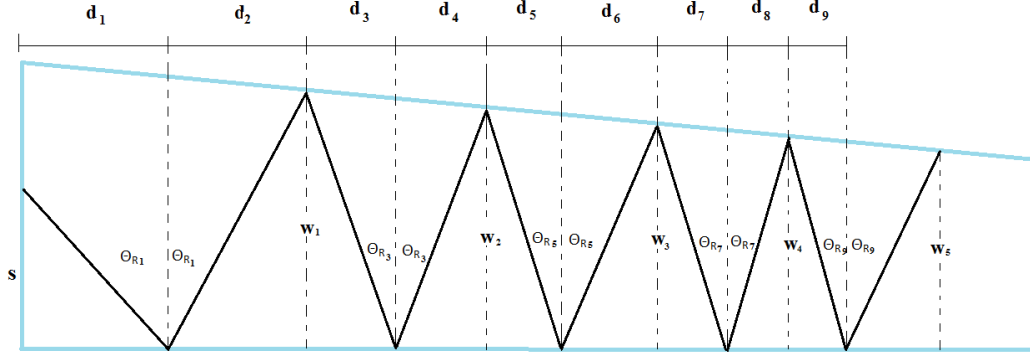


Figure 74 Internal reflections in 2D taper. The illustrated propagation is non-physical in the sense that the reflection angles have been drawn to allow for room for labels.

One can show the following relationships,

$$w_{i=\frac{n-1}{2}, n \text{ odd}} = w_o + \left(L - \sum_{m=1}^{\substack{n, n \text{ even} \\ n-1, n \text{ odd}}} d_m \right) \tan(\alpha) \quad (\text{A.127})$$

$$d_{n \text{ odd} > 1} = \frac{w_{\frac{n-1}{2}}}{\tan(90 - \theta_{R_n})} = \frac{1}{\tan(90 - \theta_{R_n})} \cdot \left[w_o + \tan(\alpha) \left(L - \sum_{m=1}^{n-1} d_m \right) \right] \quad (\text{A1.28})$$

$$d_{n \text{ even}} = \frac{w_{n \text{ even}}}{\tan(90 - \theta_{R_{n-1}}) \tan(90 - \theta_{R_{n-1}})} \cdot \left[w_o + \tan(\alpha) \left(L - \sum_{m=1}^n d_m \right) \right]$$

However, one might notice that the n even case is recursively defined so we rewrite this

as

$$d_{n\text{ even}} = \frac{w_o + \left(L - \sum_{m=1}^{n-1} d_m \right) \tan(\alpha)}{\tan(90 - \theta_{R_{n-1}}) + \tan(\alpha)} \quad (\text{A1.29})$$

With the total lateral distance (projection onto z-axis) for a given internal reflection number being

$$D = \frac{s}{\tan(90 - \theta_{R_1})} + \sum_{m=2}^n d_m, \quad (\text{A1.30})$$

where the first term can be thought of as d_1 . Therefore, the total number of internal reflections N will be

$$N = 1 + n \quad (\text{A1.31})$$

Where n is the largest integer that satisfies the condition $D < L$.

Case 2

This case is an extension of case one where the entrance angle and location is such that the propagation of the beam inside the LP results in a singular reflection from the bottom surface before striking the output surface. This happens when the following condition is satisfied

$$(L - d_1) \tan(\theta_R) < w_o. \quad (\text{A1.32})$$

Case 3

Here, rays do not directly interact with either the top or bottom surfaces and reflect and transmit from the input and output faces. The angle incident on the output face will be

equal to the refracted angle achieved upon entry into the LP. The conditions for this to happen are split between two subcases. When $S < w_o$, one can think of the triangle created with the width at the output plane being denoted by o . For positive theta angles, this output width needs to be less than S . For negative angles, this needs to be less than $w_o - S$. When $S > w_o$, only positive theta angles are allowed with the constraint that the ray must be incident on the output face and hit neither the top nor the bottom of the LP on its way there. These situations are summarized here

For $S < w_o$,

$$\begin{aligned} o < s &\rightarrow L \cdot \tan(\theta_R) < s, & \theta > 0 \\ o < w_o - s &\rightarrow L \cdot \tan(\theta_R) < w_o - s, & \theta < 0 \end{aligned} \quad (\text{A1.33})$$

For $s > w_o$,

$$s > o > s - w_o \rightarrow s > L \cdot \tan(\theta_R) > s - w_o, \quad \theta > 0 \quad (\text{A1.34})$$

APPENDIX II

LIBERATION PROCEDURE

This appendix describes a general procedure for liberating a small fused silica LP from a borosilicate glass substrate when bonded with an ultraviolet-cured optical adhesive.

Liberation Procedure

Make sure to wear ALL appropriate personal protective equipment (PPE) when dealing with glass, and toxic and corrosive chemical fumes (refer to material safety data sheets prior to their use). It is good practice to wear a pair of nitrile gloves under the silver lined gloves. Given the extreme delicacy of the samples, it is best to consider and conduct yourself as a surgeon performing surgery on the sample and that the sample's life depends on your good performance (because it does!). It has been observed that the more viscous the adhesive, the more time it takes to dissolve. Also, the adhesive does dissolve when subjected to many less corrosive/aggressive solvents, such as IPA. Since methylene chloride/dichloromethane is a strong organic solvent, it will dissolve many plastics and organic materials (such as wooden applicators). Dissolved adhesive will create a film on the surface of the solvent bath and will stick to anything it touches. Note that the following procedure is to liberate "in a hurry" (with "hurry" being an hour or so). The adhesive manufacturer's website suggests dissolving overnight. The general procedure is as follows and will often take an hour to complete:

1. Place mounted sample in appropriate container (glass, NOT plastic). A clean Pyrex glass petri dish is a good choice. The solvent will easily dissolve a plastic petri dish.
2. Fill container with enough solvent to fully submerge the sample. As the solvent used is volatile, it will evaporate quickly. Cover the container with a beta wipe if it does not have a lid.
3. Leave the sample in the bath for at least 15 minutes. The amount of time required depends on the adhesive being dissolved. The more viscous the adhesive, the longer one should leave the sample in the bath. When dissolving NOA 1328, for example, you will be doing yourself a favor if you leave the sample in the bath for at least 40 minutes.
4. After the initial waiting period, very carefully, gently, and slowly run one side of a set of appropriate plastic tweezers (rinse the tweezers under water immediately after removing them from the bath to prevent them from being dissolved) along the bonded edges of the LP. In doing this, you are both helping the adhesive removal process, and testing to see how dissolved the adhesive is. Only very light pressure should be applied, since the sample can easily break. **BE CAREFUL** not to ram the ends of the LP into the walls of the container, which would damage them. **Avoid contact between the endfaces and the walls of the container in general.** This may need to be repeated multiple times after multiple waiting periods.

5. Once the LP is freed from its base, allow the LP to sit in the solvent for a few more minutes but note that it might partially re-adhere to the container so one must be careful picking it up after waiting.
6. Prepare another container with water.
7. Carefully, remove the light pipe from the solvent bath with tweezers and submerge it in the water container only long enough to “rinse” the sample. The sample will have a sticky layer of adhesive on it, most likely. When grabbing the sample with tweezers, note that the tweezers might stick to the sample or to itself.
8. Using lens tissue and IPA (methanol might be a better candidate), **gently** clean the sample to remove the adhesive that remains. The adhesive will exist on the lens tissue and will stick to whatever it touches so use one piece of tissue once, and then switch to another tissue for a final cleaning. A good method of cleaning the sample is to gently pinch the sample with folded lens tissue and to pull the sample through. **Do not induce a torque on the sample otherwise it will break.** Pressing too hard can scratch the sidewalls, even with lens tissue.
9. Set the LP aside and keep in mind that it can easily be launched by lens tissue that is relaxing from a folded state or be blown away from breathing in its direction.
10. Remove the base/substrate from the solvent bath and clean with a beta wipe in a similar fashion (save the optical lens tissue for the samples).
11. Dispose of the chemicals properly. This completes the liberation process.

APPENDIX III

MICROSOFT EXCEL FORMULA FOR USE WITH THE Θ STAGE

In order to set the desired angle of the θ mount, a Microsoft Excel spreadsheet was used.

The example functionality is shown below in **Figure 75**.

	A	B	C	D	E
1					
2		Knob Rotations Per Degree	2.08889		(188 turns / 90 degrees)
3		Zero Incident Angle Knob Position	1.64		
4					
5		Desired Input Angle	Value	Tens Digit	Position Setting
6		-55	-113.25	-12	6.75
7		-50	-102.80	-11	7.20
8		-45	-92.36	-10	7.64
9		-40	-81.92	-9	8.08
10		-35	-71.47	-8	8.53
11		-30	-61.03	-7	8.97
12		-25	-50.58	-6	9.42
13		-20	-40.14	-5	9.86
14		-15	-29.69	-3	0.31
15		-10	-19.25	-2	0.75
16		-5	-8.80	-1	1.20
17		0	1.64	0	1.64
18		1	3.73	0	3.73
19		2	5.82	0	5.82
20		2.5	6.86	0	6.86
21		5	12.08	1	2.08
22		7.5	17.31	1	7.31
23		10	22.53	2	2.53
24		12.5	27.75	2	7.75
25		15	32.97	3	2.97
26		20	43.42	4	3.42
27		25	53.86	5	3.86
28		30	64.31	6	4.31
29		35	74.75	7	4.75
30		40	85.20	8	5.20
31		45	95.64	9	5.64

Figure 75 Example θ stage angle calculation spreadsheet.

A repurposed counting dial/knob was attached to the knob shaft of the rotation stage and is shown in **Figure 76**.



Figure 76 Counting dial/knob used with the theta rotation stage.

Looking at the dial/knob and comparing it to any of the numbers in column E of the spreadsheet in **Figure 75**, the ones digit refers to the outermost number of the dial/knob, the tenths digit corresponds to the innermost labeled number, and the hundredths digit corresponds to the gradation mark. In **Figure 76**, the dial/knob currently displays a value of “2.08” where the tens digit is kept track of via pencil and paper, or through other means. As ten rotations of the dial/knob reset the outer ring of the dial/knob back to its starting point, it is necessary to keep track of this “higher digit” and is referred to as the “Tens Digit” listed in column D of the spreadsheet shown in **Figure 75**. The formula used to calculate cell C6 is

$$=C\$3+C\$2*B6$$

This formula uses the “Zero Angle Incident Knob Position,” specified in cell C3, as what would be determined through optical alignment after sample mounting as the position at which light is incident on the sample at zero degrees. It takes this value, and adds the desired angle to its value after the desired angle is converted into the number of knob/dial turns. The formula used to calculate cell D6 is

$$=FLOOR(C6/10,1)$$

This formula simply rounds the calculated value down to its nearest integer, after dividing it by ten. The formula used to calculate cell E6 is

$$=(10*ABS(D6)+C6)*(1-(C6+ABS(C6))/(2*ABS(C6)))+(C6-FLOOR(C6/10,1)*10)*((C6+ABS(C6))/(2*ABS(C6)))$$

In order to understand why this formula is what it is, one needs to realize that, for example, while $0 + .2 = +.2$, and $0 - .2 = -.2$, a knob set at 0.00 would read 0.2 if .2 were added to it, while on the other hand it would read 9.98 if -.2 were added to it. For efficiency, a singular formula structure is desired to be used with any angle, regardless if the angle is positive or negative. To save the user from having to use two different formulas based on a positive or negative angle, the formula used employs a structure such as this one

$$y = 1 - \frac{x + |x|}{2|x|}$$

Here, it is clear to see that when $x > 0$, $y = 0$ and when $x < 0$, $y = 1$. Using structures like this allows the user to apply formulas that compute one thing for a positive input,

and compute something entirely different for a negative input and essentially turn on or off parts of a formula under different circumstances.

APPENDIX IV

NOTES REGARDING WORKING WITH NORLAND OPTICAL ADHESIVES

Adhesive product names are given and followed by an informal description of various observations made regarding their behavior.

13685 – First adhesive to be used in this project. Behaves similarly to water. A quick spot cure can be obtained with two minutes. The adhesive appears to have a type of “memory” when heated. A test of using a hot plate and heating (perhaps 120°C) a cured drop of the adhesive folded and bent over on itself multiple times revealed that the drop unfolded itself and attempted to form its original position obtained after curing. Low surface tension. It has been observed once that a drop migrated up a suspended, vertically orientated, sample from its endface (lowest point) up its sidewalls all the way to the top of the sample (5 or 10 mm above). This can happen if an edge or corner is touched with the adhesive applicator.

1328 – High viscosity adhesive used in most recent data runs. Usually used after an “overnight cure” (169 minutes of UV light, the maximum of the curing lamp timer, plus oxygen environment drying) to achieve a good enough cure though not enough to avoid a sample from sliding over a period of time. The sample’s high viscosity usually necessitates waiting 30 seconds for a drop to finally come out of its syringe container.

1327 – According to its data sheet online, it is more viscous than 1328. However, it appears to flow more easily than 1328 though this could be due to the larger size syringe

that the 1327 is kept in -30cc instead of 10cc as in the case of 1328. It was noticed that the blue endcap on the back of the syringe was not seated well so some oxygen may have influenced some of this adhesive. It is also the messiest adhesive to work with as it very easily develops drawn strands of adhesive than can seemingly stretch forever. This adhesive is remarkably quick drying and seems to have the property that working the sample (e.g. stretching, folding, pulling, twisting, etc.) induces localized cure spots. This is perhaps similar to work hardening metal, and the adhesive might undergo significant heating at worked areas that induce a drying or cure. It was also noticed that bring a soldering iron tip close to the adhesive made a slightly tacky adhesive surface (cure obtained after UV exposure for approximately four minutes) less tacky. This adhesive only takes a few minutes to obtain a functional cure for most current uses.

1315 – Evaporates fast. In less than ten seconds, a small drop applied to the endface of a sample will be completely evaporated. This adhesive also seems to exhibit the lowest surface tension of all other listed adhesives. Its propensity to evaporate makes the adhesive hard to contain on a given surface if another surface exists nearby in an upward relative location. Perhaps the lowest viscosity adhesive we have, as well.

142 – Flows similarly to 13685. Has the highest Shore D hardness of any of the listed adhesives. Perhaps for this reason, this adhesive exhibits the best performance when used as an “endface flat.”

85 – Refractive index is listed at 1.46, making it the closest adhesive to index matching for fused silica (1.4616 at 514 nm). Cures fast (within minutes) and is relatively easy to work with.